九州大学学術情報リポジトリ
Kyushu University Institutional Repository

Study on Modeling of Seismic Wave and Gas Permeability Characteristics through Porous Layers in Goaf

杨, 晓晨

https://hdl.handle.net/2324/1959124

出版情報：Kyushu University, 2018, 博士（工学）, 課程博士
バージョン：
権利関係：

Study on Modeling of Seismic Wave and Gas Permeability Characteristics through Porous Layers in Goaf

KYUSHU
UNIVERSITY

YANG XIAOCHEN

JULY 2018

Study on Modeling of Seismic Wave and Gas Permeability Characteristics through Porous Layers in Goaf

A DOCTORAL DISSERTATION

SUBMITTED TO THE GRADUATE SCHOOL OF ENGINEERING

KYUSHU UNIVERSITY

AS A PARTIAL FULFILLMENT OF THE REQUIREMENTS FOR THE DEGREE OF

DOCTOR OF ENGINEERING

BY

YANG XIAOCHEN

SUPERVISED BY

PROF. KYURO SASAKI

DEPARTMENT OF EARTH RESOURCES ENGINEERING

KYUSHU UNIVERSITY

FUKUOKA, JAPAN

JULY, 2018

CERTIFICATE

I certify that I have read this dissertation and that , in my opinion, it is fully adequate in scope and quality as a dissertation for the degree of Doctor of Engineering.

_____

Prof. Kyuro Sasaki (Principal Supervisor)

_____

Prof. Hemanta Hazarika (Examining Committee)

_____

Prof. Zhang (Examining Committee)

_____

Prof. Yuichi Sugai (Examining Committee)

Graduate School of Engineering,

Kyushu University

July, 2018

Truth is so large a target that nobody can wholly miss hitting it, but at the same time, nobody can hit all of it…

The investigation of the truth is in one way hard, in another easy. An indication of this is found in the fact that no one is able to attain the truth adequately, while, on the other hand, no one fails entirely, but everyone says something true about the nature of thing, and while individually they contribute little or nothing to the truth, by the union of all a considerable amount is amassed. Therefore, since the truth seems to be like the proverbial door, which no one can fail to hit, in this way it is easy, but the fact that we can have a whole truth and not the particular part we aim at shows the difficulty of it. Perhaps, as difficulties are of two kinds, the cause of the present difficulty is not in the facts but in us.

Aristotle

Abstract

The large amount of underground coal excavations have caused about 430 million-m^3 goaf widely distributed in China. Goaf is an area that partially or wholly filled with waste and the collapsed rock mass from roof. The monitoring of the goaf properties is important, because the goaf-induced hazards are various with a potential threaten role to the mining operation and natural environment. The seismic method is an effective tool to detect goaf properties. However, in most of the previous investigations using with seismic velocity and attenuation in the goaf areas, goafs were treated as a homogeneous medium and the optimal seismic frequency was not considered against actual rock mass sizes. The characteristics such as porosity, stiffness of discontinuities, size of voids and fragments in the goaf area have not been clearly related to the seismic data, and a model to estimate gas permeability in the goaf also has not been established based on the seismic properties. In the present study, laboratory measurements were done using porous samples compressing rock particles to construct the new model equations for seismic attenuation and gas permeability consisting porosity, ratio of seismic wave length to particle size, and mechanical properties to apply for a field measurement in underground coal mine area. Furthermore, the quantitative damage by earthquake on the ground surface have been simulated to clear the effect of the goaf on the seismic response.

The dissertation is composed of six chapters as follows:

Chapter 1: This chapter describes a potential inducing hazards by the existence of goaf in the underground strata and provides a background on the detection technologies of goaf field in coal mine areas. Furthermore, this chapter reviews in-situ investigations and theoretical approaches about the seismic and permeability characteristics of goaf presented by previous researches. The research objectives and thesis structures are also described in this chapter.

Chapter 2: This chapter elaborates the measurement apparatuses and methodologies of the seismic and gas permeability in the laboratory. The preparation processes of intact rocks and porous samples compressing rock particles were described. Firstly, elastic modulus, porosity-effective relationship, mineral composition as well as the microstructure of three types of intact rocks, limestone, sandstone and bituminous coal, were measured as basic seismic data to compare the porous rock samples. Three intact rocks were crushed and sieved into particles with three group sizes of 0.12-0.25 mm, 0.25-0.5 mm and 0.5-1.0 mm. Those particles were used to form 135 porous specimens that were pressed in a cylindrical PVC pipe surrounded by a stainless socket using a hydraulic compression press. The porosities of the specimens were controlled to be 0.21 to 0.33 with stepwise compressive process and stress, because seismic property and gas permeability are very sensitive to the porosity. The seismic velocity and attenuation through the specimens were measured by wave frequency from 24 to 500 kHz. The permeability (k) was also measured with same porous specimens used for seismic measurements. The seismic attenuation and elastic velocity changes in rock/coal with different porosities, the effect of particle size (D) and seismic wavelength (λ) were deeply investigated.

Chapter 3: This chapter describes a new seismic attenuation model (the B-R model) based on the multi-fractured rock attenuation model. The B-R model accounts for (i) greater attenuation through fragmented rock due to increased contact points between the particles, and (ii) decreased attenuation caused by network propagating through the porous media. The B-R model was applied to the laboratory measurement results of ultrasonic wave attenuation using compressed porous rock and coal samples, and good agreements were found for various porosities, particle sizes and wavelength. The relationship between porosity and elastic velocity change was closer to that of the B-R model compared with the empirical relation. The B-R model showed better agreement with measurement results when λ/D varied between 65 and 80, which covers most of the λ/D range expected at a coal mine goaf.

Chapter 4: This chapter describes the results of permeability of the porous samples. The results showed that the measured permeability conformed to the corrected Kozney-Carman equation with percolation threshold porosity of 0.06, tortuosity 5–10 and power 4 on porosity. It was cleared that the permeability of porous samples can be expressed with a new model equation combining average square value of particle sizes and two functions defined for seismic velocity change and attenuation. The estimated permeability by the model equation showed a good agreement with the measured permeability data. The permeability of the actual goaf in coal mine was estimated to be $k = 10^7$-10^9 md based on compressive stress, rock mass size and properties in the goaf.

Chapter 5: This chapter describes seismic damping coefficient input for the simulator to investigate earthquake wave propagation through the gaof area. The variation of the elastic modulus of goaf material with time was also explained. Various simulations models were established considering the depth, porosity, compaction time as well as the varied damping coefficient. The numerical simulation results showed that the peak ground acceleration (PGA) above the goaf area is reduced because of the presence of goaf. The PGA above goaf is gradually increased with the increasing depth and compaction time of goaf. However, peak ground displacement (PGD) above goaf is increased as the reduction of depth and compaction time of goaf. Especially, the PGD above a shallow goaf 100m from the surface is amplified 2 to 7 times compared with that of the free-field condition. Additionally, the resonant period of the response acceleration spectrum above goaf is around 0.2s longer than that of the places above undisturbed coal-seams.

Chapter 6: This chapter presents the conclusions of this study including the seismic and permeability properties of goaf areas as well as the application of the established models for the estimation of permeability and earthquake damage in the underground coal mine field scale.

Table of Contents

List of Tables

List of Figures

Acknowledgements

Firstly, I would like to express my sincerely gratitude and highly acknowledge to Prof. Kyuro Sasaki for the opportunity provided to me to pursue the Ph.D degree at Kyushu University. He has given me not only the professional knowledge and rigorous attitude on academic research, but also the perspective and thinking depth on the study and life. My research can not be conducted without his patient guidance and instructions. I also would like to express my appreciation to Prof. Zhang for his support on my research and my life. I am also very thankful to Prof. Yuichi for his assistance on my research and instruction on my experiment.

I would like to pass my deep gratitude to Prof. Hemanta Hazarika for his reviews and comments to improve my thesis considerably. I thank Prof. Hideki Shimada for his providing and support on my laboratory equipment. I also would like to express my respect and gratitude to Dr. Ronald and Dr. Afika for their professional advises and comments. Furthermore, I thank Dr. Wang from Liaoning Technical University for his useful discussion on my research. Equally, I thank Mr. Jia from the CCTEG Shenyang Research Institute for his valuable in-situ information.

I gratefully acknowledge financial support received from the Japanese Government (MEXT) to pursue Ph.D degree at Kyushu University. I also would like to thank the funding support for my conferences and researches abroad by Kyushu University. I thank the Daliuta coal mine in Inner Mongolia for providing the coal samples.

I would like to thank Mrs. Zhao for her care and help on my life. Meanwhile, I thank all former and present members of Resources Production and Safety Engineering Laboratory for their assistance and lively environment.

Finally, my deep acknowledge to my mother and my girl friend for their support and understanding.

Chapter 1: Introduction

1.1 Energy production from coal

The fossil resources including oil, natural gas and coal account for about 86% of the global energy supplements. As is reported by BP Statistical Review of World Energy, the percentage of oil, gas, coal have a share of 33, 24 and 28%, respectively in the global energy mix in 2017. Even if a number of pollution and climate change issues have been caused by fossil resource burning, but the fossil resources are still holding the domination of the energy supply.

Meanwhile, it can be seen in Figure 1-1, the coal production in the last 25 years are steadily increasing in the global energy proportion. As is well known, coal is a finite and non-renewable resource in the nature. Meanwhile, a number of artificial hazards and pollution are induced by mining activity. Therefore, the safe and sustainable as well as environment-friendly mining operation needs to be vigorously developed.

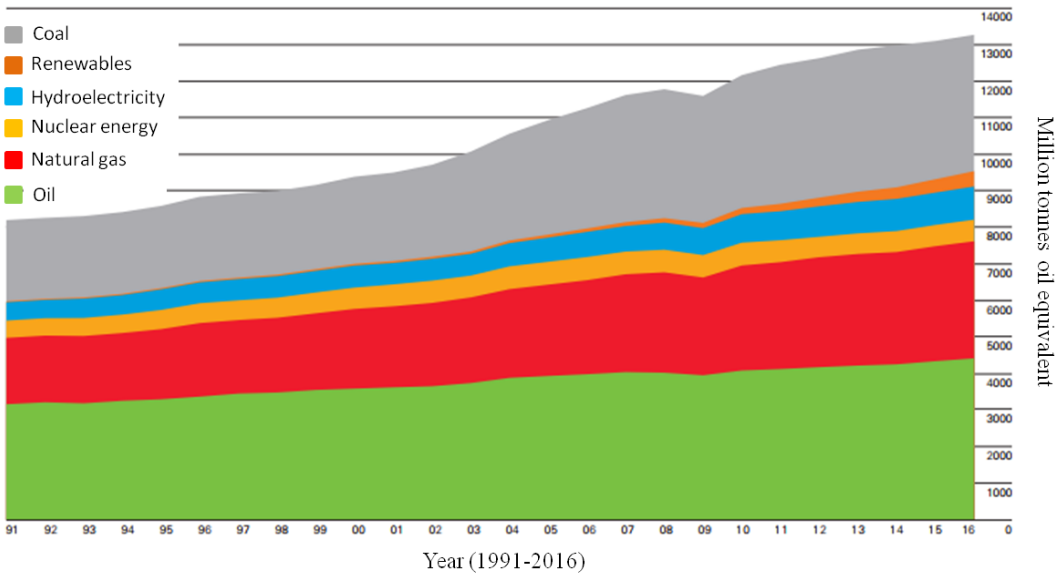

Figure 1-1. Proportion of resources in the global energy production (BP Statistical Review of World Energy, 2017).

In my view, three major factors are supposed to be considered in the coal exploitation.

- Trying our best to guarantee the safety in the coal mining operation including underground and surface coal mines.
- Taking the efforts to reduce the pollution caused by mining activities and coal usages.
- Strive to develop the clean, environment-friendly and lower-cost method in monitoring and management in coal fields.

1.2 High-intensity and large-scale coal production in China

According to the latest report, the coal production of China is the largest in the world, which takes account 51% of the global coal production (Figure 1-2) (BP Statistical Review of World Energy June, 2017).

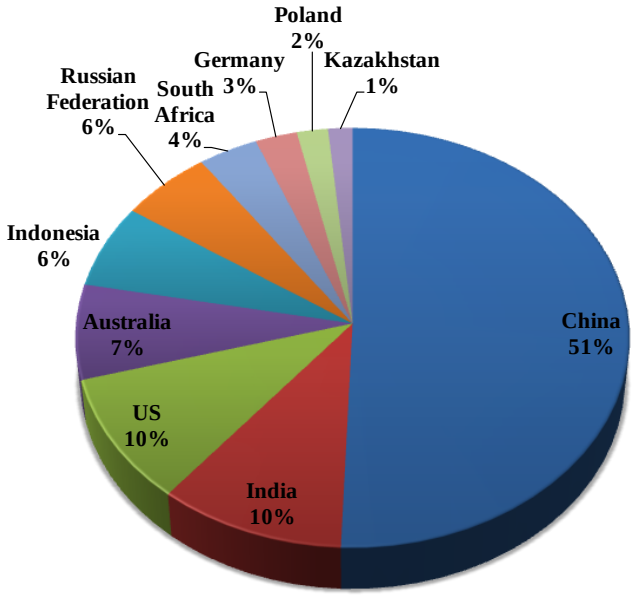

Figure 1-2. Coal production by region (BP Statistical Review of World Energy, 2017).

Coal occupies the absolute majority of primary energy supply in China. Around 72% of the Chinese energy production are from coal. About 75% of industrial fuels, 85% of chemical raw materials, and 90% of civil fuels depend on the energy produced by

coal. Therefore, for a long period in future, coal resource is still the largest source for the Chinese energy demand. With the rapid demand for development, Chinese annual coal production have risen up to about 3.5–4.3 billion tons, in which around 2.8 billion tons come from the underground coal mine. Meanwhile, as the year-to-year increasing exploitation of coal resource, a series of issues have inevitably occurred involving environment, safety and geological damage.

1.3 Goaf-induced hazards in underground coal mine

1.3.1 What is goaf ?

The mining method can be approximately divided into two ways: underground mining and surface mining. Around 60% of the global coal mines are exploited by underground coal mining (Figure1-3). In the process of underground coal exploitation, as the working face moves forward, coal is partially or wholly removed from the coal seam, therefore, the roof above the coal seam will be broken into fragments and collapse into the space behind the working face. This abandoned area behind the working face is called as goaf.

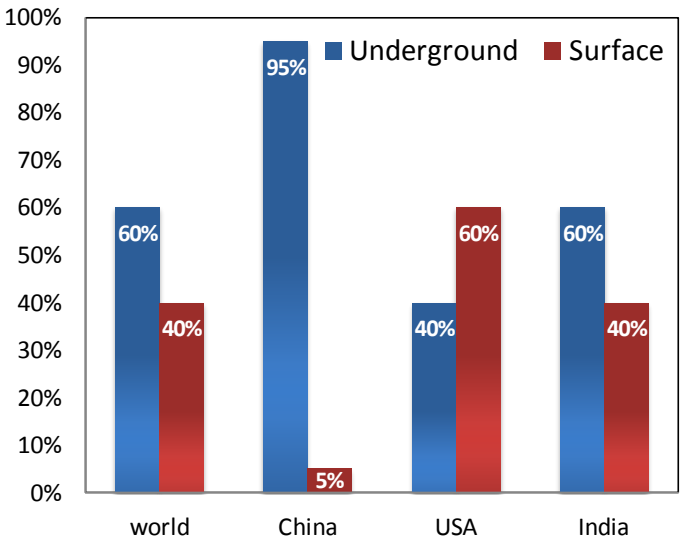

Figure 1-3. The number of the underground and surface coal mines in the three world largest coal production countries (Energy choices, 2014).

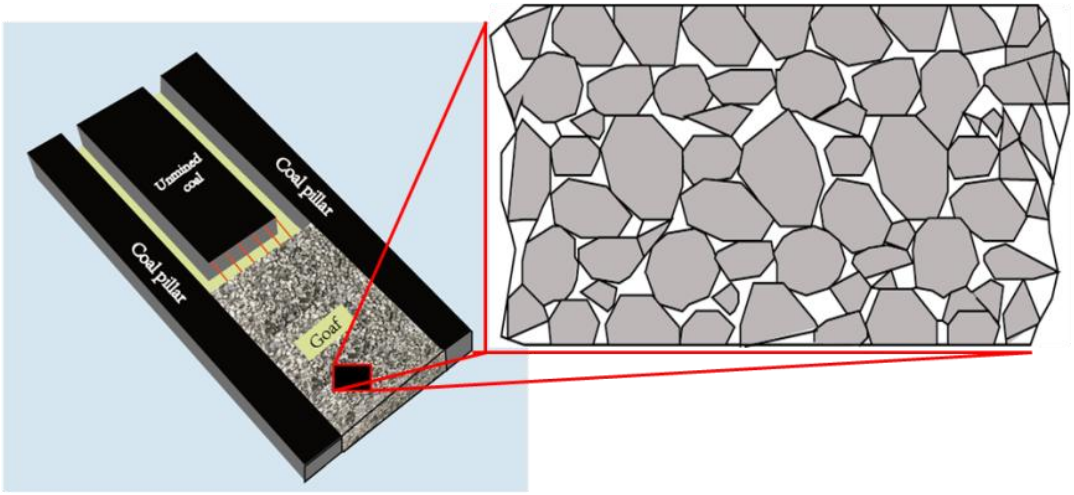

Figure 1-4. Schematic figure of underground goaf.

As is mentioned, a goaf consists of fragmented rock that collapsed from the roof rock above the coal seam (Figure1-4). Because significant rock-mass failures and subsequent stress redistribution are induced after coal extraction, several issues of a goaf must be considered, including collapsed areas and goaf reconsolidation. Based on the different mining methods and management, goafs are divided into different types. The classification of general goafs is listed in Table 1-1.

Table 1-1. Coal mine goaf classification (Lunarzewski, 2010)

<table>
<tr><th>Classification</th><th>Mine entries and surface boreholes</th><th>Ventilation</th><th>Coal production</th><th>Water pumping</th><th>Responsibility</th></tr>
<tr><td>Temporary closed</td><td>Opened, not permanently or partially sealed</td><td>Operating on reduced capacity</td><td>Ceased Possible future production</td><td>Optional</td><td>Mine operator (maintenance)</td></tr>
<tr><td>Closed</td><td>Partially or fully sealed</td><td rowspan="4">Terminated</td><td rowspan="4">Ceased No future production</td><td rowspan="3">Terminated Goaves gradually flooding</td><td>Mine operator</td></tr>
<tr><td>Decommissioned</td><td rowspan="3">Permanently sealed</td><td rowspan="2">Transferred from mine operator to the relevant Authority</td></tr>
<tr><td>Abandoned</td></tr>
<tr><td>Sealed longwall or district</td><td>Optional</td><td>Mine operator</td></tr>
</table>

1.3.2 The issues induced by underground goaf

The coal produced by underground mining takes account a large proportion of the total coal production. It was reported that by the end of 2017 (China National Energy Administration, 2017), in China, around 4980 coal mines are in the running with the production capability of 4.36 billion tons per year. Around 95% of these mines are underground coal mine that distributed in the major six coal formations (Figure 1-5).

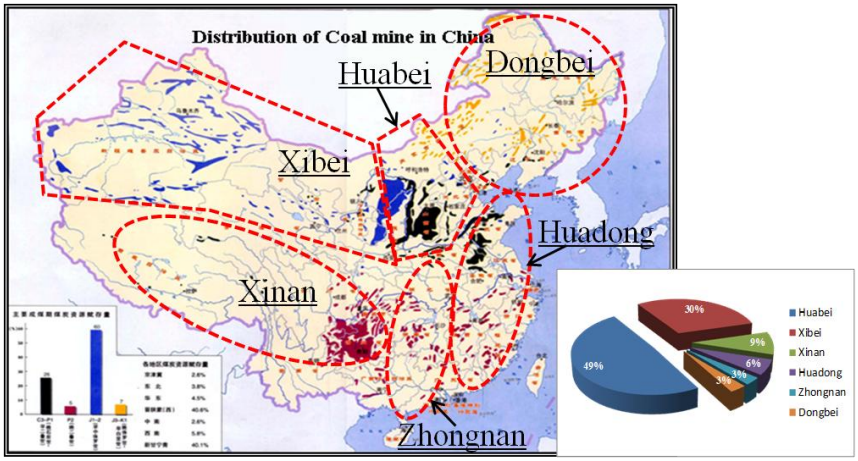

Figure 1-5. Distribution of coal field in China (China National Energy Administration, 2015).

Because of the large-scale of underground exploitation, the abandoned goaf areas distributed in various parts of China are approximately 432 million m^3 (China National Energy Administration, 2015). For an example, one of largest coal production province, Shanxi, there are 3000 km^2 goaf areas have been found in the running and abandoned underground coal mines (China National Energy Administration, 2017).

In addition, in China, about 95% of the coal production is conducted by underground mining with long-wall working faces and managed by roof collapse method. This kind of mining method has induced unrecoverable structural damage to the overlying strata and caused severe surface subsidence. Such a large area of underground goaf plays a big potential threaten to the people and environment. For instance, the mining activity causes permanent and unrecoverable damages to the strata and further surface

destruction, including land resource subsidence and occupation, water resource loss and pollution, air pollution, as well as ecological damage and degradation. Additionally, the goaf areas containing highly void ratio could induce a leakage of ventilation airflow from the working face into the goaf areas (Karacan et al., 2011). The leakage air could induce coal spontaneous combustion(Wang et al., 2017) and then produce air pollution and greenhouse gas emission. Meanwhile, the methane from the adjacent coal seam is possible to flow into a goaf area through the fractured zone and then into the working face. Overall, the underground coal mining process has caused various serious and permanent destruction to the environment and human properties.

Facing such a big area in underground goaf, the most important is to accurately estimate the valuable properties of the active and abandoned goafs, including the mechanical and hydraulic properties. Only in this way, the goaf areas can be further utilized controlled and managed

1.4. The characters of the underground goaf areas

1.4.1 Porosity of goaf

Esterhuizen and Karacan (2007) proposed that the swelling ratio of goaf can be estimated based on the ratio of fall height to fragments width in terms of the rotation of the fragments. The porosity range 22-42% showed a good agreement with a realistic goaf gas venthole production that was employed as the parameter in the reservoir modeling. Karacan (2010) developed an approach that combines fractal scaling in porous medium with principles of fluid flow to estimate the porosity of goaf materials. Zhou (2006) obtained the porosity (void ratio) in the goaf by taking the pictures of some piles of fragments inside the goaf.

Meanwhile, Szlązak (2001) presented that the formation pressure on the goaf area is increased with the distance from the working face because of the compaction, but the increasing degree was reduced gradually. The parabolic variation of the overburden

pressure results in a porosity range from 20 to 30% in the goaf, expressed as

$$\varphi = \begin{cases} 0.00001x^2 - 0.002x + 0.3; & x \leq 100\text{m} \\ 0.2 \quad ; & x > 100\text{m} \end{cases} \tag{1-1}$$

where φ [-] is the porosity and x [m] is the distance from a position in goaf to the working face.

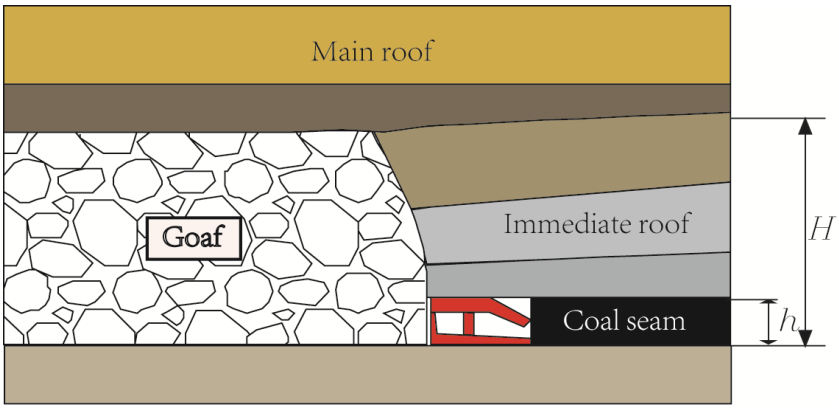

Figure 1-6. Estimate of the height of goaf in a longwall working face.

As porosity is related to the swelling ratio and height of the goaf, it could be estimated by an empirical equation (Liang et al., 2017). Bai et al. (1995) conducted an extensive survey of a large number of mines in China and USA considering the different geological conditions and derived a statistical regression formula which evaluates the height of the goaf (Figure 1-6),

$$H = \frac{100h}{c_1 h + c_2} + c_3 \tag{1-2}$$

where H [m] is the height of goaf; h [m] is the extraction thickness; and c_1, c_2 and c_3 are coefficients that reflect the lithology of the surrounding rock. For average conditions in the goaf area in a coal mine, c_1 = 4.7 m^{-1}, c_2 = 19 and c_3 = 2.2 m were adopted by (Yavuz, 2004).

The swelling ratio of the goaf, K_P, is estimated by

$$K_P = 1 + h/H \tag{1-3}$$

According to the definition of the swelling ratio, porosity is given as

$$\varphi = 1 - \frac{1}{K_P} \tag{1-4}$$

The swelling ratio of the goaf usually ranges 1.3–1.7 (Palchik, 2002); thus, the porosity of the goaf is estimated as 23-41%.

1.4.2 Mechanical modulus of goaf area

Deformation modulus of goaf have been measured by large scale in-situ tests and from detailed laboratory studies. Wardle (1983) conducted an in-situ test of caved waste piles from the roof failure in an Australian coal mine. The result showed a linear stress-strain curve and the elastic modulus was estimated as around 21.4 MPa at a maximum stress of 1.37 MPa. Meanwhile, Smart and Haley (1987) used a hydraulic jacking apply on a stone-built pillar in the United Kingdom, got a result of 20.7MPa for the elastic modulus under a vertical pressure of 5.5MPa. Kose and Cebi (1988) suggested a wide interval such as 15–3500 MPa for the modulus of elasticity value for goaf material. Xie et al. (1999) suggested the formula for determination of the modulus of elasticity of goaf material with respect to time. Su (1991) presented the elastic modulus 72 to 2900MPa to reflect the bilinear behavior of the goaf. Xie (1993) showed that the modulus of elasticity, Poisson's ratio and the density of the goaf material change with time. Yavuz and Fowell (2004) proposed a value of 0.495 for the Poisson's ratio of the goaf material in the Tuncbilek region. Fujji (2011) measured the Young's modulus of clastic-rock in the old closed roadway in the 300m deep at the Kushiro coal mine, Japan. The test measured with a Goodman jack and provided a value of 500MPa around the borehole in the clastic-rock.

Meanwhile, Pappas and Mark (1993) conducted a series of laboratory experiments to

measure the deformation modulus of the goaf material. They used the size-scale-down method to simulate the goaf fragments size distribution in lab-scale, and the secant modulus was 0.7-63 MPa over the porosity (void ratio) from 0.1 to 0.8. The elastic modulus used in numerical simulation showed a relatively higher and wider values from 6.9 to 2400 MPa for the goaf modulus. Following the rule for estimating the modulus presented by Peng (2017) , Hsiung (1985) proposed the elastic modulus should be based on rock type and porosity in the goaf.

1.4.3 Permeability in the goaf area

Permeability is a key factor to estimate the capacity of a material allowing fluids to pass through it without changing or displacing the medium structure. Underground longwall coal mining causes large scale disturbances of the surrounding rock mass leading to the variation of stress and fragments of the rock mass. Goaf area is an abandoned space suffered from an irrecoverable damage during the mining operation. The clastic condition results in a much higher permeability compared with intact or fractured rock. Accurate knowledge of permeability in goaf is essential for methane production, ventilation, methane control and operation safety during and after the mining operation. For example, during the mining operation, goaf behind a working face contains high porosity (void ratio) due to fragmented rock pieces and may result in air leakage into the goaf zone or flow from surrounding formations into the working face; The air leakage into the goaf may probably cause coal spontaneous combustion resulting from the oxygen concentration increase (Figure 1-7).

Beside, when an underground mine ceases coal production, methane gas continues to flow into the underground workings through the process of desorption from residual coal left in the goaf. For gassy mines this desorption process will last for many years. This desorption process has a long-term potential in risks, such as explosion on the surface and surrounding public as well as the greenhouse gas emissions.

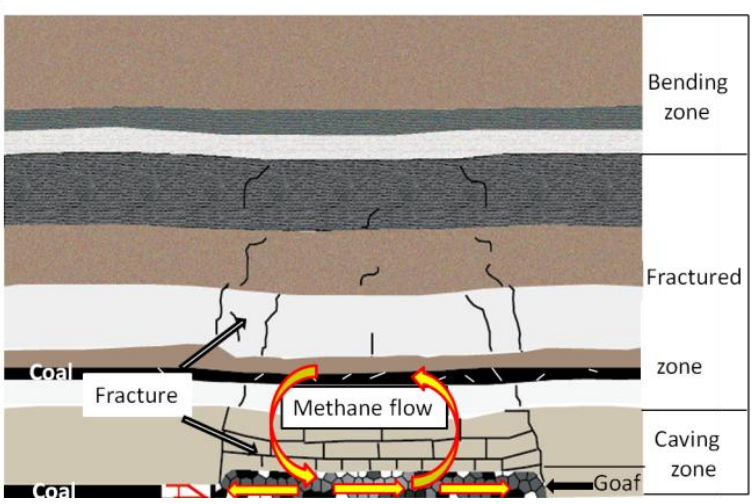

Figure 1-7. Methane flow in the goaf and the interaction with adjacent areas.

Mostly, the permeability measurement techniques are used by the industry, such as wireline-log measurement, laboratory measurement on core samples and well testing. Some studies have conducted the permeability using crushed materials in the laboratory (Li et al., 2018). Ma et al. (2016) measured the seepage properties of different rocks including crushed sandstone, limestone, mudstone, and coal by a self-designed water-flow apparatus. Peng and Loucks (2016) conducted permeability measurements on the crushed rock by gas-expansion method. However, in the field, direct measurement of permeability through the goaf areas are extremely difficult because of the inaccessibility to the internal space of goaf (Adhikary and Guo, 2015). The *in-situ* investigation on the goaf has been very limited. Fujji et al. (2011) conducted an in-situ measurement using a long-drilled hole and provided the permeability data ranging from 1 to 100 d (darcy). However, the region they investigated was the 50-year goaf in which fracture and cleat were completely closed.

Some studies presented permeability values based on volumetric strains and geomechanical calculations. Brunner (1985) used permeability values of goaf ranging from 10^5 to 10^7 d in his ventilation simulation. Ren et al. (1997) proposed a permeability of 10^2 d in a compacted goaf. Whittles et al. (2006) reported a range of 10^4

to 5×10^5 d. Szlazak (2009) estimated the permeability ranging from 5.07×10^3 to 1.01×10^6 d based on the resistance of the rock roof stratification from the caving. Karacan et al. (2007) presented a permeability range of 1×10^5-4×10^5 d according to the *K*-*C* equation combined with a base permeability coefficient. Karacan (2011) proposed a predictive approach to calculate the porosity and permeability from the size distribution of broken rock material in a goaf by combining fractal scaling in porous medium with the principles of fluid flow.

1.4.4 Seismic properties propagating through the goaf area

A number of studies were conducted to investigate the goafs and obtain the goaf parameters. At present, geophysical methods to detect the characteristics of goafs can be classified into surface and subsurface techniques (Wang et al., 2008). Because of its reliability and low operating costs, the seismic detection method is widely applied in the field.

For example, the "Mine Void Detection Demonstration Projects" carried out by the USA Mine Safety and Health Administration (MSHA) consisted of 11 sub-projects within a total of 14 projects that were based on seismic methods (Ge et al., 2008). However, most investigations were conducted using indirect seismic methods, such as surface (Gochioco, 2000; Li et al., 2011), borehole (Cao et al., 2015; Chen et al., 2015; Luxbacher et al., 2008) and in-seam (Cai et al., 2014; Dresen and Rüter, 1994; Friedel et al., 1997) seismic surveys because of the inaccessibility of the goaf and the safety risk inside it. Some field investigations inside goafs (Fujii et al., 2011) have been mentioned in the literature. Furthermore, it has been suggested that the general seismic method provides inaccurate results because of its lower resolution (Barton, 2007). To address this issue, some researchers used high-resolution seismic methods to detect the voids and the stress distribution in the goaf (Poursartip et al., 2017; Tselentis and Paraskevopoulos, 2002). Seismic tomographic imaging, which is analogous to the medical Computer Aided-Tomography Scans, is capable of identifying the location

and condition of the geologic and stress patterns of the inaccessibility such as goaf areas. Many tomography applications in the mining industry use seismic velocity and/or attenuation tomography within a volume enclosed by the seismic source and receiver arrays. The principle of tomography method is based on the energy variation of the seismic reflection or transmission waves reflected or through the anomalies in the strata. At an Australian longwall coal mine, the tomography system was installed to aid in predicting periodic shield loading (Hanna and Haramy, 1998).

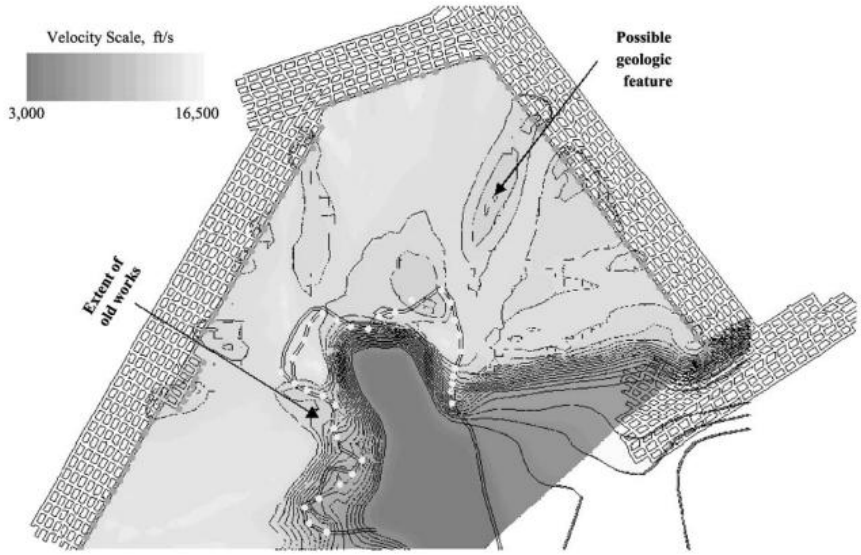

Figure 1-8. Velocity tomogram of the area surveyed to detect old mine works. (The lower velocity areas are indicative of fractured material or old works. Higher velocities are obtained in areas of intact coal) (Hanson et al., 2002)

Attenuation tomography on the shearer was employed as a source in a relative shallow Australian longwall coal mine to determine if roof structural anomalies or fracture zones, along with stress conditions. MSHA (Hanson et al., 2002) has conducted a seismic tomography system to detect the old working near the on-going mining panel (Figure 1-8). The seismic velocity was around 1000m/s in the old working which is obviously less than that of the intact region. Meanwhile, Si et al. (2015) employed arrays of seismic sources and geophones in the roadway at Velenje

coal mine in Slovenia. They showed the velocity transmitted through the goaf areas is 1300m/s by using tomography imaging.

The previous seismic detection method has proved that the seismic method is capable of providing a relatively accurate estimate of the anomalies such as goaf and other fractured or damaged strata. However, selecting the optimum frequency still involves an uncertainty, because the porosity and fragmented coal and rock size distribution in the goaf are not precisely known.

1.5 Effective medium theory for the unconsolidated porous sediment

Goaf area is a space consisting of large void and random-shaped rock masses in different sizes. This kind of formation results in a large number of discontinuities such as voids, joints, fractures and microcracks at all scales. These discontinuities might be aligned in one particular direction or randomly oriented. Generally, effective medium theory is used to assumes that the rock consisting of voids or fractures can be seen as a whole. The compliance of the discontinuities is taken into the average strain of the rock (Lubbe and Worthington, 2006). It means that the reduced modulus leads to the decrease in seismic velocity and the increase in attenuation. Effective medium theories can be used to treat the effect of a porous rock on fluid flow (Kachanov, 1980; Oda, 1985) and seismic propagation (Sayers and Kachanov, 1991; Schoenberg and Sayers, 1995). Eshelby (1957) firstly attempted to explain the reduced modulus resulting from the discontinuity and successfully obtained the elastic modulus of an infinite solid containing ellipsoidal inclusions. Hudson (1981) presented a commonly used model for estimating the effective elastic properties of a transversely anisotropic crack rock This model is based on a simplified analysis of a thin circular crack, considering displacement and stress conditions on the boundaries of the cracks. The model focused not only on the number of the discontinuities, but also the interactions between the discontinuities.

For the porous media, it is commonly to estimate the effective modulus by using Mindlin-Hertz theory.

$$K_{HM} = \left[\frac{C^2(1-\varphi_c)^2}{18\pi^2(1-\nu)^2}P\right]^{\frac{1}{3}} \tag{1-5}$$

$$G_{HM} = \frac{5-4\nu}{5(2-\nu)}\left[\frac{3C^2(1-\varphi_c)^2G^2}{2\pi^2(1-\nu)^2}P\right]^{\frac{1}{3}} \tag{1-6}$$

where K_{HM} [MPa] and G_{HM} [MPa] are the bulk and shear modulus at critical porosity φ_c, P [MPa] is the compressive pressure; K [MPa] and G [MPa], are the bulk and shear moduli of the solid phase, ν [-] is Poission's ratio, and C [-] is the coordination number. However, this theory is most efficient for the case at the critical porosity of the porous media. Therefore, Dvorkin et al. (1995) developed the Hashin-Shtrikman model to estimate the modulus at a certain porosity that is larger or smaller than the critical one.

(a) Hashin-Shtrikman lower model

This model connects two end-points in the elastic-modulus porosity plane. One end point is at the critical porosity which can be obtained by Hertz-Mindlin. The other point is the elastic modulus of the pure solid phase.

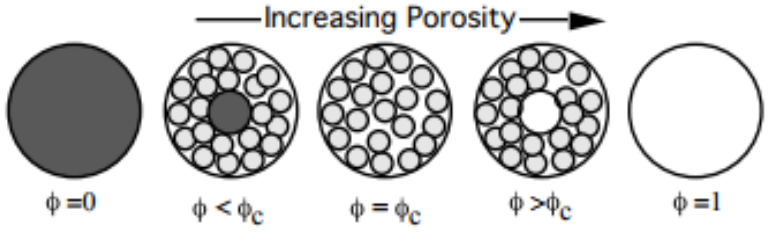

Figure 1-9. Hashin-Shtrikman arrangements of sphere pack, solid, and void (Dvorkin and Nur, 2002).

These two points in the porosity-modulus plane are connected with the curves that have the algebraic expressions of the Hashin-Shtrikman lower model bound for the mixture

of two components: the pure solid phase and the phase that is the sphere pack (Figure 1-9). While this model is only useful for the porosity which is smaller than critical porosity, the higher porosity above critical porosity has to be estimated by the another model by the name of Hashin-Shtrikman upper bounds

(b) Hashin-Shtrikman upper bounds (Helgerud et al., 1999)

This model is analogous to the friable sand model but covers the porosity range above critical porosity. One end point is the critical porosity estimated by Hertz-Mindlin theory (Johnson, 1987). For the higher porosity, empty voids are added to the sphere pack (Figure 1-9). In this case the voids are placed inside the pack in the Hashin-Shtrikman fashion. At porosity $\varphi>\varphi_c$, the concentration of the void phase is (φ-φ_c)/ (1-φ_c) and that of the sphere-pack phase is (1-φ)/ (1-φ_c). Then the effective dry-rock frame bulk and shear modulus are:

$$K_{dry} = \left[\frac{(1-\varphi)/(1-\varphi_c)}{K_{HM}+4/3G_{HM}} + \frac{(\varphi-\varphi_c)/(1-\varphi_c)}{4/3G_{HM}}\right]^{-1} - \frac{4}{3}G_{HM} \tag{1-7}$$

$$G_{dry} = \left[\frac{(1-\varphi)/(1-\varphi_c)}{G_{HM}+Z} + \frac{(\varphi-\varphi_c)/(1-\varphi_c)}{Z}\right]^{-1} - Z$$

$$Z = \frac{G_{HM}}{6}\left(\frac{9K_{HM}+8G_{HM}}{K_{HM}+2G_{HM}}\right) \tag{1-8}$$

Based on the models mentioned above, seismic velocity can be derived from the elastic modulus.

1.6 Seismic attenuation

In order to improve the resolution of seismic detection, the bandwidth frequency of the incident wave should be wider and higher. However, the higher frequency wave is susceptible to the rock strata and to be easily attenuated. Therefore, the extent of the attenuation should be figured out in order to take measures to improve the accuracy of

the seismic detection. We herein discussed the definition of the seismic attenuation and attempted to show the relationship between them.

(a) For the homogeneous media, the amplitude of plane wave is

$$A = A_0 e^{-\beta x} \cdot \varpi(t) \tag{1-9}$$

where A_0 [-] is the initial amplitude of the incident wave; x [m] is the travel distance; ω(t) is the wave function. If the sphere spreading is considered, a factor of sphere spreading (1/x) can be multiplied to the expression.

(b) Quality factor (Q) is another factor to describe the attenuation in terms of the energy loss in one cycle

$$\frac{1}{Q} = -\frac{\Delta E}{E} \tag{1-10}$$

where (-ΔE) is the energy loss per cycle in a material with peak strain energy E. It can be generalized to include the rate of loss of energy expressed by differential form (Lubbe and Worthington, 2006):

$$\frac{1}{Q} = -\frac{1}{2\pi}\left(\frac{dE}{E}\right)\left(\frac{T}{dt}\right) = -\frac{1}{2\pi}\left(\frac{T}{E}\right) \tag{1-11}$$

where T [s] is the period of the propagating wave.

Integrating 1/Q on time, the Equation 1-11 can be converted into

$$E = E_0 e^{-\frac{2\pi t}{QT}} = E_0 e^{-\frac{2\pi x}{QVT}} \tag{1-12}$$

where E_0 [-] is the initial energy at time; t [s] is the travel time of the propagating wave; V [m/s] is the velocity of the material.

Because energy is proportional to the square of amplitude, therefore,

$$A = A_0 e^{-\frac{\pi x}{QVT}} \tag{1-13}$$

Equation 1-9 is equal to Equation 1-13, therefore,

$$\beta = \frac{\pi}{QVT} \tag{1-14}$$

(c) Logarithmic reduction (δ) is the logarithmic value of the ratio between the neighbor peak amplitude after traveling one wavelength

$$\delta = \ln\left(\frac{A_1}{A_2}\right) \tag{1-15}$$

where β is the attenuation in the unit length. So the attenuation in one wavelength is equal to δ. A_1 and A_2 are the amplitudes of the neighbor peaks

$$\delta = \lambda\beta = \frac{V}{f}\beta \tag{1-16}$$

where λ [m] is wavelength.

(d) Another property is decibel attenuation factor $\hat{\beta}$ (db/m) which is defined as the decibel attenuation of the amplitude after traveling one wavelength.

$$\hat{\beta} = 20\log_{10}\frac{A_1}{A_2}\ (\text{db/m}) \tag{1-17}$$

Compare 1-16 and 1-17:

$$\hat{\beta} = 8.686 \times \delta \tag{1-18}$$

Consequently, the relationship between the different attenuation factor can be express as

$$\frac{1}{Q} = \frac{\delta}{\pi} = \frac{\beta\lambda}{\pi} = \frac{V\beta}{\pi f} = \frac{\hat{\beta}}{27.3} \tag{1-19}$$

1.7 Objectives of present research

As mentioned above, goaf is an area filled with different sizes of irregular-shaped rock fragments. A large number of discontinuities such as voids, joints, fractures and microcracks at all scales are observed in the goaf. The mass-distributed voids and complicated geometric skeleton results in the reduction of seismic velocity and increase of the attenuation. For the single fracture or aligned fractures, Pyrak-Nolte et al. (1987) has posed time delay at the discontinuity to predict the P and S-wave velocities in rock containing fractures. Gibson and Ben-Menahem (1991) and Boadu and Long (1996) presented elastic wave transmission model for the seismic attenuation passing through a system of aligned fractures. However, for the compressed porous rock, the theoretical model for the seismic attenuation needs to be further studied.

Meanwhile, because both of the seismic properties (velocity or attenuation) and hydraulic property such as permeability are related to volumetric and geometric features of the rock formation. A number of researches have attempted to relate the seismic characters to the permeability. For an example, Prasad (2003) used hydraulic units to predict the permeability by seismic velocity. Pyrak-Nolte and Morris (2000) tried to investigate the relation between the fracture permeability and seismic anisotropy to extract permeability information from seismic data.

Since goaf area performed is void space and more tortuous geometric skeleton, the correlation between permeability and seismic characters is different from that of the fractured rock.

In the meantime, the existence of goaf in the underground has a potential risk on the constructions on the ground surface above goaf. Especially, when earthquake happens, the propagation of earthquake wave may be affected by the presence of goaf. The previous research used a shaking table to observe the seismic response above goaf (Aydan Ö., 2003) in laboratory measurement. Some researchers also employed

simulation method to study the effect of large-scale goaf on the ground seismic response in the mining area. However, the non-linear elastic characteristic of goaf and the damping effect of goaf on seismic propagation have not yet been clearly studied.

Therefore, in this study, we attempted to establish the models to predict the seismic attenuation in the compressed porous rock. And corrected factor is propose by experiment to improve the precision of the estimated results from the empirical model. Meanwhile, we established an empirical equation including effects of the tortuosity factor and porosity with the seismic velocity and attenuation to predict the permeability in the compressed porous rock. Additionally, the damping coefficient of goaf under different conditions such as depth or compaction time can be estimated based on the laboratory measurement, and try to study the seismic response on the ground surface above goaf in the coal mine areas.

The innovation of this research can be summarized as four points;

1. The previous seismic investigations modeled the goaf as an intact rock or fully void space. The wavelength of seismic wave in the discussion is much larger than the size of void or rock mass. As a result, the porosity or void space can not be clearly detected. In this research, it was figured out that the optimal ratio of wavelength and the size of rock mass can be used to estimate the porosity of porous layers.

2. The seismic attenuation in the unconsolidated porous rock like goaf area has not been studied previously. Most of the current theories focus on the intact or fractured rock rather than the porous rock. Therefore, this research attempted to establish a new model to estimate the seismic attenuation in the unconsolidated porous rock based on the laboratory measurement and theoretical approaches. The prediction shows a good agreement with the measured data.

3. The correlation between permeability and seismic properties have been studied by numerous researchers. However it is still difficult to estimate gas permeability in the

goaf area. This research has presented the model for the relationship between gas permeability and seismic velocity and attenuation of the porous rock specimen. The predicted permeability by the model showed a good consistency with the measured values. This correlation can be used to estimate the permeability in the actual goaf based on the seismic measurement data.

4. The seismic damage above the goaf areas have been studied by some researchers based on simulation analysis. But most of them treated the goaf area as intact according to the effective medium theory. Those results in the adsorption of seismic energy through the goaf only base on the variation of mechanical modulus. In this research, the damping coefficient has been presented based on the laboratory seismic measurements to describe the adsorption effect of goaf on the seismic energy. The simulation results of seismic response on the ground surface above goaf for different depths and porosities can be estimated more reasonable and accurate.

1.8 Summary of chapters

Chapter 2 firstly elaborates the experimental apparatus and sample preparation, and introduces the experimental procedures, and shows experimental procedures of the seismic and permeability measurements. Experimental apparatus is comprised of transient ultrasonic measurement and steady-state gas permeability measurement. Coal and rock particles in diameter of 0.12-1.0 mm were used to form the cylindrical porous samples by high-pressure compression machine. The P-wave seismic velocity and attenuation as well as the gas permeability were measured on the samples in different porosities, rock particle sizes and types of rock.

Chapter 3 presents a new seismic attenuation model (the B-R model) based on the multi-fractured rock attenuation model by Boadu and Long (1996). The B-R model accounts for (i) greater attenuation through fragmented rock due to increased contact points between the particles, and (ii) decreased attenuation caused by network

propagating through the porous media. And this model is applied to the laboratory measurement results of ultrasonic wave attenuation using compressed porous rock and coal samples and good agreement has been found for various porosities, particle sizes and wavelength.

Chapter 4 focuses on the tortuosity (τ) factor and effect of porosity (φ) on gas permeability in the cylindrical compressed porous rock samples, they are found to be related to the functions of seismic velocity variation and attenuation change (ξ and η), respectively. The function, η showed a linear relationship with the square root of the τ over the range of τ = 5–10. The function, ξ showed an approximately linear relationship with the porosity part of the *K*-*C* equation. A new empirical equation to estimate the permeability of the compressed porous samples has been presented by modifying the Kozney-Carman (*K*-*C*) equation with seismic velocity and attenuation. The permeability estimated by the empirical equation showed good agreements with the measured permeability of the compressed porous samples.

Chapter 5 describes numerical simulation study to analyze the earthquake damage on the ground surface above goaf areas in coal mine area. The elastic modulus of goaf region is based on compressive strength of the intact rock and porosity as well as the compaction time. The damping coefficient of the goaf is obtained by B-R model presented in Chapter 3. Numerical simulations are carried out for different conditions to study the acceleration, characteristic period, displacement on the ground surface above goaf in different geologic and geometric condition.

Chapter 6 concludes the results of the experiments and established models on seismic characteristics and permeability as well as the numerical study and field estimation. Finally, the limitations of the present study are discussed, and the suggestions for the future research are proposed.

Chapter 2: Laboratory measurements of ultrasonic and permeability of the compressed porous samples

2.1 Introduction

The measurement of goaf area is a significant and imperative work for evaluating the safety of the underground and surface environment. However, it is difficult to conducted measurement directly in a closed goaf. This chapter introducs a method to measure the properties of the goaf area by simulating the condition of the goaf in laboratory measurement. Since Ebrom and McDonald (1994) reported that certain features may be reproduced on a small-scale in the laboratory measurement for seismic modeling. For reservoir modeling, the size of the object is usually set so that the ratio between the wavelength and size of the object is the same as in the laboratory setting. We therefore attempted to use the similar ratio of wavelength to rock or coal particle size for the measurement with ultrasonic wave. Meanwhile, according to the observation by Pappas and Mark (1993) in a goaf using a high-resolution camera, size distribution of the fragments in the goaf was approximately 60–450 mm. The majority of the fragments were 120-250 mm. Meanwhile, the P-wave seismic velocity and wavelength used in the usual field measurement is in the range of 1000-1500 m/s and 10-200 Hz. The ratio of wavelength and fragment size is from 11-120. In present experiments, coal and rock particles in diameter of 0.12-1mm were compressed into cylindrical porous samples under a high pressure by a molding machine. The size distribution of the particles have the analogous size distribution as the fragments in the actual goaf to keep the similar mechanical modulus. Ultrasonic wave frequency in the range of 37-250 kHz was applied for these samples consisting of 0.12-1mm in diameter. The ratio of wavelength and particle size was set in the range 6-140 which covers the range of the field measurement (Table 2-1).

Table 2-1. Comparison of parameters used in previous field studies and present laboratory measurements

Property	Si et al.(2015)	Hanson et al.(2002)	Present measurements
Field/ Laboratory	Field	Field	Laboratory
Type of coal	Lignite (Slovenia)	Bituminous (USA)	Bituminous (China)
Frequency, *f* (Hz)	80	150	27k-500k
P-wave velocity in the goaf (V_{PG}, m/s)	≈ 1300	990	400-1100
Mass or Particle size *D* (mm)	≈150	≈150	0.12 to 1
λ/D	116	40	6–120

2.2 Preparation of compressed porous samples

Three rock types of core samples were used in this study (sandstone, limestone and bituminous coal) to measure the mechanical parameters, wave velocities and attenuation as well as gas permeabilities. Sandstone core was Berea sandstone from West Virginia, USA. Limestone was from Kagumeyoshi formation located in northern Kyushu, Japan. Bituminous coal sample was from No.3319 panel (-300 m) of Daliuta coal mine in Inner Mongolia, China (Figure 2-1).

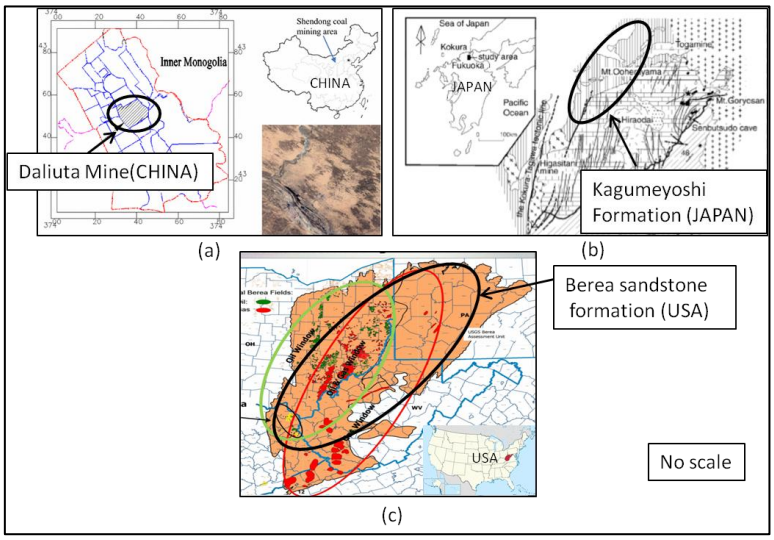

Figure 2-1. Source of the rock samples (a) bituminous coal, (b) limestone and (c) sandstone (Fukuyama et al., 2004; Luan et al., 2018; Pepper et al., 1954).

2.2.1 Intact samples

All of the samples were preserved in excellent condition after extraction to keep the original properties. Before the mechanical and wave measurement, the samples were put into the drying oven at 80^{o}C for 7 days to remove the effect of the moisture. The cylindrical intact rock was cut from the sandstone and limestone rock mass by coring bit (Figure 2-2 *Left*) with 40mm in diameter. The coal intact samples were cut into a cuboid with the size of 6×6×8 mm rather than a cylinder to preserve its integrity. The end faces of the samples were cut roughly parallel with an edge saw and then polished with the surface grinder (Figure 2-2 Right).

Figure 2-2. Coring bit (Left) and surface grinder (Right).

In this way, intact rock samples (Figure 2-3) were made for measuring the mechanical properties. Mechanical parameters of the intact rocks are listed in Table 2-2.

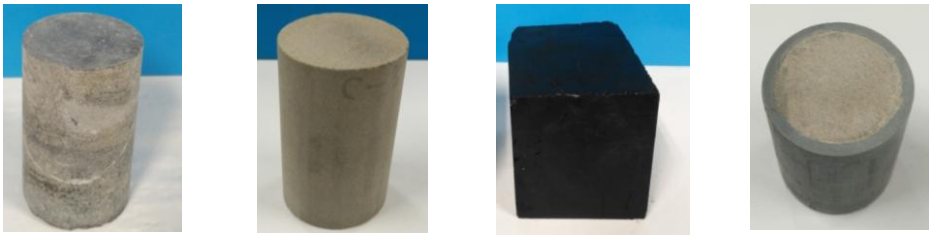

(a) (b) (c) (d)

Figure 2-3. Intact samples of (a) limestone, (b) sandstone (c) bituminous coal and (d) sandstone with PVC pipe.

Figure 2-4. X-ray fluorescence equipment for rock composition measurement.

Mineral compositional of sandstone and limestone samples were measured by small rock particle in 0.01mm using X-ray fluorescence (Figure 2-4). The composition of coal were measured by thermal method (Figure 2-5) to obtain the primary content in coal samples. The mineral composition of the samples are shown in Table 2-3.

Figure 2-5. Electric high-temperature furnace for coal composition measurement.

Table 2-2. Physical parameters of intact samples used for present measurements

Properties / Samples	Limestone	Sandstone	Coal
Young's modulus, E (GPa)	17	8	1.7
Bulk , B (GPa)	15.5	6.55	1.67
Possion ratio, v (-)	0.32	0.22	0.33
Shear modulus, G (GPa)	6.3	4.70	0.63
Density, ρ (kg/m^3)	2607	2551	1545
P-wave velocity, V_{PI} (m/s)	4830	2350	2150
S-wave velocity, V_{SI} (m/s)	1550	1157	638

Table 2-3. Mineral composition of the intact samples

Coal		Sandstone		Limestone	
Moisture (%)	3	SiO_2 (%)	93.13	CaO (%)	54.24
Fix carbon (%)	69.8	AlO_3 (%)	3.86	MgO (%)	0.28
Ash (%)	3	Fe_2O_3 (%)	0.11	P_2O_5 (%)	0.033
Volatile matter (%)	16.2	FeO (%)	0.54	I.R. (%)	2.6
Sulfur (%)	2	MgO (%)	0.25	Sr (%)	0.14

2.2.2 Compressed porous samples

The rock and coal particles were prepared by crushing the dried core samples. The particles were sieved into three groups according to particle size, with diameter ranges of D = 0.12–0.25 mm, 0.25–0.50 mm and 0.50–1.00 mm. The particles were compressed in cylindrical PVC pipes that were surrounded by a stainless-steel socket (Figure 2-6 upper panel).

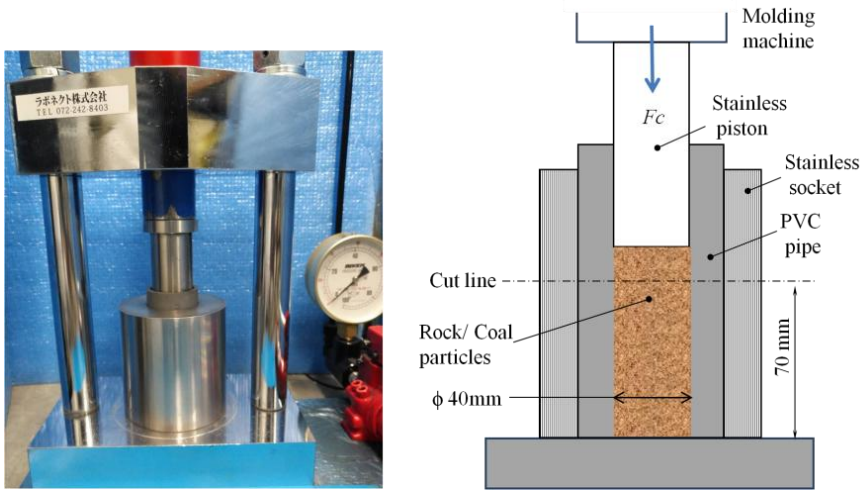

Limestone Sandstone Coal

Figure 2-6. Press molding machine (upper panel) used to form the porous rocks and coal samples (lower panel).

The cylindrical porous samples were compressed in the PVC pipe by a stainless-steel piston 39.8 mm in diameter under high compression using the press molding machine. The porosities of the porous samples were controlled by the compression force applied to the particles in a stepwise manner to maintain the homogeneity and consistency of the samples. After the compression stage each sample was cut to a length of 70 mm and the surfaces on both ends were smoothed (lower panel in Figure 2-6). The porosities of the samples were controlled by measuring the stroke of the hydraulic piston using the laser rangefinder and the following equation

$$\varphi = 1 - \frac{m}{AL_S\rho_{mat}} \tag{2-1}$$

where φ is the porosity; m [kg] is the mass of the sample; A [m^2] is the base area of the sample; L_S [m] is the length of the sample; and ρ_{mat} [kg/m^3] is the matrix density of the rock or coal sample. The porosity, therefore, can be changed by varying the mass, or the length of the sample depending on compressive pressure.

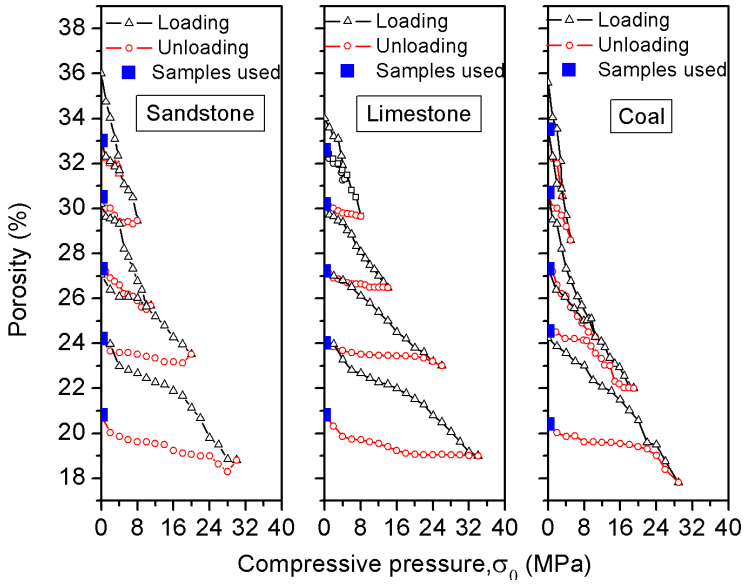

Figure 2-7. Porosities of the compressed porous samples under stepwise compression.

The loading and unloading process (Figure 2-7) were recorded to measure the porosity and Young's modulus. In each step of compressing, it last for 5 to 10 minutes. At the maximum stress in the loading process, the loading machine applied on the samples

for 30 minutes to remain samples less rebound. Rebound of the particles was considered by subtracting the rebound portion from the entire stroke of piston while calculating the porosity. Three different particle sizes were used for the samples: 0.5-1.0mm, 0.25-0.5mm and 0.12-0.25mm. Each group consists of five samples over the porosiity from 0.21-0.33 with intertal of 0.03. Additionally, each sample were measured three times by repeating molding and obatin the average to keep the reliability and accuracy. In this way, total 135 samples were made for seismic and permeability measurements.

2.3 Microstuctures in compressed rock samples

Microstructural analysis was conducted on thin sections impregnated with fluorescent red-dyed epoxy to assess the characteristics of voids in the compressed porous samples by using polarizing microscope (Figure 2-8). The samples shown here (Figure2-9) were selected as the representatives with the typical distinctions of different porosities. It can be observed the coal particles were intricately aligned and exhibited weak connetivity for the higher porosity. The size of the pores among particles showed similar scale to the particle size for the higher porosity samples.

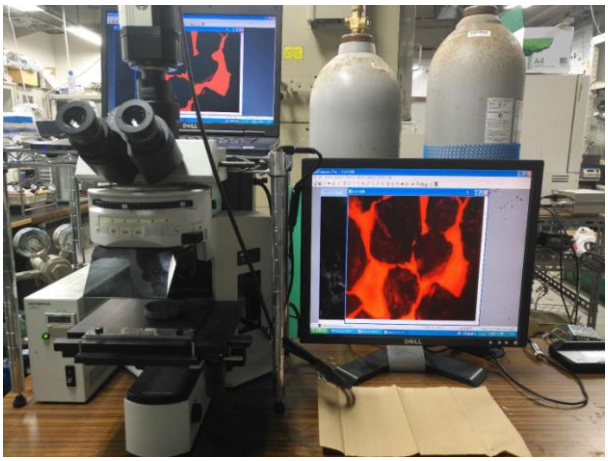

Figure 2-8. Acquision of the microstrucure of samples.

Differ from the intact rock involing thin and long fractures, the crushed material was dominated by circular pores with different sizes and thin throat (Lamur et al.,

2017). The particles showed weaker link and surrounded by larger pores which might affect the seismic propagation and gas flow because no cementation was present in the compressed porous material.

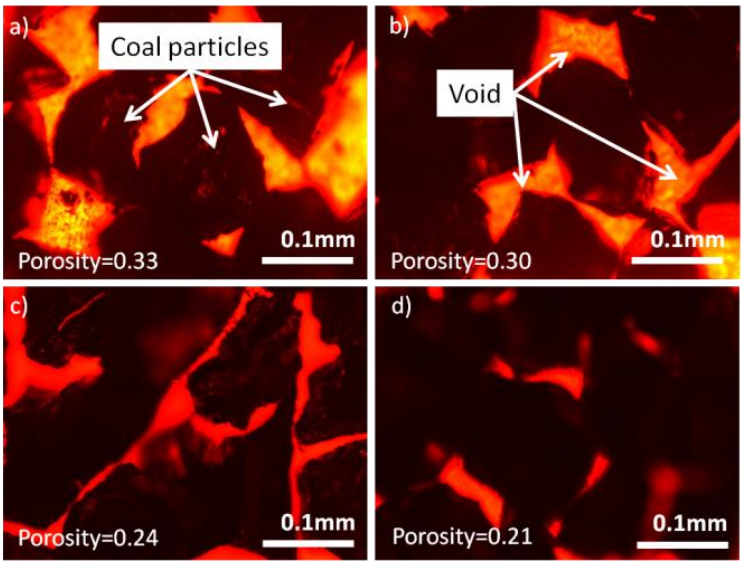

Figure 2-9. Microstructure of compressed porous samples consiting of 0.12-0.25 mm coal particles.

2.4 Effective stress and porosity

Before the seismic and permeability measurements, the mechanical properties of the compressed porous samples were measured. The influence of the effective stress on the porosity for low-permeability samples is relatively small. However, for high permeability material, such as crushed rock, the effective stress is not negligible because of the material's vulnerability to compression. Shi and Wang (1988) presented the empirical equation relating the porosity change to the effective stress:

$$\varphi = \varphi_0 \exp(-\alpha \sigma_{\max}) \tag{2-2}$$

where φ_c [-] is the critical porosity, σ is the maximum effective stress at each cycle of compressive stress loading and α is the power constant. In our measurement, the maximum stress (σ_{max}) of each loading–unloading cycle (Figure 2-7) was used as the

effective stress in Equation 2-2. The porosity under σ_{max} at each cycle was at zero compression stress rather than at σ_{max} because of the rebound of the unloading particles. Athy (1930) and Dickinson (1953) derived α values in the range of 0.01 to 0.1 MPa^{-1} for shale. Dickinson and Suczek (1979) and Shepard and Bryant (1983) reported α values of 0.5×10^{-2} to 5×10^{-2} MPa^{-1}.

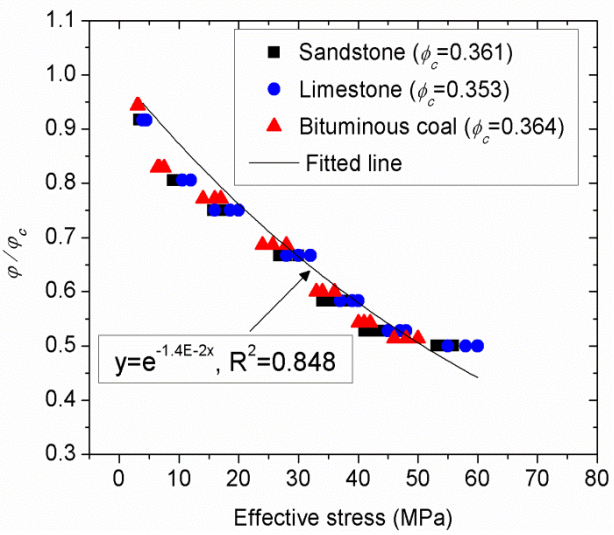

Figure 2-10. Effective stress versus porosity.

In our study, the crushed particles were slightly packed to an initial height, the critical porosity were measured shown in Figure 2-10. The porosity (φ) can be calculated by Equation 2-2. With increased effective stress loading on the compressed porous samples, φ/φ_c and the effective stress exhibited an exponential relationship (see Figure 2-10). The fitting curve yields α = 1.412×10^{-2}, 1.36×10^{-2} and 1.46×10^{-2} MPa^{-1} for the sandstone, limestone and bituminous coal, respectively. The results indicate that α decreases with the increasing rock hardness. Based on these results, the average value of α for the three types of rock samples was set as 1.4×10^{-2} MPa^{-1}.

2.5 Young's modulus of compressed porous samples

According to Fumagalli (1969), the grain size distribution of the actual rockfill materials could be proportionally scaled down and accurately represented for laboratory tests. Furthermore, Hardin (1985) provided theoretically that the strength

and deformation characteristic of the small particle size materials could be considered the same as those of the large particles. It has been proved by Papps and Mark (1993) that the elastic modulus of the fragmented rock is independent of the size of fragments, but is strongly related to the size distribution.

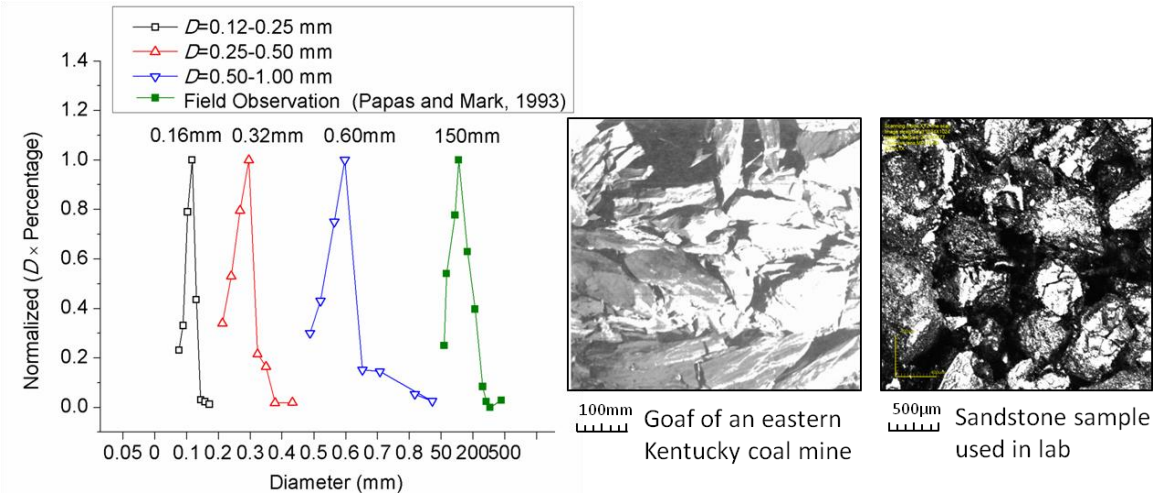

Figure 2-11. Size distribution of fragmented rock masses in the actual goaf and sandstone particles in our laboratory measurements.

Therefore, in this laboratory measurement, average particle size was used by reducing the size of the fragments of the actual goaf (Pappas and Mark, 1993) to small particles. (Figure 2-11). It was presented by Pride (2005) that grain packs having unimodal grain-size distributions have elastic moduli that are independent of grain/particle size. Therefore, we used the similar particle size distribution as the actual goaf (Figure 2-11) to form the samples, and measured the Young's modulus for different porosities. It can be seen that the Young's modulus of the sample is independent on the particle size. The three groups of particle size showed the similar values. The sandstone and limestone samples exhibited larger Young's modulus than that of bituminous coal because of the intrinsic rock properties. Overall, the Young's modulus of the compressed porous samples, E (MPa) are fell into the range of 200-5000 MPa (Figure 2-12). Compared to the in-situ measurement (Table 2-4), the E values of our samples in the laboratory show similar ones of the field Young's modulus.

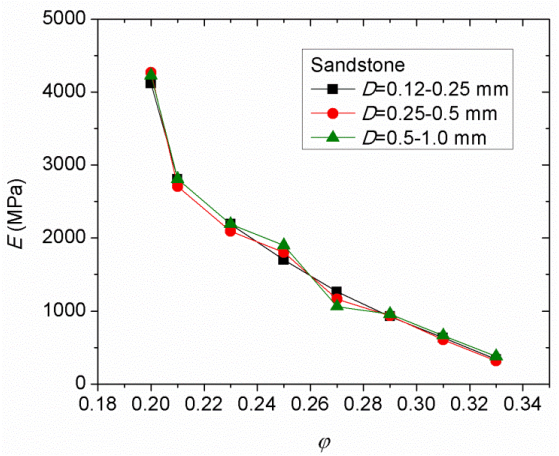

(a)

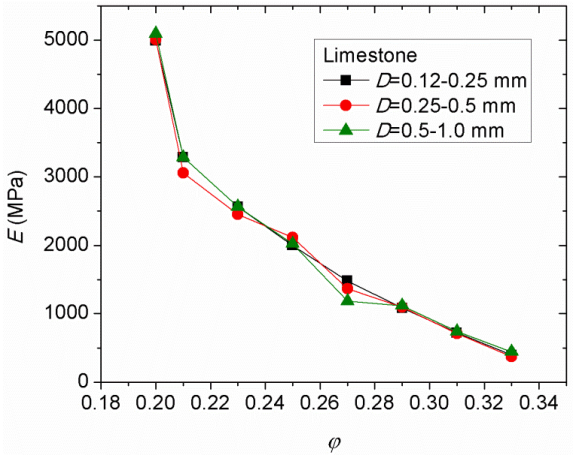

(b)

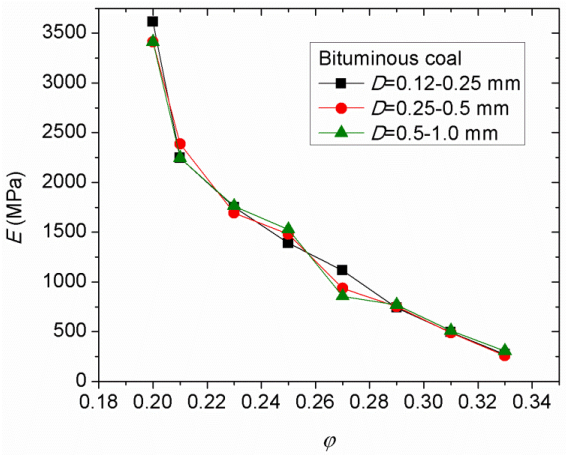

(c)

Figure 2-12. Young's modulus of compressed porous samples. (a) sandstone, (b) limestone and (c) bituminous coal

Table 2-4. Comparison of parameters measured in the previous field studies and present laboratory measurements

Property	Fujji (2011)	Wardle (1983)	Smart (1987)	Present lab measurement
Location	Japan	Australia	UK	Laboratory
Type of goaf	Compacted goaf	Loose goaf	Loose goaf	Porous sandstone
Elastic modulus (MPa)	500-5500	20-	21-700	60-4800

2.6 Seismic measurements

The seismic wave velocity and attenuation were measured by the pulse transmission apparatus (Pundit Lab+) (Figure 2-13 left). For the case of compressed porous samples, the transducers were inserted into the cells with two springs in case of the compressive pressure. The measurements were done under ambient pressure. The transducers were driven with high voltage (500V) and provided a wide range of ultrasonic frequencies from 24 to 500 kHz.

A square pulse was generated from the transducer and the received signals were displayed on the screen of an oscilloscope with an integrated a software (Punditlink) which controls the measurement, to the seismic processing system (Pundit Lab+) for storage and the subsequent data processing. Fast Fourier Transform (FFT) was used to convert time-history curve into spectral amplitude. The attenuation of the wave was calculated as

$$\beta = -\frac{1}{L_s} ln \left[\frac{A_1(f)}{A_0(f)}\right] \tag{2-3}$$

where f [Hz] is wave frequency; A_0 (f) is the spectral amplitude of the incident wave; $A_1(f)$ is the spectral amplitude of the transmitted wave; and L_S [m] is the propagation length on straight line between two transducers .

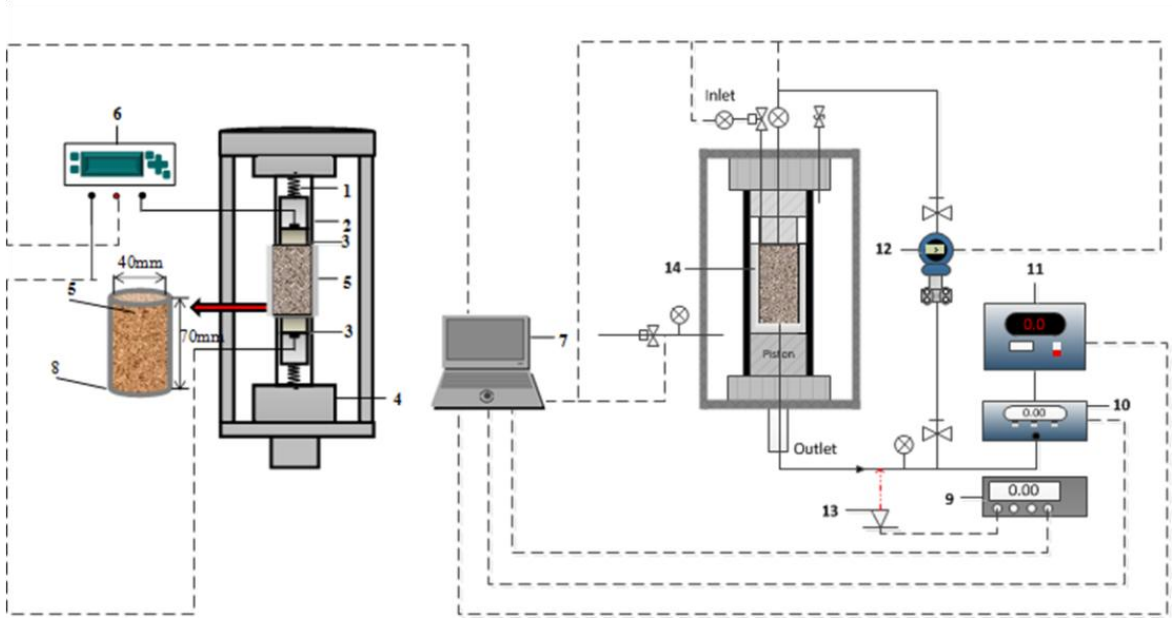

Figure 2-13. Apparatus of seismic and permeability measurement. (1) spring; (2) piston; (3) transducers; (4) pedestal; (5) compressed porous sample, $A = 1.26 \times 10^{-3}$ m^2; (6) pulse transmission apparatus and analyzer (Pundit Lab+); (7) storage and software; (8) PVC pipe, 40 mm inner diameter; (9) display; (10) gas flow meter controller; (11) gas flow meter; (12) differential gas pressure gauge; (13) laser rangefinder; (14) PVC cup

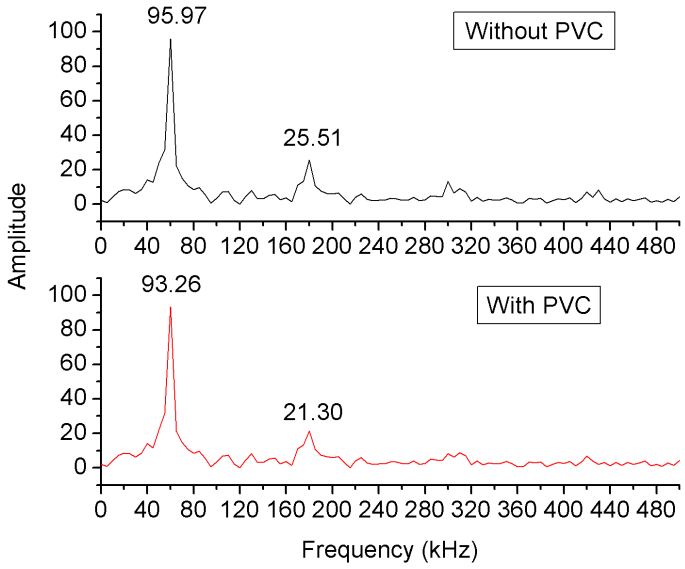

Figure 2-14. Spectra of the intact sandstone sample (upper) and sample with PVC casing (lower).

Seismic measurements of the compressed porous samples were performed with the PVC casing in place. To check the effect of the PVC pipe on the seismic measurements of the compressed sample, we compared the seismic characteristics of the intact sandstone specimen with that of the same specimen inside a PVC pipe, filling the gap between the sample and the pipe with Epoxy resin (Figure 2-3-d). Figure 2-14 shows the spectra of the two samples. The results indicate a very small difference (within 3%) between the peak amplitudes of the two cases. Therefore, the effect of the PVC casing on the seismic attenuation can be neglected.

2.6.1 Seismic attenuation

2.6.1.1 Effect of frequency on the seismic attenuation

According to Jones and Nur (1983), the seismic attenuation is caused by 2-15 depicted the seismic attenuation in the compressed porous samples consisting of three different rock types over the porosity from 0.21 to 0.33.

As is shown in Figure 2-15 that seismic attenuation of the three different types of rock noticeably increase with the increasing porosity. Even though the values of attenuation are different for the different types of rock, while, all of them have showed strongly dependent on frequency. As the frequency increased from 37 to 250 kHz, the attenuation approximately increased from 20 to 50, 10 to 50 and 30 to 90 1/m for three types of rock, respectively. Meanwhile, the values of attenuation under different frequencies tend to close with the porosity decreased.

This illustrates the attenuation is more susceptible to the frequency change at larger porosity. The discrepancy of seismic attenuation among different rocks is because the stiffness between the rock particles are different. The compliance of the contact surface between limestone and sandstone particles are larger than that of bituminous coal. Therefore, the seismic wave propagated through the particles are more smooth resulting from the less compliance.

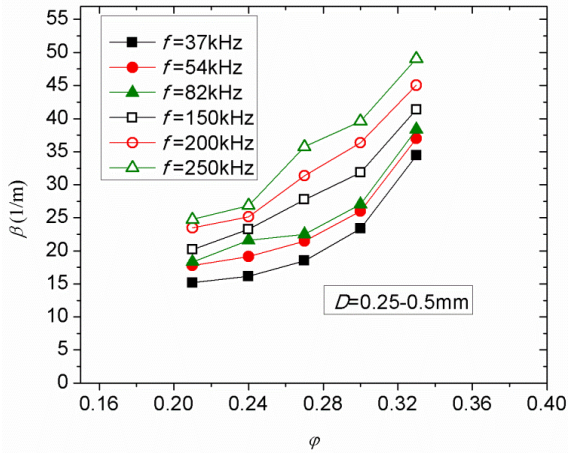

(a)

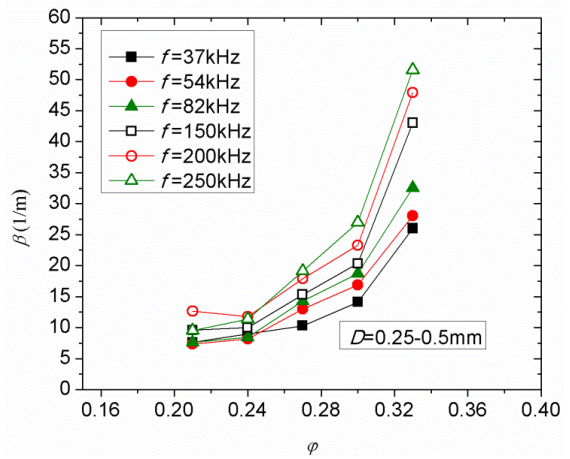

(b)

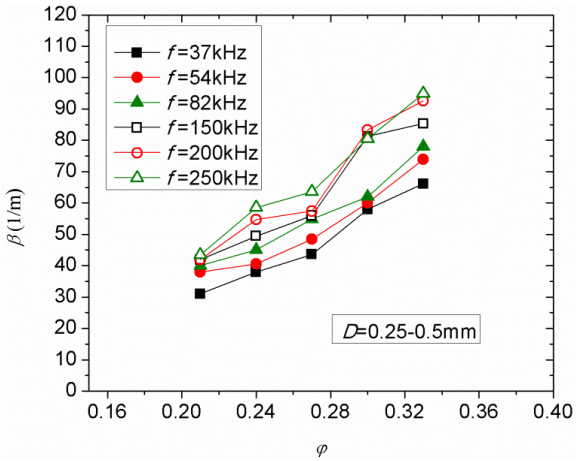

(c)

Figure 2-15. Seismic attenuation against porosity for different frequencies. (a) sandstone, (b) limestone and (c) bituminous coal

2.6.1.2 Effect of particle size on attenuation

Figure 2-16 shows the effect of particle size on the seismic attenuation.

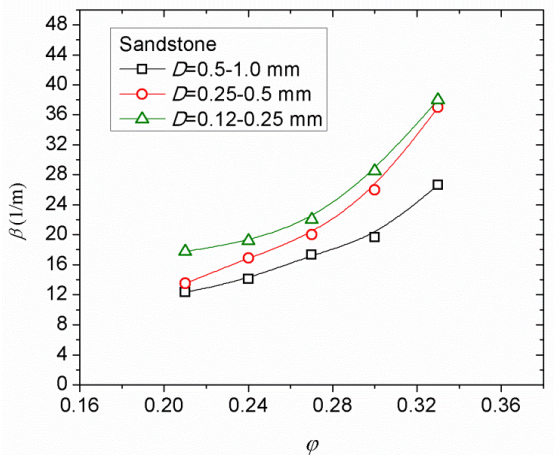

(a)

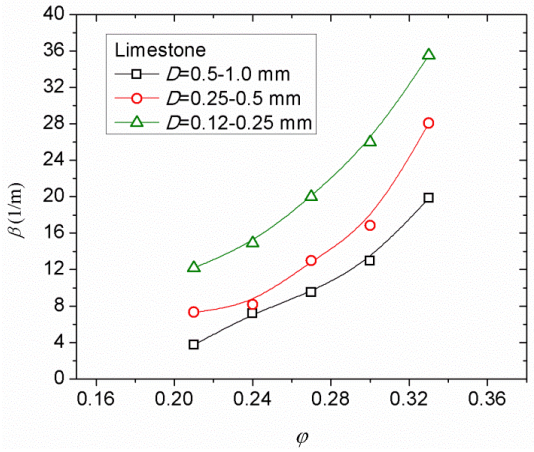

(b)

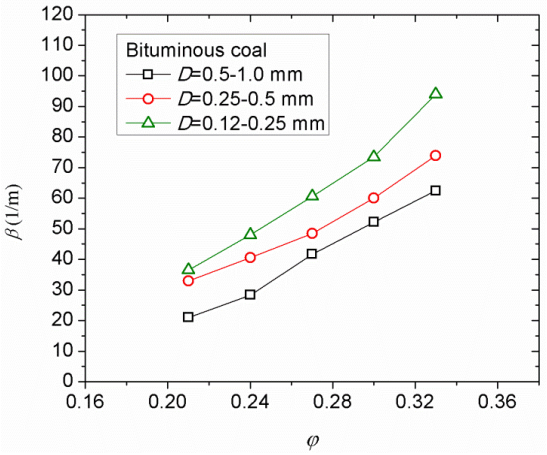

(c)

Figure 2-16. Seismic attenuation against porosity for different particle size. (a) sandstone, (b) limestone and (c) bituminous coal

Pyrak-Nolte et al. (1990) performed laboratory experiments using compressional and shear waves transmitted normal through the parallel fractures. The results showed the seismic attenuation is dependent on the number of contact surface and the stiffness of the contact surface. In our measurements, the length of the sample is constant, therefore, the different sizes of particles results in the varied number of contact surface.

It can be seen that the seismic attenuation increases rapidly as the reduction of particle size. The slope of the attenuation versus porosity curve for the smaller particles shows larger than that of the larger particles. This illustrated the attenuation in the smaller particles is more susceptible to the porosity change. While, the attenuation for three particle sizes remained similar level when the porosity dropped to φ=21%. It means the attenuation is more sensitive to the variation of the particle size within high porosity range.

2.6.2 P-wave velocity measurements

Based on the research about frequency-dependent velocity dispersion presented by Sams et al.(1997), the seismic velocity increase as the frequency increase resulting from the presence of fluid. The Gassmann's equation also supports this result. Meanwhile, it is presented by Clark et al. (1980) that seismic dispersion by frequency in intact dry rock is relatively negligible. However, seismic velocities depend not only on the rock and fluid properties but also on the ratio of seismic wavelength to the diameter of the scattering heterogeneity (Cerveny, 2005). In the compressed porous media, the porosity could strongly effect the wave propagating of different frequencies, the velocity is also affected and dispersed under different frequencies (wavelength).

2.6.2.1. Effect of frequency on the P-wave velocity

In order to analyze the velocity dispersion of the compressed porous rock caused by frequency, we used six different incident frequencies to measure the porous samples.

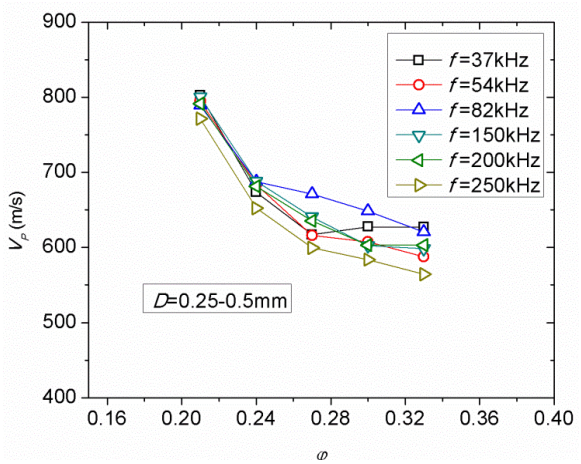

(a)

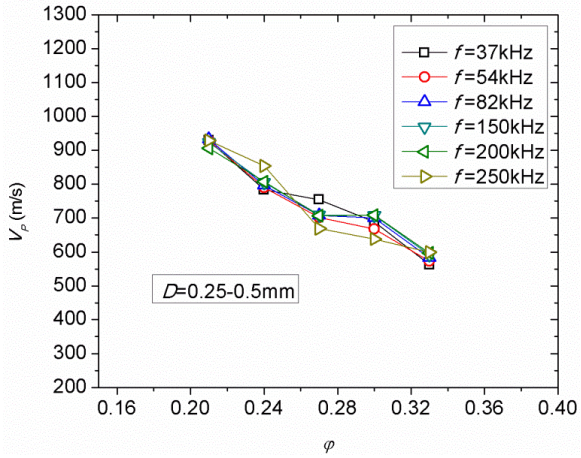

(b)

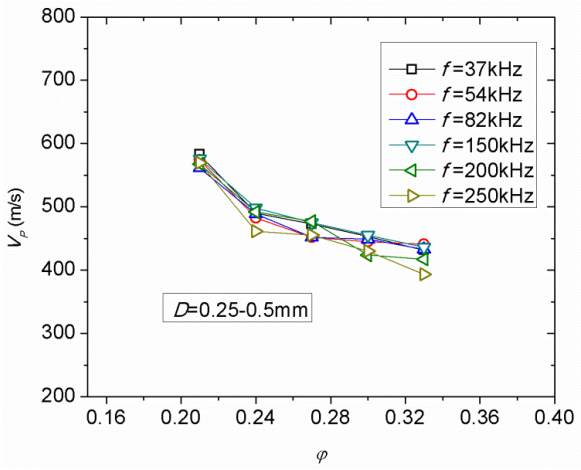

(c)

Figure 2-17. P-wave velocity against porosity for different frequencies. (a) sandstone, (b) limestone and (c) bituminous coal

Figure 2-17 shows the P-wave velocity against porosity for the cases of different incident frequencies. It can be seen that at high porosity, the velocity exhibited dispersive under different frequencies. For example, for the case of 250 kHz corresponding to around 2mm wavelength, the ratio of wavelength and particle size is approximately 6.5, the dispersion is obvious.

With the porosity reduced, the void between the particles get smaller, the velocity dispersion turned to be negligible. This means when the ratio of wavelength and particle size is large enough to a specific value at a certain porosity, the rock can be treated as equivalent medium. The velocity is therefore regarded to be a constant.

2.6.2.2 Effect of particle size on the P-wave velocity

Pyrak-Nolte et al. (1987) presented that there exists a time delay at the discontinuities resulting in the slowness of velocity. The particle size in a certain length corresponds to the number of contacts between particles affecting the velocity.

Figure 2-18 shows the effect of particle size on the velocity for three different types of rock samples. It is clear seen that the smaller particle size induces obvious decrease of velocity compared to the larger particle size at the same porosity. The number of discontinuity has a large effect on the velocity. Different from the velocity dispersion changing with porosity, the particle size effect is not much affected by the porosity. Despite the reduction of porosity, the discrepancy between different particle size and velocity has the similar values.

Meanwhile, the velocity of bituminous coal is smaller than sandstone and limestone at the same particle size and porosity. This illustrates that the stiffness (compliance) of the contacts between particles also has a influence on the P-wave velocity. The weaker stiffness of contact surface results in a larger time delay which leads to reduction of the phase velocity.

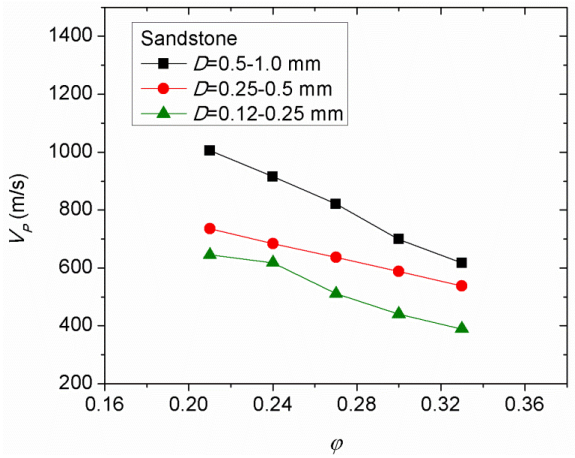

(a)

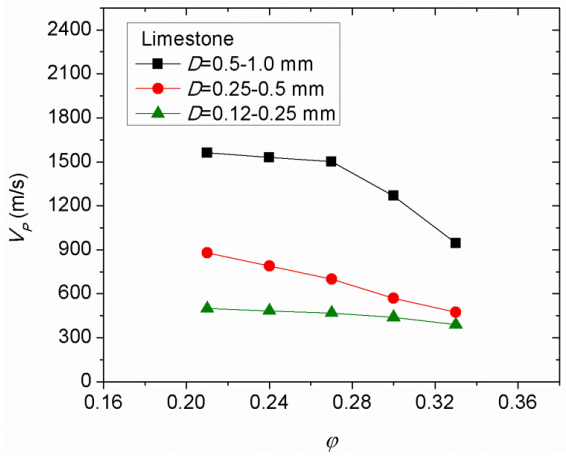

(b)

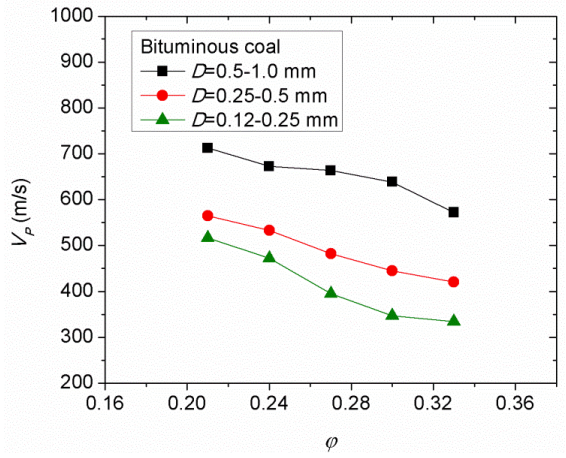

(c)

Figure 2-18. P-wave velocity against porosity for different particle size. (a) sandstone, (b) limestone and (c) bituminous coal

2.7 Permeability measurement of the compressed porous samples

After the seismic measurement of compressed porous samples, a bottom cover was assembled to the PVC pipe in case of the broken sample. Permeability of these samples were measured by steady-state method using the apparatus shown in Figure 2-13 (Right). It is known that for the compressed porous material, the Reynolds number *Re* is estimated by (Kong, 1999)

$$Re = \frac{\rho_f \upsilon D}{\varphi \mu} \tag{2-4}$$

where ρ_f (kg/m^3)is density of fluid media, υ (m/s) is apparent flow velocity and μ (Pa s) is fluid viscosity.

In present measurements, υ fell in the range of 4.24×10^{-4}-8.15×10^{-4} m/s, thus, the range of *Re* is 0.017-0.135 which falls into the applicable range of Darcy's law. Thus, the permeabilities of the samples were estimated by

$$k = \frac{1}{9.87 \times 10^{14}} \cdot \frac{2QP_r\mu L_s}{S\Delta P^2} \tag{2-5}$$

where k (md) is permeability; Q (m^3/s) is volumetric rate of flow at reference pressure; P_r (Pa) is reference pressure; ΔP (Pa) is the pressure difference between up stream (Pa) and down stream (Pa).

In permeability measurement, the nitrogen gas was used rather than fluid to measure the permeability of the compressed porous samples. Thus, gas slippage effect (Klinkenberg effect) should be taken into account. Equation 2-6 demonstrates the relationship between absolute permeability (k) and gas permeability

$$\frac{k}{k_g} = \frac{1}{1 + \frac{b}{p_m}} \tag{2-6}$$

where k_g (md) is the permeability of gas; p_m (atm) is the mean absolute pressure; b (atm) is a constant for a particular gas in a given rock type.

The value of b can be acquired from the measurement. Heid (1950) measured permeabilities of 164 sandstone samples ranging from 10^{-4} to 10 md by using nitrogen, and proposed an empirical equation (Equation 2-7) for the higher permeability estimation by plotting the logarithm of *b* factor against the logarithm of Klinkenberg (*k*) permeability. Sasaki (1987) measured compressed and lump coal samples to obtain the values of *b*, the results were highly consistent with the equation presented by Heid. We therefore substituted Equation 2-7 into Equation 2-6 and converted measured gas permeability to absolute permeability by using Newton-Raphson method.

$$b(\text{atm}) = 0.77[k(\text{md})]^{-0.39} \tag{2-7}$$

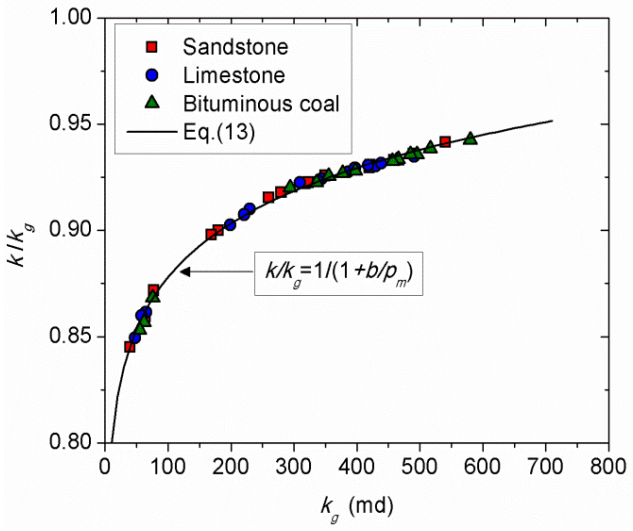

Figure 2-19. Correction of gas permeabilty.

Figure 2-19 showed absolute permeability (*k*) and gas permeability (k_g) relationship for compressed rock samples. The different rock exhibited the similar variation trend, which was *k/kg* decreased with the reduction of measured permeability (*kg*). The biggest correction was around 16% at the smallest porosity of 0.21.

Figure 2-20 shows the corrected permeabilities of the rock and coal samples in the experiment and compared them to the permeability of natural rock in the field (Kukal and Simons, 1986). The small scale compressed porous samples measured in laboratory showed the similar permeability of the large scale natural rock at the same porosity indicates that the compressed rock samples exhibited a relatively high permeability. The corrected permeability (k) were used in the following analysis.

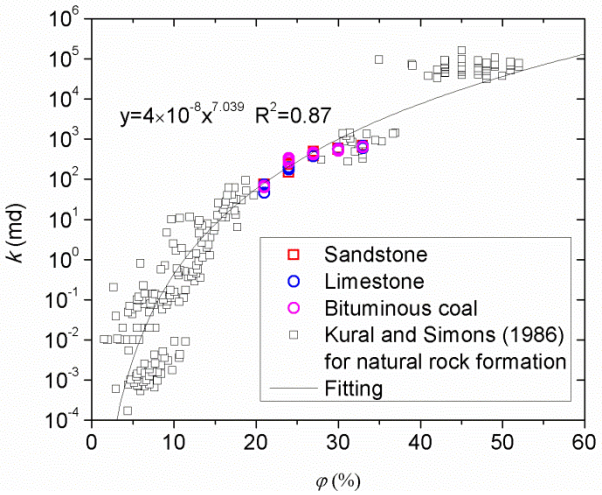

Figure 2-20. Corrected permeability by Klinkenberg effect vs. porosity.

Figure 2-21 shows permeability results plotteed against porosity for different rock types including sandstone, limestone and bituminous coal comprised of different particle sizes of rock or coal. The permeablity showed a systematic decrease with the reduction of porosity (Figure 2-21) on the samples. Throughout the results shown above, the size of particle and porosity are the major properties for the permeability of the compressed porous samples. The permeability is approximately varied from 40 to 600 md over the porosity from 0.21 to 0.33. The bituminous coal samples exhibite less permeabilities compared to sandsonte and limestone samples. This attibuted to the relative weaker stiffness of the contact surface between the particles. The smaller particles show smaller permeabilties as expected by *K-C* equation, especially at higher porosity. The discrepency between different particle size was especially noticeble in sandstone cases. The reduction of permeabilty of 0.5-1.0 mm particles was about 20% larger than that of 0.12-0.25 mm. Meanwhile, permeability at porosity φ=0.21 appeared sharp reduction in three rock types.

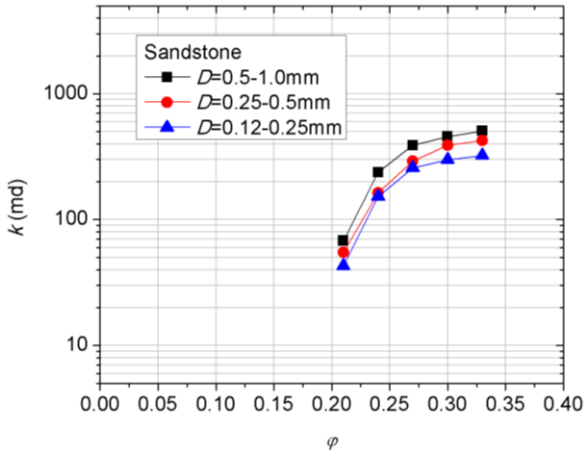

(a)

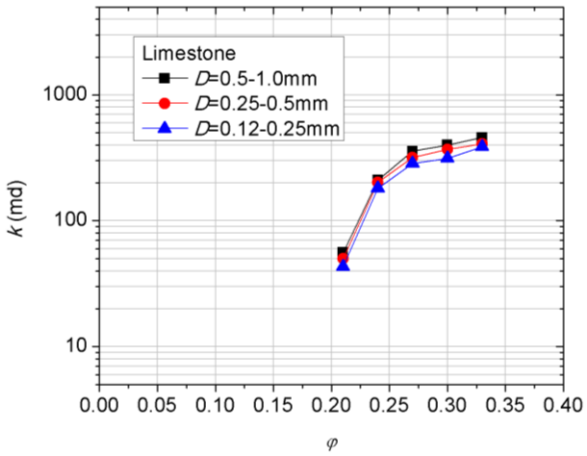

(b)

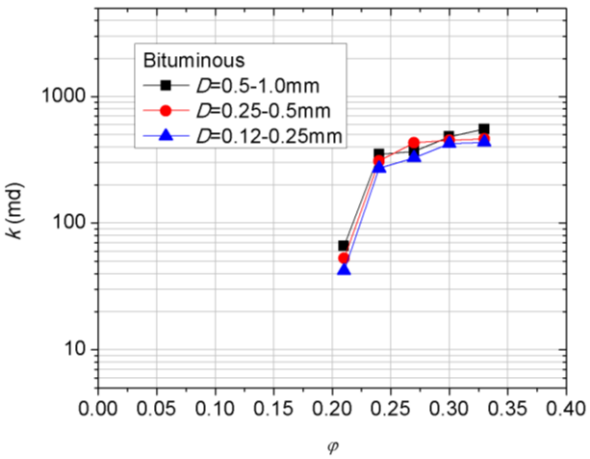

(c)

Figure 2-21. Permeability vs. porosity for different particle sizes. (a) sandstone, (b) limestone and (c) bituminous coal

Overall, the permeability of compressed samples comprising different types of rock particles shows a similar exponent relationship against porosity. Furthermore, along with the decrease of porosity, permeability of the different particle size tends to be close. It illustrates that the size of partilces are gradually close under the high pressure applied on the samples.

2.8 Conclusions

In this chapter, the apparatus and procedures of the laboratory experiments involving the mechanical, seismic and permeability measurement were elaborated. The preparation of the cylindrical compressed porous samples including sandstone, limestone and bituminous coal were introduced.

Smaller particle samples exhibited larger seismic attenuation regardless of the types of rock. As expected, the seismic attenuation becomes large with the increase of frequency. As the decrease of porosity, the effect of frequency on the attenuation is gradually declining down. Additionally, the velocity dispersion occurred when the ratio of wavelength and particle size close to 6.5 at the porosity φ=0.33. The dispersion tends to be eliminated with the reduction of porosity. This illustrated the ratio of wavelength and particle size as well as the porosity has a strong effect on the velocity dispersion in the porous samples

Seismic attenuation of sandstone and limestone showed smaller than that of bituminous coal for the same particle size and porosity. This means the stiffness of the discontinuities has an effect on the seismic propagation.

Permeability of the porous sample is strongly dependent on the particle size and porosity. The range of permeability of the compressed samples is from 40 to 600 md over the porosity φ=0.21 to 0.33.

Chapter 3: Model of seismic attenuation of the wave propagating through compressed porous rock

3.1 Introduction

When seismic wave propagates through the contact surface between two rock masses, the phenomenon is represented as a displacement discontinuity on the boundary between two elastic half-spaces. According to the displacement discontinuity theory, the stress across the contact surface is continuous. Whereas the contact surface is in an imperfect condition, an additional displacements occur between the boundaries of two half-spaces. The magnitude of the discontinuity in displacement is inversely proportional to the specific stiffness of the contact surface.

Pyrak-Nolte (1990) modeled the transmission and reflection coefficient based on the discontinuity displacement theory.

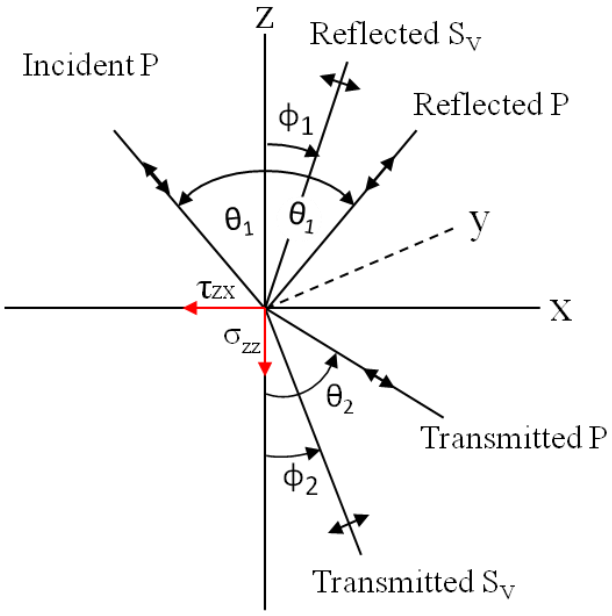

Figure 3-1. Transmission and reflection of an incident wave at a contact surface between two elastic half-spaces.

Transmitted and reflected components of P-wave on a displacement discontinuity are expressed as

$$u_{z1} - u_{z2} = \sigma_{zz/}\kappa_z \qquad \sigma_{zz1=}\sigma_{zz1} \tag{3-1}$$

$$u_{x1} - u_{x2} = \tau_{zx/}\kappa_x \qquad \tau_{zx1=}\tau_{zx2} \tag{3-2}$$

$$\sigma_{zz=}\lambda'\left(\frac{\partial u_x}{\partial x}\right) + (\lambda' + 2\nu)\left(\frac{\partial u_z}{\partial z}\right) \tag{3-3}$$

$$\tau_{zx} = \nu\left(\frac{\partial u_z}{\partial x} + \frac{\partial u_x}{\partial z}\right) \tag{3-4}$$

where u [m] is the displacement; σ [MPa] is the normal stress; τ [MPa] is the shear stress; κ [Pa/m] is the specific stiffness of the displacement discontinuity; λ' [-] and ν [-] are Lame's constants; subscripts1and 2 refer to the media above and below the displacement discontinuity.

For P-wave incident normally to (θ_1=90^o) the contact surface with the same material properties in both half-spaces, the reflection and transmission coefficients $R_P(\omega)$ and $T_P(\omega)$ are

$$|R_P(\omega)| = \frac{\omega}{\sqrt{\omega^2 + 4\left(\frac{\kappa_z}{Z_P}\right)^2}} \tag{3-5}$$

$$|T_P(\omega)| = \frac{2\kappa_z/Z_p}{\sqrt{\omega^2 + 4\left(\frac{\kappa_z}{Z_P}\right)^2}} \tag{3-6}$$

$$|T_P(\omega)|^2 + |R_P(\omega)|^2 = 1 \tag{3-7}$$

As a result, the velocity across a contact surface can be estimated by the group delay at the discontinuity. For the transmitted wave, the group time delay has been presented by Pyrak-Nolte (1987).

$$t_g(\omega) = 2(\kappa_z/Z_P)/4(\kappa_z/Z_P)^4 + \omega^2 \tag{3-8}$$

For a rock with an arbitrary number of partitions (*M*), Gibson & Ben-Menahem (1991) posed the expression for the seismic velocity obtained by considering the changes of amplitude and phase due to successive passages of the wave through individual partitions can be written as

$$V = \frac{V_G}{1 + V_G \sum_{i=1}^{M} D_i t_{gi}(\omega)} \tag{3-9}$$

where V [m/s] is the velocity of the fractured rock, D_i [-] is the frequency of contact surface in the i_{th} fracture set in the direction of propagation of the wave and t_{gi} (ω) [s] is the time delay at a discontinuity belonging to the *ith* set.

In a similar manner, the expression for the attenuation or absorption coefficient β of a system consisting of partitions can be expressed as

$$\beta = \beta_0 + \sum_{i=1}^{M} D_i(-ln|T_{Pi}|) \tag{3-10}$$

Here, T_{Pi} is the transmission coefficient of the wave across the ith contact surface set for the case of an incident *P* wave; and β [1/m] is the attenuation coefficient for the intact rock.

Stiffness of the discontinuity was derived from the apparent modulus such as the P-wave and S-wave velocity, density of discontinuities as well as the contact area, et.al. Hudson presented a normal and tangential stiffness of the contact surface,

$$Z_N = r' \frac{4G}{\pi r}\left(1 - {V_S}^2/{V_P}^2\right)\left(1 + \frac{2(r^\omega)^{1/2}}{\sqrt{\pi}}\right) \tag{3-11}$$

$$Z_T = r' \frac{8G}{\pi r}\left(1 - \frac{{V_S}^2/{V_P}^2}{3 - 2{V_S}^2/{V_P}^2}\right)\left(1 + \frac{2(r^\omega)^{1/2}}{\sqrt{\pi}}\right) \tag{3-12}$$

where V_p [m/s] and V_s [m/s] are P and S-wave velocity, G [MPa] is shear modulus, r' [-] is the proportion of the fracture surface area that consists of welded contact, r [m] is the mean radius of the contact areas.

3.2 Establish of seismic attenuation model through porous media

Seismic attenuation of amplitudes, β (1/m), is defined as

$$\beta = -\frac{1}{L_s} ln \left[\frac{A_1(f)}{A_0(f)}\right] \tag{3-13}$$

where f [Hz] is the frequency; A_0 (f) is the spectral amplitude of the incident wave; $A_1(f)$ is the spectral amplitude of the transmitted wave; and L_S [m] is the propagation length.

Mechanism of seismic attenuation is subject to physical phenomena including the frictional and inelastic attenuation(Biot, 1956; Dvorkin et al., 1995; Müller et al., 2010). In the goaf, seismic attenuation and velocity reduction are induced by large void resulting from fragmented rocks and coals. The majority of the attenuation are caused at the discontinuities between the rock or coal masses. The total attenuation includes the scattering attenuation and intrinsic attenuation which is much smaller than the former one. The value of the attenuation is mainly decided by the stiffness at the discontinuities and the number of the contact points, since the goaf is not fully consolidated including large void. The attenuation in pore space filling gas is relatively larger pertaining to its smaller drainage ability.

In this study, we assumed a mechanical model to provide an equation on estimating seismic attenuation in the goaf area based on the laboratory measurements.

Gibson and Ben-Menahem (1991) and Boadu and Long (1996) presented an elastic wave scattering model for the seismic attenuation passing through a system of aligned fractures. A wave propagating in a porous media is much more complex due to the many contact surfaces between the rock fragments/particles and the network of propagation passes. We developed a revised model based on Boadu and Long's model considering the stiffness of the rock media and the number of the contact surfaces.

(a)

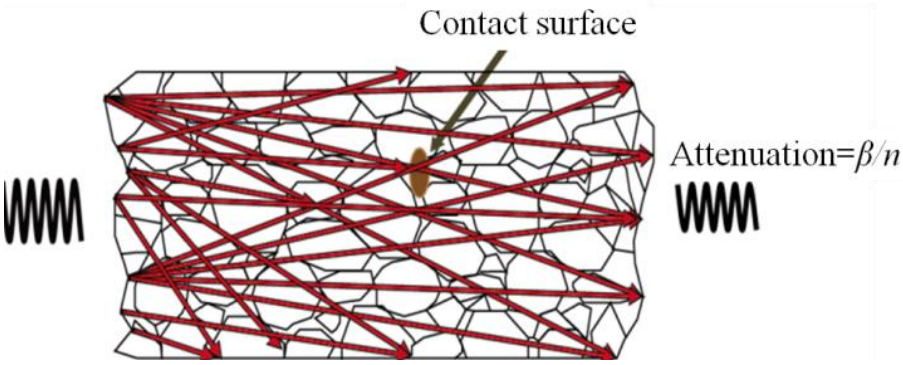

(b)

Figure 3-2. Seismic wave attenuation propagating through the contact surfaces in the fragmented rock. (a) A model of spherical rock masses arranged in series on a straight line. (b) Effect of network propagation through porous rock masses in statistically random arrangements.

To model the attenuation at the contact surfaces between the particles/fragments, we first assumed a series of spherical rock particles arranged in a straight line as shown in Figure 3-2 (a) and constructed the equation for seismic attenuation at the contact surfaces between the particles under compressive stress:

$$\beta^* = \beta_0 + M(-ln|T|)$$

$$M = \frac{1(m)}{D(m)}; \quad T = \frac{2\kappa/I}{-i\omega + 2\kappa/I} \tag{3-14}$$

where β^* [1/m] is the seismic attenuation through the straightly aligned particles; β_0 [1/m] is the coefficient of attenuation of the intact rock; D [m] is diameter of particles; M [-] is the ideal number of contact points between the particles in a unit length (= 1 m);

T [-] is the transmission coefficient at the contact surface; I [kg/m^{2}s] is the wave impedance; and κ [Pa/m] is the stiffness of the contact surface.

Next, we simulated seismic waves reflected and refracted at irregular contact surfaces among irregularly shaped particles as shown in Figure 3-2 (b). In this case the wave amplitude is amplified at the contact surface as a result of the superposition of the reflected waves produced by the seismic network.

Therefore, the attenuation through the porous media is considerably reduced compared with the straight line case due to the networking waves producing the duplication effect. In the second model, the seismic attenuation was reduced by simulating the effects of network propagation in the porous media using the duplication factor, n, in Equation 3-15 as follows;

$$\beta = \beta_0 + \frac{M}{n}(-\ln|T|) \tag{3-15}$$

where β [1/m] is the total seismic attenuation through the porous media consisting of particles.

The rock masses or particles in the model were spherical, with the shape of the contact surface between the particles being circular as shown in Figure 3-3. The ratio of the contact surface diameter to the diameter of the spheres is r_a (Equation 3-16) and can be obtained from the Hertz contact theory presented by Johnson (1987).

$$r_a = \frac{d}{D} = \sqrt[3]{\frac{3\pi(1-\nu)}{2C(1-\varphi)G}\sigma} \tag{3-16}$$

where d [m] is diameter of contact on the circular area; φ is porosity, ν is Poisson's ratio; G [Pa] is shear modulus of particle material; σ [Pa] is the compression stress; and C is coordination number.

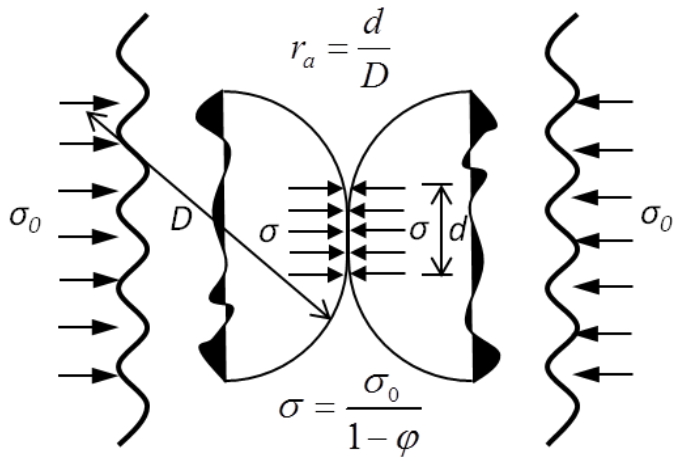

Figure 3-3. Hertz theory for the contact surface between particles.

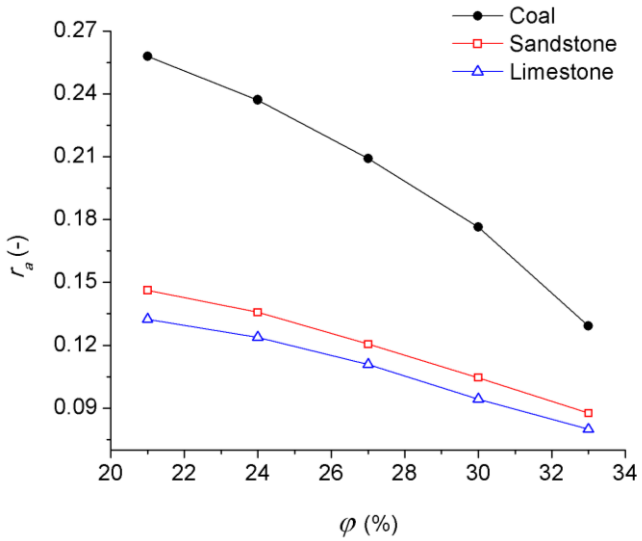

Figure 3-4. Relationship between porosity and r_a.

Murphy (1982) presented the empirical equation for the coordination number based on measurements using granular sedimentary rocks as follows:

$$C = 24\exp(-2.55\varphi) - 0.37 \tag{3-17}$$

Therefore, r_a can be derived as

$$r_a(\sigma, \varphi) = \frac{d}{D} = \sqrt[3]{\frac{\pi(1-\nu)}{16G}\frac{\exp(2.55\varphi)}{1-\varphi}\sigma} \tag{3-18}$$

The transmission coefficient T at the contact surface can then be found considering the welded surface (Hudson, 1981) and the Hertz contact theory (Equation 3-16) with respect to the frequency and porosity:

$$|T(f,\varphi,\sigma)| = \left|\frac{\kappa(\varphi,\sigma)/I}{-i\pi f + \kappa(\varphi,\sigma)/I}\right| \tag{3-19}$$

$$\kappa(\varphi,\sigma)/I = \frac{8G}{\pi D\rho V_{PI}}\left(1 - \frac{{V_{SI}}^2}{{V_{PI}}^2}\right)\cdot\left(1 + 2\sqrt{\frac{r_a(\sigma,\varphi)}{\pi}}\right) \tag{3-20}$$

where V_{PI} [m/s] and V_{SI} [m/s] are the P and S-wave velocities of the intact rock, respectively.

Since

$$V_{PI} = \sqrt{\frac{K + 4/3G}{\rho}};\quad V_{SI} = \sqrt{\frac{G}{\rho}}\ ;\quad \frac{{V_{SI}}^2}{{V_{PI}}^2} = \frac{G}{K + 4/3G} = \frac{1-\upsilon}{2(1-2\upsilon)} \tag{3-21}$$

Equation 3-20 can be expressed as

$$\kappa(\varphi,\sigma)/I = \frac{8G}{\pi D\rho V_{PI}}\left(\frac{1-3\upsilon}{2(1-2\upsilon)}\right)\cdot\left(1 + 2\sqrt{\frac{r_a(\sigma,\varphi)}{\pi}}\right) \tag{3-22}$$

By substituting Equation 3-20 into Equation 3-16, the model (denoted the B-R model) revised from Boadu's model was formulated, expressing the attenuation of a seismic wave propagating through the spherical particles as. Thus, the B-R model presented here is a function of the particle size D and mechanical properties φ, ρ, ν, G, and V_{pI}, as well as the wave frequency f and duplication factor n. In this model, n cannot be chosen arbitrary. Therefore, an empirical value was given based on laboratory measurements of the investigated porous samples, as described below.

As described above, the duplication factor n was estimated based on laboratory tests. Here, n is acquired by comparing the difference between the measured attenuation and the model estimates of different n values (Figure 3-5). The method of mean squared

error (*MSE*) was used to minimize the error between the model and experimental results (Equation 3-23).

$$MSE(n) = \frac{1}{N}\sum_{j=1}^{N}\left(\frac{\beta_{m_{nj}} - \beta_{l_j}}{\beta_{l_j}}\right) \tag{3-23}$$

where β_{mnj} [1/m] is the attenuation of the *j*th sample in the B-R model using a particular *n*; β_{lj} [1/m] is the measured attenuation of the *j*th sample; and *N* is the number of samples.

Figure 3-5 shows the *MSE* between the B-R model and the measurement results vs. *n* for the compressed porous samples for *D* = 0.5–1.0 mm and φ = 0.27. The curves of the *MSE* for the coal, sandstone and limestone samples show minimum values at *n* = 150, 204 and 240, respectively; these points are defined as the optimum value points, n_{opt}.

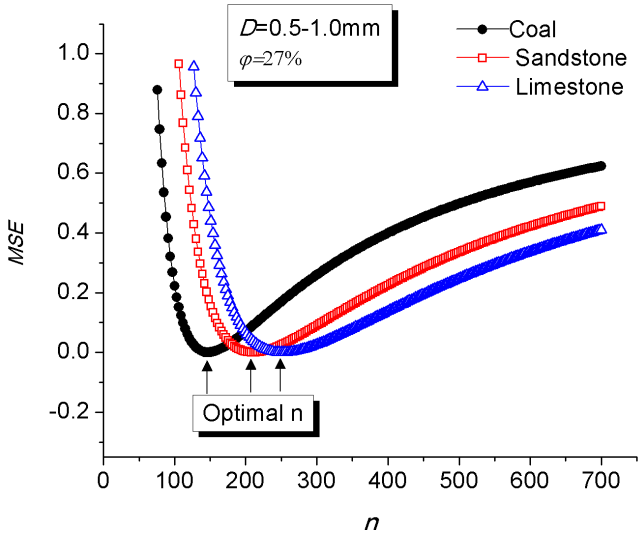

Figure 3-5. Mean squared error between the B-R model and measurement results vs. duplication factor, *n*, for compressed porous samples (φ = 0.27; *D* = 0.5–1.0 mm).

The results derived from the B-R model agree well with the measured results using n_{opt}. To investigate the characteristics of n_{opt}, we plotted the values of n_{opt} against the velocity (V_{PG}) of all the compressed porous samples (Figure 3-6).

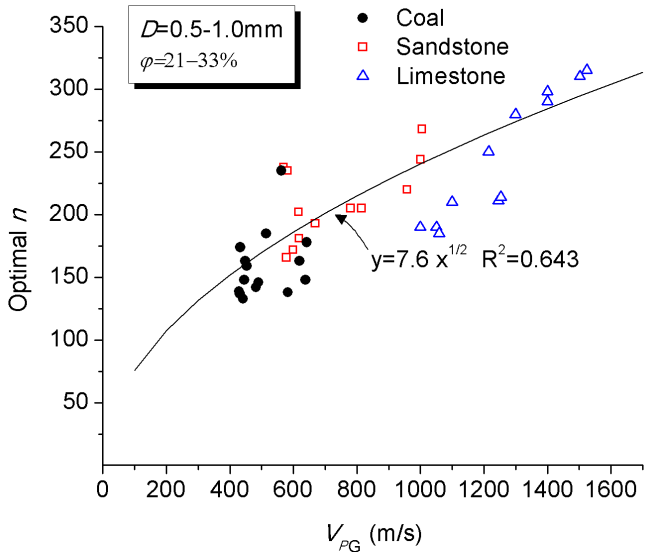

Figure 3-6. Correlation between optimal n and V_{PG} (φ = 0.27–0.33; D = 0.5–1.0 mm).

As V_{PG} increases, n_{opt} rises because the wave attenuation through the harder samples such as limestone is lower than through the soft samples such as coal. Since n_{opt} is within a specific range for a particular rock, we can utilize the B-R model using n_{opt} as n in Equation 3-25 .

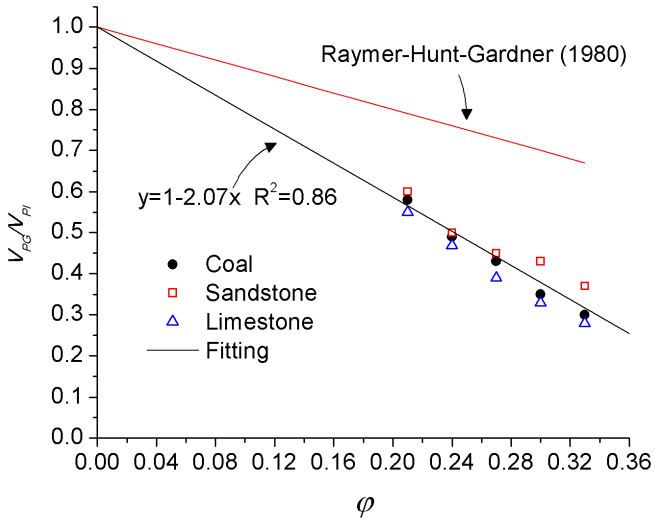

Figure 3-7. Velocity ratio of intact samples and compressed porous samples vs. porosity.

To estimate the value of n_{opt}, we used the empirical correlation between n_{opt} and the measured P-wave velocity V_{PG} (Figure 3-6). The correlation was found to be

$$n_{\text{opt}} = 7.6\sqrt{V_{PG}} \tag{3-24}$$

Figure 3-7 shows the measured V_{PG}/V_{PI} vs. porosity along with the V_{PG}/V_{PI} vs. φ line from the equation of (Raymer et al., 1980) expressed as

Raymer-Hunt-Gardner equation; $\frac{V_{PG}}{V_{PI}} = 1 - 1.5\varphi$ (3-25)

The velocity of the compressed porous sample accounts for approximately 25% to 52 % of that for the intact sample for φ = 21%–33%. The present measurement results, which differ from those based on Equation 3-24, yield the following empirical equation:

Present equation; $\frac{V_{PG}}{V_{PI}} = 1 - 2.07\varphi$ (3-26)

Combine Equation 3-26 with Equation 3-25,

$$n_{\text{opt}} = 7.6\sqrt{(1 - 2.07\varphi)V_{PI}} \tag{3-27}$$

Finally, the B-R model can be expressed by the following equation:

$$\beta(D, \varphi, f, V_{PI}) = \beta_0 + \frac{5}{38D\sqrt{(1 - 2.07\varphi)V_{PI}}} \cdot \ln\left(1 + 2\frac{\pi^2 f^2}{(\kappa(\varphi, \sigma)/I)^2}\right) \tag{3-28}$$

3.3 Effect of λ/D on seismic attenuation

In the method described above, it is assumed that the model can be matched with the measurements while n is provided in the B-R model. Because the model estimation may be dependent on the particle size and frequency, therefore, in this section, using λ/D, we examined the influence of the combination of particle size and frequency on the seismic attenuation. In the field measurements of the goaf areas, the frequency of

seismic signals used were quite low, for instance, 20–150 Hz. This indicates that the rocks including the compressed porous rocks were treated as an equivalent elastic medium (Barton, 2007). However, a major problem with this approach is the accuracy of the porosity values. Therefore, to account for the porosity of the porous rock layers we use the ratio λ/D. To compare the errors between the B-R model and the measured values we define the dimensionless difference error ζ:

$$\zeta = \frac{\beta_{(M)} - \beta_{(L)}}{\beta_{(L)}} \tag{3-29}$$

where $\beta_{(M)}$ [1/m] is the attenuation predicted by the B-R model and $\beta_{(L)}$ [1/m] is the measured attenuation.

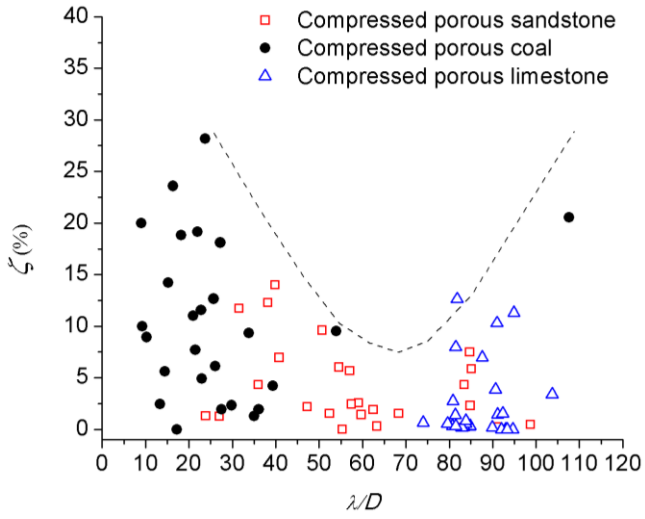

Figure 3-8. Difference error ζ (%) between the measured data and the B-R model prediction vs. λ/D.

The scattering of the attenuation (Figure 3-8) is obvious at different λ/D. The difference between the experimental values and those predicted by the model is also affected by the λ/D of the rock types commonly found inside goafs: sandstone, limestone and bituminous coal. The coal samples show larger attenuation compared with the sandstone samples, suggesting discrepancies between the lithological character of the

rock types, or smaller cohesion of the coal particles compared with that of sandstone and limestone particles; this is attributed to the volatile organic compound on the surface of the particles. Furthermore, the differences between the model and the experimental results increase as λ/D decreased. These differences are less than 10%, with low values around λ/D = 65–80, indicating that the model which includes porosity agrees well with the laboratory measurements, with the difference becoming small when λ/D = 65–80. Thus, wave attenuation is dependent on the size of the mass/particle and the frequency of the seismic wave.

The above results support the initial thought that λ/D is an important parameter when comparing laboratory and field measurements. The seismic characteristics used for the goaf measurements can be evaluated from the laboratory data measured for a similar range of the λ/D covering the actual goaf (Table 2-3).

3.4 Comparison of the B-R model and laboratory measurements for different particle sizes and frequencies

The attenuation estimated by the B-R model was consistent with that derived from the measurements. The attenuation increased with porosity, and the coal sample showed a larger attenuation than the sandstone and limestone ones.

Moreover, we observed that the porous sample with smaller D showed larger attenuation than the sample with larger D and the same porosity. Since the porosity is independent of the particle size, this can be attributed to the fact that the number of contact points between particles in a unit volume increases with decreasing particle size. This is illustrated in Figure 3-9, which indicates that the samples comprising smaller-sized particles have a larger number of contact points for the transmitted wave as well as smaller stiffness and strength compared with those with larger particle size. The attenuation estimated by the B-R model agrees well with the measurement data, especially for the samples with larger D.

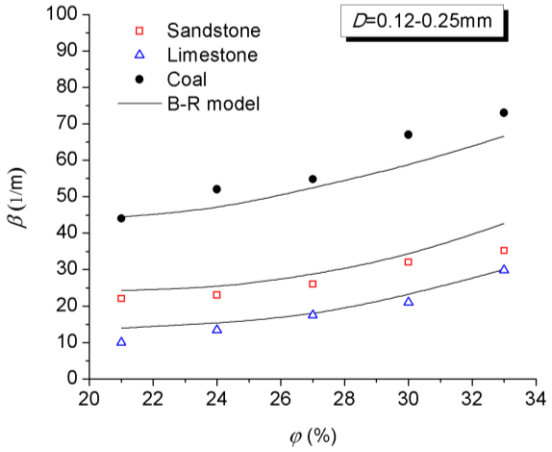

(a)

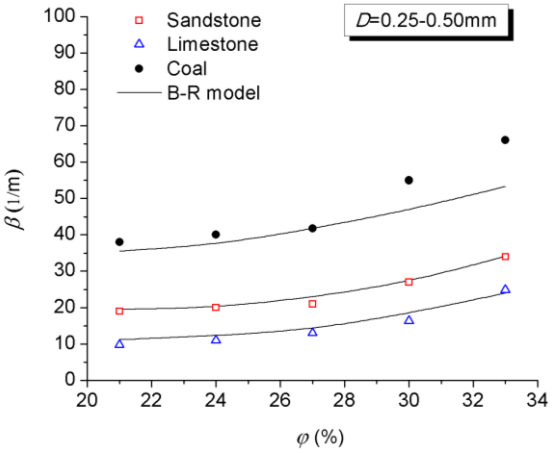

(b)

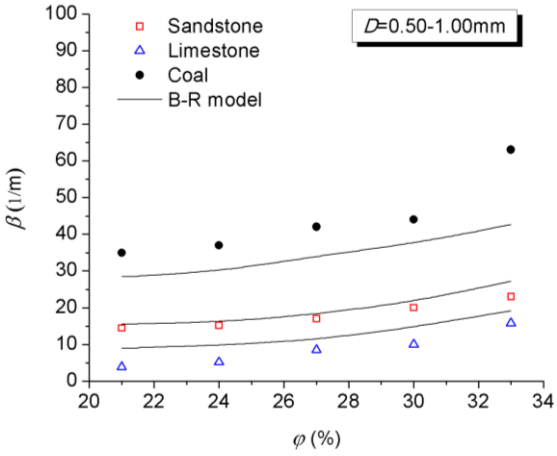

(c)

Figure 3-9. Attenuation vs. porosity for different particle sizes. (a) D = 0.12–0.25 mm, (b) D = 0.25–0.50 mm and (c) D = 0.50–1.00 mm

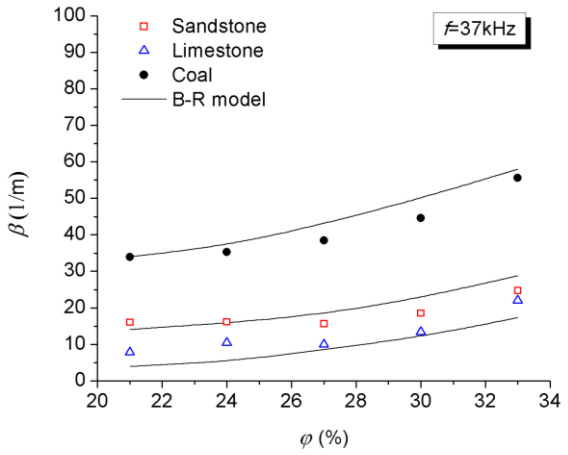

(a)

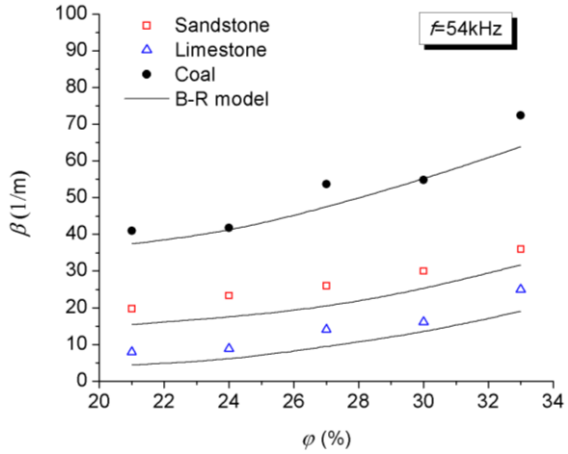

(b)

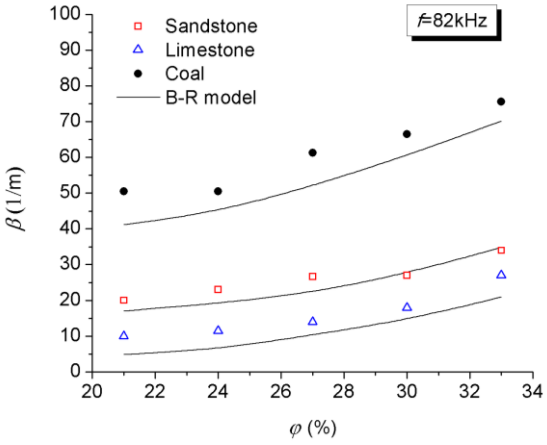

(c)

Figure 3-10. Attenuation vs. porosity for different frequencies. (a) 37 kHz, (b) 54 kHz and (c) 82 kHz

We also compare the laboratory measurements and estimation by the B-R model under different frequencies (Figure 3-10). As shown in Figure 3-10, the attenuation increases with the frequency, and the differences between the measurement and the B-R model increase at higher frequencies. This illustrates that the frequency has a considerable influence on the applicability of the B-R mode regarding seismic attenuation. The measurement at the lower frequency (37 kHz) is in better agreement with the model prediction.

3.5 Correlation between P-wave velocity and porosity

Li and Gu (2002) found an empirical correlation between P-wave velocity and seismic attenuation based on statistical analysis of field measurement data as follows:

$$\lambda\beta = 0.893 \times 10^{6} {V_{PI}}^{-2.2} \tag{3-31}$$

In this study, to formulate a similar relationship for the porous media, we plotted attenuation against the velocity ratio (V_{PG}/V_{PI}) of the compressed porous rock and coal samples and their intact samples (Figure 3-11). The attenuation in the porous samples was higher than in the intact samples due to the reduced porosity. For the intact samples, the measured data were roughly 4 times larger than that calculated from Equation 3-31 presented by Li and Gu. The empirical relation between the measured seismic attenuation and the velocity ratio V_{PG}/V_{PI} through the porous samples can be expressed by following empirical equation,

$$\lambda\beta = 0.011 \times \left(\frac{V_{PG}}{V_{PI}}\right)^{-2} \tag{3-32}$$

Thus, the seismic attenuation can also be estimated from the measured elastic velocity ratio. This indicates that we may be able to estimate seismic attenuation through porous media, such as a coal-mine goaf, from the velocity change against that of the

intact rock layer. Furthermore, the porosity can also be estimated from the following Equation 3-33 by revising Equation 3-27.

$$\varphi = \left(1 - \frac{V_{PG}}{V_{PI}}\right) / 2.07 \tag{3-33}$$

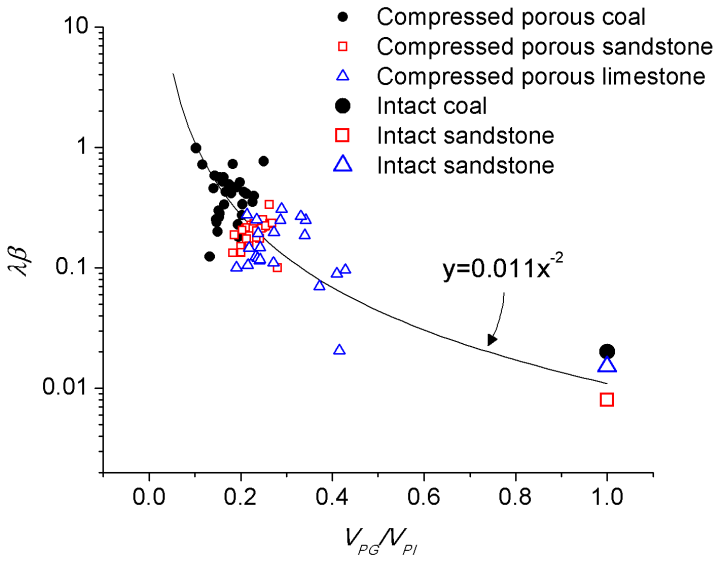

Figure 3-11. Comparison of seismic attenuation in a wavelength vs. P-wave velocity ratio for the experimental measurements.

3.6 Conclusions

In this chapter, seismic attenuation through porous rock and coal media was investigated to form an equation for attenuation that accounts for the porosity, wave frequency and particle/mass size. The new equation for seismic attenuation (named the B-R model) was developed by considering the effects of increased attenuation due to larger numbers of contact surface between the particles and decreased attenuation due to network propagation through the porous media. Those effects were modeled by introducing the ideal contact number and the duplication factor which were evaluated by comparison with laboratory measurements using compressed porous samples of rock and coal particles. The main results are summarized as follows.

1. The seismic attenuation through the compressed porous samples was measured; the results clearly showed that attenuation in the samples consisting of smaller particles was greater than that in samples with larger particles at the same porosity and wave frequency.

2. The seismic attenuation through compressed coal particles was higher than that through sandstone or limestone particles with higher elastic velocities.

3. We developed the B-R model based on the model presented by Boadu and Long for a multi-fractured medium to estimate the effect of the particle diameter and porosity of the porous media and the wavelength on the seismic attenuation.

4. The seismic attenuation and P-wave velocity changes estimated by the B-R model showed good agreement with the laboratory measurement data of the compressed porous samples.

5. Our results show that it is possible to estimate seismic attenuation through porous rock or a coal layer, such as a coal mine goaf, from the velocity changes compared with those of the intact lock layer.

Chapter 4: Estimate of permeability of compressed porous rock by seismic velocity and attenuation

4.1 Introduction

To understand, predict, or manage hydrological systems, information about the basic property such as permeability is often required, as is information about the controlling characteristics, such as the lithology, porosity, or geometric skeleton (Cushman and Tartakovsky, 2016). With the knowledge that both permeability and seismic properties such as velocity and attenuation are related to volumetric and geometric properties of rock. Therefore, it is important to relate them in some way. Raymer et al. (1980) and Dvorkin and Nur (2002) have presented the relationship between the P-wave velocity and porosity of the natural and unconsolidated sediments. Assefa et al., 1999, found that their bimodal porosity limestone specimens showed higher attenuation when permeability and porosity were also larger. Prasad (2003) used hydraulic units to relate the velocity and attenuation to permeability and find the velocity increased and attenuation decrease with the reduction of porosity. Besides, Pride (2005) discussed the correlation between the permeability and frequency-dependence P-wave attenuation in the double-porosity model. The slope $\partial Q^{-1}/\partial f$ of peak attenuation is inversely proportional to permeability.

However, no universal relation valid for all rock types can exist between permeability and seismic velocity or attenuation. The previous empirical correlations between permeability and seismic property is based on the case-by cased details how a rock is built. The different lithology or geometric formation results in a varied correlation between permeability and seismic velocity or attenuation.

In this study, the effect of fluid on the seismic is omitted, because it was mainly focused on the gas permeability in the goaf. Additionally, the size distribution is fixed similar

as the actual goaf. Therefore, the correlation between the gas permeability and seismic properties is concentrated on the goaf area.

As it is known that the relationship between permeability and seismic properties is usually difficult to establish. While, with the knowledge that compressed porous material like goaf is filled by random aligned fragments, which resulting in the seismic wave propagation in a sinuate path instead of a straight line (Cerveny, 2005) (Figure 4-1).

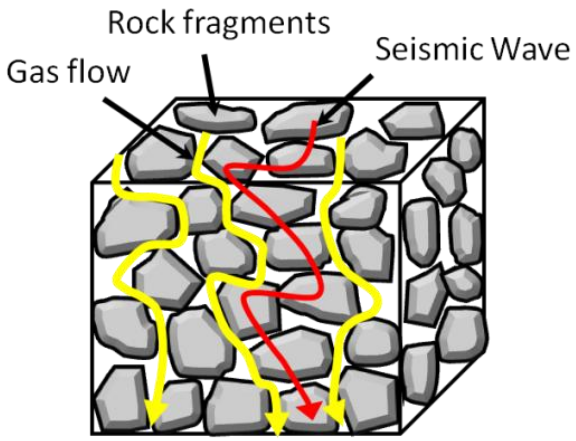

Figure 4-1. Schematic of seismic wave transmitting and gas flow cross the compressed porous material.

This indicated the wave propagation was affected by the geometric features such as tortuosity and porosity of the rock skeleton. Meanwhile, the permeability is also determined by the tortuosity factor and porosity as well as particle size. Therefore, in this chapter, it is attempted to relate seismic velocity to tortuosity factor, and seismic attenuation to the porosity.

4.2 Kozney-Carman equation

According to Poiseuille law, the mean fluid velocity along a tube is shown as

$$\overline{v} = -\left(\frac{\Delta P}{L_e}\right)\left(\frac{{D_H}^2}{16k_0\mu}\right) \tag{4-1}$$

where ΔP [Pa] is pressure drop; L_e [m] is the actual length of the fluid paths; S [-] is the specific surface area (the ratio of the total interstitial surface area of the voids and pores to the bulk volume); D_H [m] is hydraulic diameter; k_0 [-] is a shape factor; μ [N s/m^2] is dynamic viscosity.

The fluid seepage velocity(v_d) is given by Darcy law

$$v_d = -\left(\frac{k}{\mu}\right)\left(\frac{\Delta P}{L}\right) \tag{4-2}$$

where k [m^2] is permeability; L [m] is the geometrical length of the sample.

Based on the Forchheimer assumption, the correlation between v_d and $\overline{v}$ is

$$\overline{v} = \left(\frac{v_d}{\varphi}\right)\left(\frac{L_e}{L}\right) \tag{4-3}$$

Therefore, permeability can be expressed as

$$k = \varphi {D_H}^2/16k_0(L_e/L)^2 \tag{4-4}$$

Because hydraulic diameter is

$$D_H = 4\varphi/S_{sp}(1-\varphi) \tag{4-5}$$

Substitute hydraulic diameter Equation 4-5 into Equation 4-4. Permeability is

$$k = \frac{\varphi^3}{k_0(L_e/L)^2(1-\varphi)^2{S_{sp}}^2} \tag{4-6}$$

Based on the correlation between specific surface (S_{sp}) and particle diameter (D)

$$S_{sp} = 6/D \tag{4-7}$$

k is converted into Equation 4-8, which is called Kozney-Carman equation

$$k = \frac{D^2\varphi^3}{72\tau(1-\varphi)^2}; \quad \tau = (L_e/L)^2 \tag{4-8}$$

where τ is tortuosity.

Because *K-C* relationship show that the permeability is related to the square of the particle size, D^2; therefore, the distribution of D^2 was plotted (Figure 4-2). The peak value D_P^2 of the squared particle size values were found as D_P^2 = 0.04, 0.065 and 0.25 mm^2 for the three groups mentioned above, respectively.

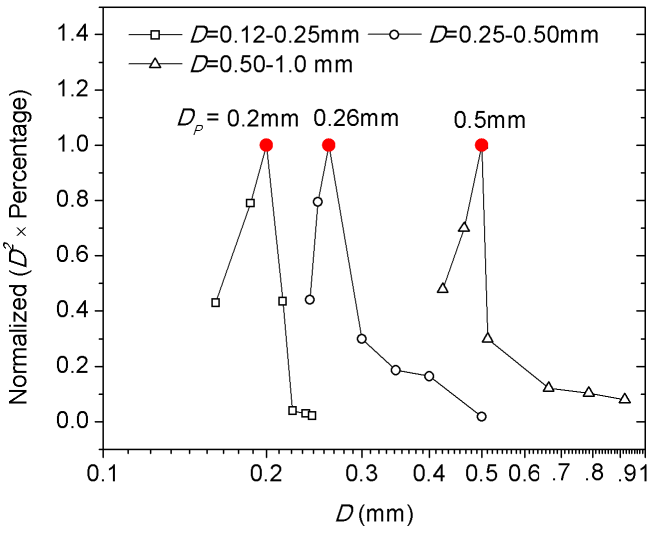

Figure 4-2. Size distribution of the sandstone particles in our laboratory measurements.

4.3 Correlation between permeability and seismic properties

The Kozney-Carman (*K-C*) equation is widely used in empirical predictions of the permeability of porous media. However, it was often reported that the permeability decreases much more rapidly with decreasing porosity. Thus, Bourbie et al. (1987) proposed a variable power formula for porosity:

$$k(\text{md}) = 9.87 \times 10^8 \cdot \frac{1}{72\tau}\varphi^n \cdot [D_P(\text{mm})]^2; \quad \tau = (Le/L)^2 \tag{4-9}$$

where k [md] is the permeability coefficient; n is power number ranges from the derived value of 3 for large porosities to values of 7–8 at very low porosities; $D_P{}^2$[mm^2] is the average square particle size; τ [-] is tortuosity; L_e [mm] is the average length of the fluid paths; L [mm] is the geometrical length of the porous media; 9.87×10^8 [md/mm^2] is the unit conversion factor.

Because this relationship is based on conductive hydraulic flow paths without considering the interaction of tortuous paths, Mavko and Nur (1997) presented a model that introduced the percolation threshold porosity in the *K-C* equation:

$$k(\text{md}) = 9.87\times10^8\frac{1}{72\tau}\cdot\frac{(\varphi-\varphi_c)^n}{(1-\varphi+\varphi_c)^2}[D_P(\text{mm})]^2 \tag{4-10}$$

where φ_c [-] is the percolation threshold porosity. The modified formula showed a satisfactory fit to their measured permeability in well-sorted material.

4.3.1 P-wave velocity and permeability

As shown in Figure 4-1, seismic waves propagate through a porous rock layer. Therefore, the apparent velocity is dependent on the length of the actual tortuous path of the seismic wave through the porous layer. For a specific condition, larger tortuosity corresponds to a longer wave propagation path and lower apparent velocity. In contrast, in intact rock, the propagation path is roughly on a straight line. Thus, the P-wave velocity variation coefficient η [-] can be defined as the ratio between the P-wave velocity of the porous and intact samples, V_{PI}/V_{PG}, reflecting the tortuous character of the compressed rock

$$\eta = \frac{V_{PI}}{V_{\text{PG}}} \tag{4-11}$$

At the same time, the tortuosity (τ) reveals the fluid flow in the compressed sample through the tortuous void space. The value of τ has been estimated by a number of

researchers (Table 4-1). Although the propagation routes of the seismic wave and fluid flow are completely different, because seismic wave propagate through the solid (particles) while gas flows through porous. However, both of them are effected by the tortuous character of the compressed porous rock. Therefore, we assumed the tortuosity factor in the *K-C* equation is a function of η:

$$\tau = f(\eta) \tag{4-12}$$

Table 4-1. Estimate of the tortuosity factor in the previous studies

Authors	Rock/Material	Tortuosity (τ)
Carman (1937)	Porous media	$1.8<\tau<2.04$
Davies and Dollimore (1970)	Sedimental spheres	$\tau=1/(5\times\varphi^{n-3}(1-\varphi))$
Koponen et al. (1997)	Random porous media	$2.6<\tau<4.16$
Bechtold and Ye (2003)	Fibres	$4.8<\tau<10$
Li and Gu (2005)	Granular beds	$5.124<\tau<2.04$
Chen and Papathanasiou (2006)	Disordered fibers	$4<\tau<7.2$
Nakayama et al. (2007)	Rods, cubes and cylinders	$3<\tau<3.8$
Gamrat et al (2008)	Square rods	$1.2<\tau<11.2$
Plessis and Woudberg (2008)	Blocks	$1.8<\tau<2.2$
Terual and Rizwan-uddin (2009)	Square cylinders	$\tau=3.27$, $\varphi< 0.55$
Pacella et. al. (2011)	Fibres bundle	$165\varphi<\tau<2.2$
Turkuler Ozgumus et al. (2014)	Rectangular rods	$1.28<\tau<8$

4.3.2 Seismic attenuation and permeability

Seismic attenuation is accompanied with energy loss caused by scattering from geo-structures and by absorption in intrinsic micro-mechanisms such as normal and shear micro-displacements across microcracks and discontinuities. These processes involve friction, fluid micromovement between pore spaces, and the existence of jointing and fractures (Barton, 2007).

Seismic attenuation is more sensitive to the characterization of rock and fluid properties more than seismic velocity, especially porosity (φ) and fracturing (Quan and Harris, 1997). This suggests that porosity is strongly related to seismic attenuation. Since seismic attenuation through porous media increases sharply with φ, the ratio between the seismic attenuation of porous and intact media, ξ , is defined as a function of φ as

$$g(\xi) = \frac{[\varphi - \varphi_c]^n}{[1 - \varphi + \varphi_c]^2} \; ; \quad \xi = \frac{\beta - \beta_0}{\beta_0} \tag{4-13}$$

where β [1/m] is the seismic attenuation of the compressed porous rock and β_0 [1/m] is the seismic attenuation of the intact rock.

Consequently, the *K-C* equation can be modified to express *k* as a function of η, ζ and D_P^2:

$$k(\text{md}) = 9.87 \times 10^8 \cdot \frac{1}{72} \cdot \frac{g(\xi)}{f(\eta)} \cdot [D_P(\text{mm})]^2 \tag{4-14}$$

4.3.3 Correlation between tortuosity factor and P-wave velocity

The percolation porosity, φ_c is the minimum value of the connected porosity at which connected paths through the representative elementary volume exist. The value of φ_c depends on the porosity reduction mechanism, such as mineral precipitation and pressure solution. (Schwartz and Kimminau, 1987) studied grain growth during porosity reduction and found a percolation range of φ_c= 0.02–0.05. Luijendijk and

Gleeson (2015) showed a satisfactory fit to the measured permeability in a sedimentary basin by introducing a calibrated percolation threshold of 0.027. Wardlaw (1987) obtained a percolation range of φ_c from 0.083 to 0.125 by mercury invasion experiments on carbonate porous rocks. Previous studies have shown that the percolation porosity can be as small as zero for thin cracks with continuously connected pore space, or as large as 0.5 for spherical pores.

Figure 4-3 shows the measured permeability data against the porosity of the compressed porous rock samples for the three rock types (sandstone, limestone and bituminous coal). Following the empirical methods of Mavko and Nur (1997), the trial-and-error method was used to obtain the values of the porosity power (n) and percolation porosity (φ_c) in the *K-C* equation.

Seventy pairs of n and φ_c values were used. Values of n between 3 and 9 at intervals of 1 were selected, and φ_c was set between 0 and 0.1 at intervals of 0.01. The optimum values of n and φ_c were determined so as to minimize the differences between the measured permeability and estimated one by the revised *K-C* equation using τ = 7.5:

$$n = 4 \text{ and } \varphi_c = 0.06 \tag{4-15}$$

As mentioned previously, τ may vary because of the change of porosity. Meanwhile, the variation of V_{PG} (η) in the compressed rock particles sample may reveal the tortuous effect. Therefore, the tortuosity τ can be derived from Equation 4-16.

$$\tau = 9.87 \times 10^8 \frac{1}{72} \cdot \frac{(\varphi - 0.06)^4}{(1 - \varphi + 0.06)^2} \cdot \frac{[D_P(\text{mm})]^2}{k(\text{md})} \ , \varphi \geq 0.06 \tag{4-16}$$

The range of the tortuosity was evaluated as τ =5–10 from the measured permeability data.

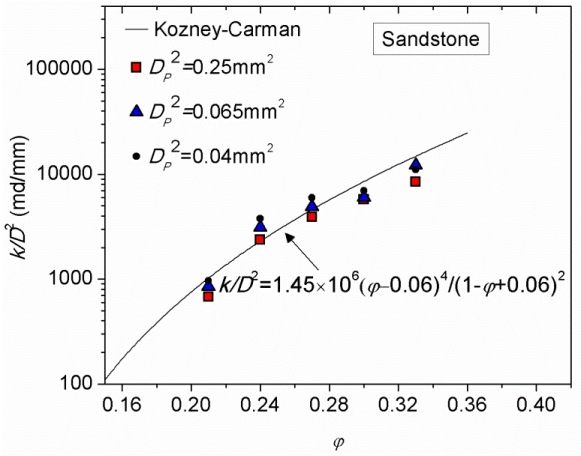

(a)

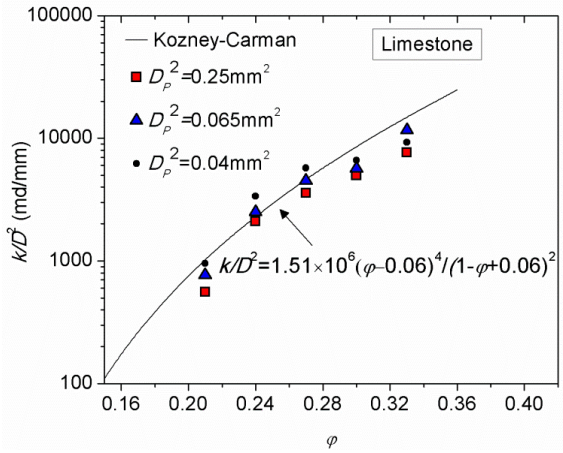

(b)

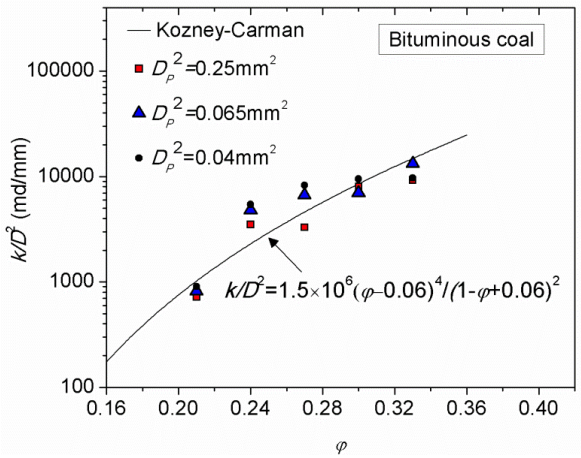

(c)

Figure 4-3. Permeability measurements, normalized by particle size squared, for different rock types and three particle sizes. The solid curve is the *K-C* relation modified to incorporate a percolation threshold porosity of φ_c=0.06 and dependent porosity of φ^4. (a) sandstone, (b) limestone and (c) bituminous coal

Figure 4-4 shows the empirical correlation between the ratio V_{PI}/V_{PG} (η) and $\tau^{1/2}$ measured for the compressed samples with φ = 0.21–0.33.

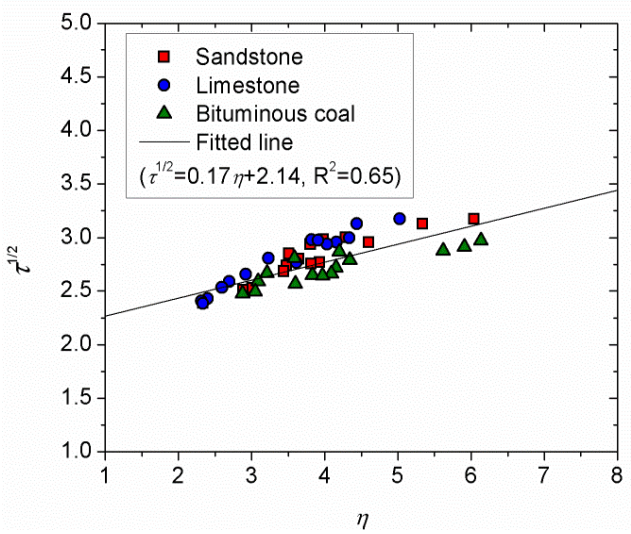

Figure 4-4. Velocity variation coefficient (η) versus tortuosity (τ) for different rock types.

The relation between η and $\tau^{1/2}$ shows a linear one; both τ and η increase with increasing porosity. The relationship can be approximately represented by

$$\tau = f(\eta) = (0.17\eta + 2.14)^2 \quad (4\text{-}17)$$

The range of $\tau^{1/2}$ = 2.3–3.2 or τ = 5 – 10 is corresponding with the range of P-wave velocity change η = 2.3–6.2.

4.3.4 Correlation between the function of porosity in *K-C* equation and seismic attenuation

Figure 4-5 shows ξ against porosity part ($[(\varphi\text{-}\varphi_C)^4/(1\text{-}\varphi+\varphi_C)^2]$) in *K-C* equation. While the seismic variation coefficient ξ in Figure 13 differs between the rock types, ξ showed an approximately linearly relationship as a function of the porosity in the *K-C* equation $g(\xi)$. This indicates that the seismic attenuation is related to the porosity part in the *K-C* equation.

The fitting correlation between ζ and porosity was derived as

$$\mathrm{g}(\xi) = \frac{(\varphi - 0.06)^4}{(1 - \varphi + 0.06)^2} = 1.51 \times 10^{-4}\xi \ ; \ \varphi \geq \varphi_c = 0.06 \tag{4-18}$$

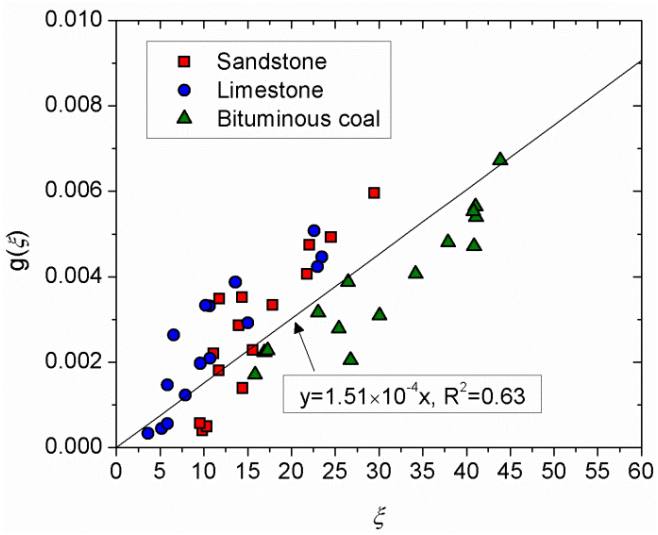

Figure 4-5. Permeability measurements, normalized by particle size squared and tortuosity versus attenuation variation coefficient (ξ) for different rock types.

4.4 Empirical equation for permeability expressed by changes of seismic properties

Substituting Equation 4-17 and Equation 4-18 into Equation 4-14, the *K-C* equation was modified into Equation 4-19 incorporating η, ξ and D_P.

$$k(\mathrm{md}) = 9.87 \times 10^8 \frac{[D_P(\mathrm{mm})]^2}{72(0.17\eta + 2.14)^2}(1.51 \times 10^{-4}\xi) \tag{4-19}$$

Figure 4-6 shows the estimated permeability (*k*') against the measured permeability (*k*). The estimation of permeability derived from Equation 4-19 is in good agreement with the measured values, indicating that the modified *K-C* equation comprising the seismic velocity change, attenuation and particle size D_P^2 can efficiently predict the permeability of the compressed samples of rock particles.

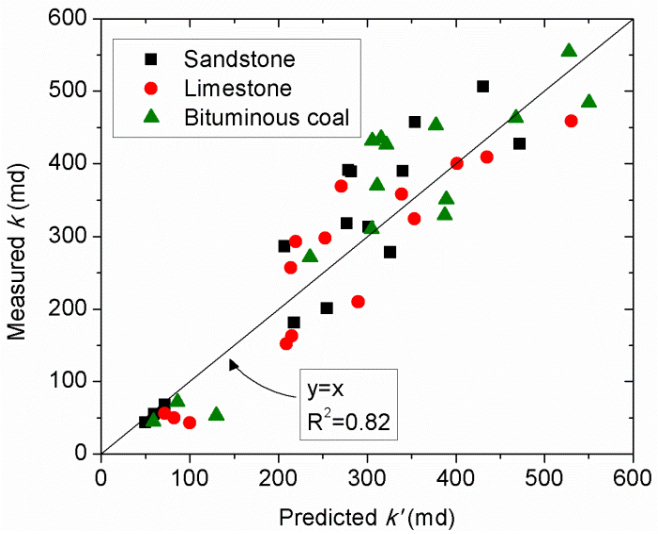

Figure 4-6. Comparison of estimated permeability (k') and measured permeability (k).

4.5 Field application

Studies involving in situ measurement of the permeability in a goaf are very limited apart from a few studies that derived the permeability values based on volumetric strains and geomechanical calculations.

As mentioned previously, the permeability of the actual goaf area can be estimated as follows.

a) Porosity range: φ = 0.23–0.41

b) Average size of fragments in the goaf area: $[D_p]^2 = 6 \times 10^2 – 6 \times 10^4$ mm^2

c) Average tortuosity: τ = 5–10

Based on the empirical equation (Equation 19), gas permeability, k_g through actual goafs is evaluated as

$$k_g = 1 \times 10^7 - 6.5 \times 10^8 \text{ md} = 1 \times 10^4 - 6.5 \times 10^5 \text{ d}$$

The permeability range estimated in our study is within the range of the results presented by the studies described below. Brunner (1985) used gob permeability values ranging from 10^5 to 0^7 d in his ventilation models. Ren et al. (1997) proposed a

permeability of 10^2 d in a compacted goaf. Whittles et al. (2006) reported a range of 10^4 to 5×10^5 d. Szlazak (2009) gave the permeability estimation 5.07×10^3 to 1.01×10^6 d based on the resistance of the rock roof stratification from the caving. Karacan et al. (2007) gave a permeability range of 10^5 to 4×10^5 d according to the *K-C* equation combined with a base permeability coefficient. Karacan (2011) proposed a predictive approach to calculate the porosity and permeability from the size distribution of broken rock mass in a goaf by combining fractal scaling in porous medium with the principles of fluid flow.

4.6 Conclusions

In this chapter, the seismic velocity and attenuation as well as the permeability were measured in 45 porous samples. An empirical equation was proposed to estimate the permeability from the variation in seismic properties and the *K-C* equation. The main results are summarized as follows.

1. The compressed porous samples had relatively high permeability range of 50–600 md with porosity changes of 0.21–0.33. The correlation between permeability and porosity was consistent with the modified *K-C* equation with a percolation threshold porosity of 0.06. The tortuosity (τ) increased from 6-10 with increasing porosity from 0.21-0.33.

2. The P-wave velocity in the compressed porous rock samples with porosities of 0.21- 0.33 was in the range V_p = 400–1100 m/s. The velocity variation coefficient (η) showed a linear relationship with tortosity, τ for the range of τ = 2.5–3.2.

3. The variation coefficient of seismic attenuation (ξ) showed an approximately linear relationship with the part expressed by the function of the porosity in the *K-C* equation.

4. The *K-C* equation was modified and an empirical equation was proposed consisting of η, ξ and D_p. The estimated permeability of the compressed porous

rock samples showed good agreement with the measured data. Our results indicate that the permeability of compressed porous rock in a goaf area can be estimated based on seismic attenuation data. The permeability predicted for the actual goaf is 1×10^4–6.5×10^5 d.

Chapter 5: Simulation on seismic damage on the ground surface above goaf

5.1 Introduction

The abandoned goaf volumes distributed in various parts of China are approximately 432 million m^3 by 2008 (Guo et al., 2012). The goaf areas are vulnerable to cause potential ground deformation and subsidence in a long-term with respect to creep, earthquake vibration and other factors (Aydan et al., 2012). More than 80% of the Chinese coal mines are located in the areas where seismic intensity is expected to be over 7 (Xu et al., 2014). Thus, the effect of earthquake on the coal mine area, especially the ground surface with underlying goaf is imperative to be studied. Additionally, the seismic risk assessment has not yet considered for the effect of goaf areas on dynamic response on the ground surface by now. Therefore, this study focused on the ground seismic response considering the effects of underlying goaf.

The effect of underground structure such as mine roadway and chamber on the seismic wave propagation is relatively slight because the sizes of them are usually much smaller than the seismic wavelength (Wang, 2011). However, if the size of underground structure (such as large-scaled goaf areas) and seismic wavelength are fell into the identical magnitude, the propagation of seismic wave is affected by the goaf areas (Figure 5-1). This fact may generate some unpredictable impacts on the dynamic response on the ground surface.

Crichlow (1982) studied the effect of position, shape, size and depth of underground structure on the seismic motions on the ground surface by two-dimensional finite element model, the geometry of the underground anomalies can be inversely estimated based on the surface seismograms. Aydan et al. (2003) conducted a series of experiments to investigate the dynamic characteristics and amplification of ground

motions using a shaking table. Aydan et al. (2007) also developed a shear layer model utilizing the tributary area concept for assessing the shaking characteristics of ground above abandoned lignite mines. Nasseri-Moghaddam et al. (2007) conducted multi-channel analysis of surface waves over void space, and found that a part of the seismic energy is trapped in the void and attenuated by radiation. Nie et al. (2013) focused on goaf surface subsidence under the influence of the interaction between seismic and fault. Smerzini et al. (2009) presented a theoretical approach for SH wave propagation to study the impact of underground cavities on the surface motion.

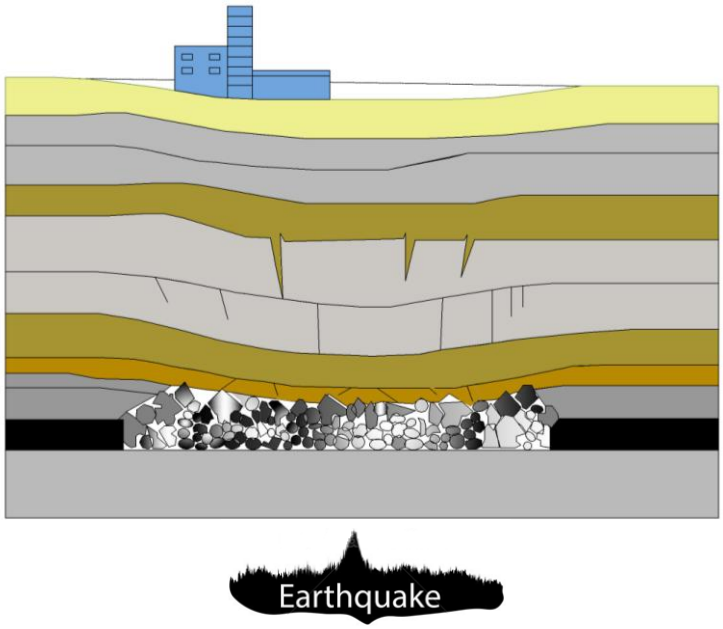

Figure 5-1. The schematic of surface seismic response under the integration of earthquake and underground goaf.

Most of the previous studies focused on the impact of shallow-buried structures rather than deep ones on the surface seismic response. The geometry of anomalies, such as size and depth, have been discussed as well. Meanwhile, the majority of the experiments and simulation models treat the goaf to be void space, which does not conform the actual situation. For instance, around 90% of Chinese coal mines utilize longwall mining and roof collapsed method (Huang et al., 2017). The goaf areas

formed subsequently are stuffed by broken rock rather than void space. Besides, the goaf is always treated as homogenous, isotropic and linear visco-elastic in the previous study (Vardoulakis et al., 1987). It was approved that the goaf area has a strong adsorbed effect on the seismic energy because of the discontinuity characteristics . In the most of the previous researches, the energy-absorbed effect is expressed by the degradation of modulus or mechanical damping obtained from the empirical correlations. In the contrast, the goaf area and overburden strata might be reactive under the vibration of earthquake, as a result, the surface seismic response above goaf area could be different from the places over the undisturbed strata. In the simulation study, the damping property is an important parameter to estimate the effect of absorption on the seismic amplitude and energy (Group, 2012). The damping parameter, functions of the material modulus, geometry size, fragmented condition, properties of dynamic wave, has not been estimated clearly and further investigation are needed.

Elastic modulus of goaf area was measured from large scale in-situ tests and detailed laboratory studies as well as the simulation study by Wardle and Enever (1983). They conducted a *in-situ* test of caved waste piles from the roof failure in an Australia coal mine. The result showed the elastic modulus at around E=21.4 MPa under a maximum stress of σ=1.37 MPa. Meanwhile, Smart and Haley (1987) used a hydraulic jacking apply on a stone-built pillar in the United Kingdom, got a result of 20.7MPa for the elastic modulus under a vertical pressure of 5.5MPa. Xie et al. (1999) suggested the following formula for determination of the modulus of elasticity of goaf material with respect to time based on the mass field data of coal mines in China and USA. Fujii et al. (2011) measured the Young's modulus of clastic-rock using a Goodman jack and provided a value of 500MPa around the borehole in the old closed roadway in 300 m deep at the Kushiro coal mine, Japan. Pappas and Mark (1993) conducted numerous of laboratory experiments to test the deformation modulus of the goaf material. He used the size scale-down method to simulate the goaf fragments size distribution in lab-scale. the secant modulus showed 0.7-63 MPa over the porosity from 0.1 to 0.8. Tajduś (2009)

found that the elastic moduli in horizontal direction and in vertical direction are very low, in range of 50–150 MPa. Meanwhile, a review of the elastic modulus used in numerical simulation showed a relative higher and wider modulus values from 6.9 to 2400 MPa for the goaf. Following the rule for estimating the goaf modulus presented by Peng , Hsiung and Peng (1985) proposed the goaf elastic modulus should be based on rock type and void ratio. Cheng et al. (2010) and Jiang et al. (2012) assigned goaf material with elastic modulus and Poisson's ratio as190 MPa and 0.25 respectively. Kose and Cebi (1988) suggested a wide interval such as 15–3500 MPa for the modulus of elasticity value for goaf material. Su (1991) chose the elastic modulus ranging from 72 to 2900MPa reflecting the bilinear behavior of the goaf.

In this simulation, we attempted to assign the reasonable elastic modulus to the goaf area in the simulation model, and to obtain the empirical equation for estimating the damping coefficient by laboratory measurement. The estimated damping coefficients were input for the simulation model to analyze the effect of the goaf on the seismic wave propagating through it and evaluate the seismic response on the ground surface.

5.2 Field case in Tangshan earthquake

In order to analyze the influence of goaf areas on dynamic response at the ground surface, the data of seismic intensity, surface deformation and collapse rate of houses were collected from Kailuan mining areas and villages in vicinity. The data were based on the recorded data by Chinese Seismological Bureau. Kailuan mining area which consists of 8 coal mines is an indispensible coal industry base in China. The entire mining area contains more than 10 coal-bearing layers. The massive goaf areas are spread more than 40 km^2. The distributions of the abandoned goaf areas and seismic intensity are revealed in Figure 5-2. As shown in Table 5-1, the damages of the industrial and civil constructions on the ground in mining areas were incredibly devastated, while the damages in some places at mining areas exhibited smaller than those of similar constructions located in the same intensity region.

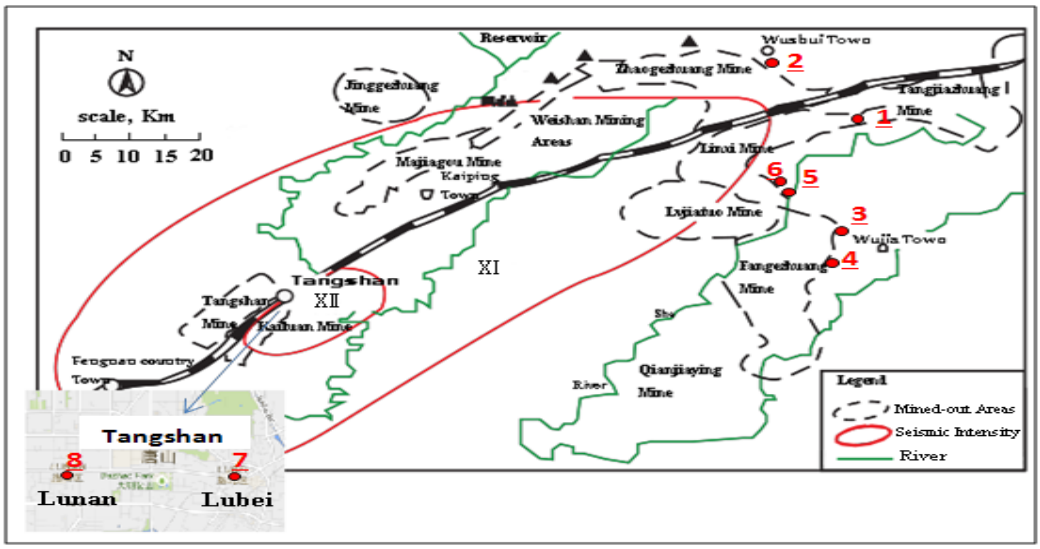

Figure 5-2. Distribution of mined-out areas and seismic intensity region in Kailuan mining areas.

The Renjiatao village located just above the goaf areas of Tangjiazhuang mine (P#1) had less surface deformation and subsidence phenomenon. The destruction of the structures adjacent to the edge of the goaf areas even appeared decreasing tendency of seismic damage. For instance, the coal preparation plant ,strap traverse and coal bunker near Zhaogezhuang goaf areas (P#2) suffered seismic intensity of Ⅷ, whereas other structures located in the same region had undergo the intensity of Ⅹ. In addition, the collapse rates of Hourenlizhuang (P#3) and Paigezhuang (P#4) which near the edge of Fangezhuang goaf areas were remarkably lower than the buildings nearby. Meanwhile, Shuanghe village (P#5), Xiaozhuangtuo village (P#6) and three other villages near the edge of goaf areas of Linxi mine suffered less damage compared to the other constructions in the same intensity region. Especially, the destructions of Lubei district (P#7) in Tangshan city with overlying goaf areas were smaller than those of Lunan district (P#8) which had no goaf in the underground. These phenomena proved that the goaf areas have no amplification effect on the seismic damage at the ground surface. On the contrary, goaf areas generate some decreasing effects on the seismic destruction in some regions at the ground surface.

Table 5-1. Comparison of seismic intensity above the goaf of Kailuan mining area and the region above undistributed area

P	Detail name	Longitude and Latitude	Seismic Intensity	Intensity of undisturbed area
1	Ground surface above goaf areas of Tangjiazhuang Mine	39 °43'23.4" N118 °32'19.3"E	Ⅸ	Ⅹ
2	Industry square near the goaf edge of Zhaogezhuang Mine	39 °47'30.0"N 118 °30'19.3"E	Ⅷ	Ⅹ
3	Hourenli village near the goaf edge of Fangezhuang Mine	39 °38'38.4"N 118 °27'41.7"E	Ⅷ	Ⅹ
4	Paige village near the goaf edge of Fangezhuang Mine	39 °37'22.3"N 118 °27'31.1"E	Ⅷ	Ⅹ
5	Shuanghe village near the goaf edge of Linxi Mine	39 °42'38.9"N 118 °26'12.8"E	Ⅸ	Ⅹ
6	Xiaozhuangtuo village near the goaf edge of Linxi Mine	39 °42'01.0"N 118 °26'00.4"E	Ⅸ	Ⅹ
7	Lubei district with underlying goaf areas	39 °37'20.6"N 118 °11'57.3"E	Ⅺ	Ⅻ
8	Lunan district without underlying goaf areas	39 °35'23.3"N118 °10'10.7 "E	Ⅻ	Ⅻ

Consequently, throughout the field observation, it is interesting to find the existence of goaf has no obviously increased damage, instead, some places around the goaf shows lighter damage compared to other places on the ground surface. We therefore used FLAC3D simulator to further analyze the effect of goaf on the seismic response on the ground surface due to it is widely applied in rock mechanics and dynamic issues.

5.3 Selection of properties in the simulation model

5.3.1 Steps of simulation

The procedures of the simulation calculation is shown in Figure 5-3. In the static calculation of initial geostress, the elastic modulus of the intact samples used in laboratory is assigned to the strata of the model. The modulus of goaf area are

subsequently replaced considering the depth and compaction time. In the dynamic calculation, the B-R model proposed in Chapter 3 was employed to yield the damping coefficient of in the goaf to highlight the fragmented characteristic of goaf. The detailed steps of simulation conduct are list below,

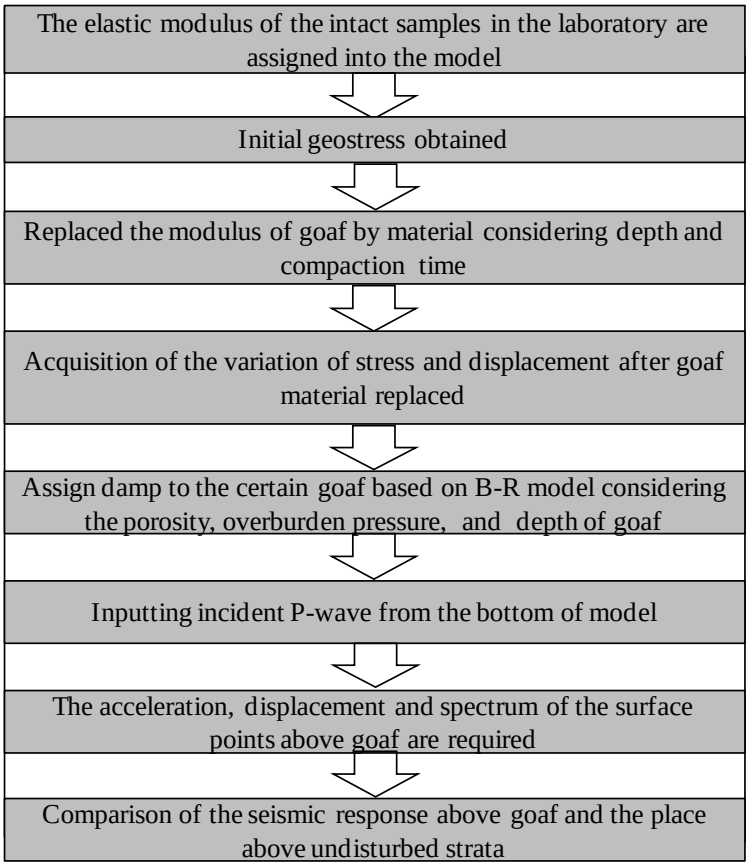

Figure 5-3. Schematic of the steps of simulation.

5.3.2. The principle of dynamic calculation

Dynamic calculation is performed by fully calculated considering the motion equation shown in Equation 5-1. Then the strain increment of element is computed dependent on the velocity of nodes by using Equation 5-2. Subsequently, the stress increment of element is acquired based on the constitutive model in Equation 5-3. The total stress is obtained by superposition of stress increment at each time step. The acceleration, velocity and displacement of nodes and stress of elements are finally derived by means of the algorithm below.

$$F_i^{\langle l \rangle} + I_i^{\langle l \rangle} = M^{\langle l \rangle} \left(\frac{dV_i}{dt} \right)^{\langle l \rangle}, \quad l = 1, \ldots n_n \tag{5-1}$$

where $F_i^{<l>}$ [N] is unbalanced force at node l in i direction, $I_i^{<l>}$ [N] is damp force at node l in i direction, M [kg] is lumped mass at node l, V_i [m/s] is the velocity at node l in i direction, t [s] is time.

$$\Delta e_{ij} = \frac{1}{2} \left(\frac{\partial V_i^{\langle l \rangle}}{\partial x_j} + \frac{\partial V_j^{\langle l \rangle}}{\partial x_i} \right) \Delta t \tag{5-2}$$

where Δe_{ij} [-] is strain increment of element, $V_i^{<l>}$ [m/s] is the velocity at node l in i direction, Δt [s] is time step.

$$\Delta \hat{\sigma}_{ij} = H\left(\Delta \sigma_{ij}, \chi_{ij} \Delta t \right) \tag{5-3}$$

where $\Delta \hat{\sigma}_{ij}$[Pa] is co-rotational stress increment, H_{ij} is a given function, $\Delta \sigma_{ij}$ [Pa] is stress increment, χ_{ij} [-] is strain rate tensor.

5.3.3. Establish of the model

Figure 5-4 shows the three-dimension of the model established by simulator.

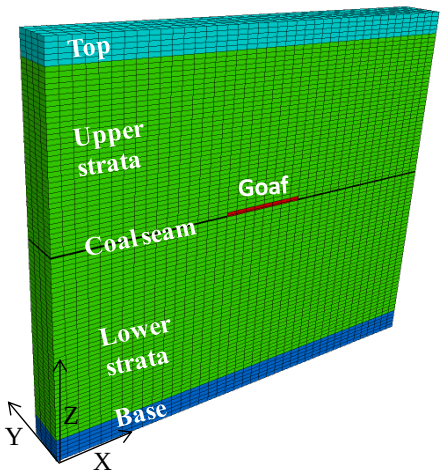

Figure 5-4. Three-dimensional model.

The model is 1000m long in X direction, 850m high in Z direction and 100m wide in Y direction, respectively. Coal seam thickness is 2m and goaf area is set in the middle of the coal seam with 150m long, 100m wide and 10m high (Equation 5-4). Elasto-Plastic constitutive model and Mohr-Coulomb failure criterion were employed in this simulation.

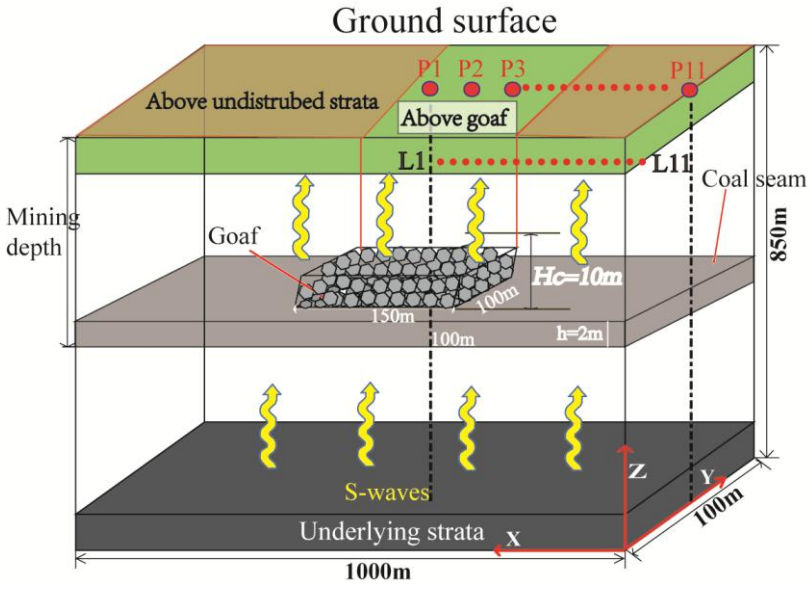

Figure 5-5. Schematic illustration of goaf area in the model.

$$H = \frac{100h}{c_1 h + c_2} + c_3 \tag{5-4}$$

where H [m] is the height of goaf; h [m] is the extraction thickness; and c_1, c_2 and c_3 are coefficients that reflect the lithology of the surrounding rock. For average conditions in the goaf area in a coal mine, c_1 = 4.7 m^{-1}, c_2 = 19 and c_3 = 2.2 m were adopted by Yavuz (2004).

Some monitoring points are set on the ground surface (Figure 5-4). Point #1 is set above the center of goaf area as well as Point #2 set above the edge of the goaf area. Points #3-11 are set above the undistrubed ground with the same interval of 50 m in X direction. Meanwhile, L_1-L_{11} with some monitoring points are set along the vertical axis Y.

5.3.4. Properties of the undistrubed strata and goaf area

(a) Undisturbed strata

In the simulation, the model was constrcted by top, upperr strata, coal seam, goaf, lower strata and base block. The elastic modulus and damping coefficient of the undisturbed strata were assgned based on the laboratory measurement on the intact core samples. The detailed properties used in the simulations are shown in the table below.

Table 5-2. Rock properties of the undisturbed strata

Properties	Base	Top	Upper	Lower	Coal
Bulk modulus(MPa)	10000	2170	6550	6500	1400
Shear modulus(MPa)	7500	1200	4700	4700	430
Cohesion (MPa)	8	4	5	5	5
Tensile strength (MPa)	7	3.4	4	4	4
Frictional angle (°)	38	30	34	34	32
Density (kg/m^3)	2500	2300	2400	2400	2000
Damping coefficient	0.03	0.08	0.035	0.035	0.07

(b) Goaf areas

It has been observed that the elastic modulus of the goaf material has a wide range, which is approximately from 20 to 3000MPa. It has been known that because of the fragmentation of the goaf material, the elastic modulus is dependent on the effective stress applied on the goaf area as well as the distribution of the fragmented rock in the goaf.

Furthermore, it has been observed that the goaf area shows the creep characteristic with the time goes by which results in a nonlinear mechanical behavior. Therefore, the definition of elastic modulus of goaf material in simulation study should consider the effective stress, porosity, size distribution and compaction time. Following Pappas and Mark (1993) and Yavuz (2004), the goaf area can be treated as an elastic material with a

certain elastic modulus varying with time. The initial elastic modulus, $\widetilde{E_0}$ (MPa), can be calculated as a function of the unconfined compressive strength of the intact rock, σ_c, and the buckling factor, *BF*.

$$\tilde{E}_0 = \frac{10.39{\sigma_c}^{1.042}}{BF^{7.7}}, \qquad BF = \frac{1}{1-\varphi_0} \tag{5-5}$$

Therefore, the initial elastic modulus of goaf area can be estimated by the compressive strength of the intact rock (σ_c) and the initial porosity (φ_0).

According to our laboratory measurement, the initial porosity (φ_0) is related to the critical porosity (φ_c) and overburden stress (σ).

$$\varphi_0 = \varphi_c \exp(-1.412 \times 10^{-2}\sigma) \tag{5-6}$$

With the knowledge that the critical porosity is affected by some major microstructural parameters, including grain size, grain packing, particle shape, and the distribution of grain sizes. For the random packing of sand, the critical porosity is around σ_c=0.399 (Clover, 2008) which is similar to our observation in the experiment of 0.39. Therefore, 0.39 is defined as the critical porosity of goaf. The initial porosity is dependent on the overburden pressure (σ) above the goaf, we therefore firstly acquired the overburden stress at the roof place above goaf in the static calculation of simulation. Then, the initial porosity is obtained from Equation 5-6 in the simulation part, we considered the different depth of goaf, the initial porosity is therefore varied with the change in depth of goaf resulting from the discrepancy of overburden stress.

Jiang et al. (2012) assigned goaf material with Poisson ratio (ν) of 0.25. Meanwhile, Xie (1999) suggested the Poission ratio of goaf ranges from 0.25 to 0.05 with time goes by. The initial Poission ratio herein is therefore assigned to be 0.25.

The goaf is filled with fragmented rock mass, with the time goes by, the void in the goaf area will be gradually consolidated. This process results in a porosity decrease in the

goaf area and subsidence on the ground surface. Because of the creep character of goaf material, the elastic modulus varies with time. According to the *in-situ* investigation and by Xie (1996) , the elastic modulus of goaf increases with time as

$$\tilde{E}(t) = 175(1 - e^{-1.25t}) + E_0 \tag{5-7}$$

where t is compaction time, [year].

The elastic modulus of goaf at different depths changing with time are shown as

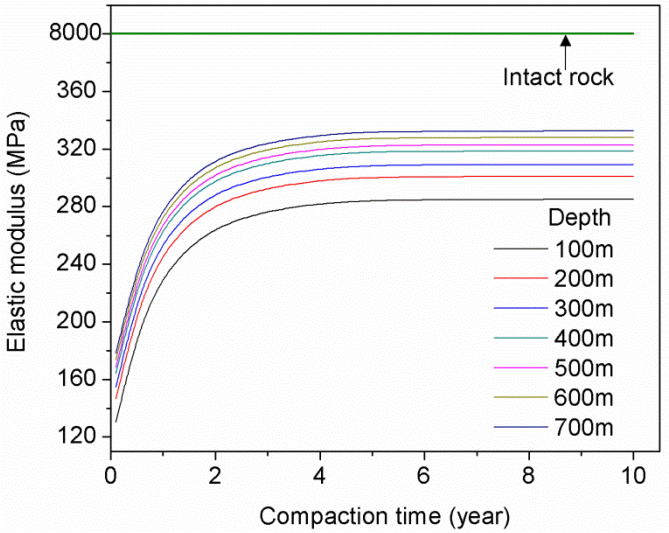

Figure 5-6. Elastic modulus of goaf changes with time.

Meanwhile, the variation of porosity with time, $\Delta\varphi(t)$, can be estimated by the strain variation ($\Delta\varepsilon$) of goaf material as

$$\Delta\varphi(t) = \Delta\varepsilon = \frac{\sigma}{E(t)}\Big|_0^t \tag{5-8}$$

where σ [MPa] is the overburden stress.

In the approach described above, the porosity of the goaf considering different overburden stress and compaction time can be estimated by

$$\varphi(t) = \varphi_c \exp(-1.412 \times 10^{-2}\sigma_n) - \Delta\varphi(t) \quad (5\text{-}9)$$

It has been known that the creep behavior of goaf ususlly happens in ten years after mining. Therefore, 10 years is the maximum time considered in Equation 5-7. The bulk and shear moduli of goaf used in the simulation under differnet cases were therefore can be yielded and listed below;

Table 5-3. Properties of goaf materials for the cases of different depths and compaction time

Depth	Properties\Time (year)	0.1	0.5	1	2	4	6	10
100	Modulus\Porosity	0.368	0.367	0.364	0.360	0.352	0.344	0.341
	Bulk modulus (*B*)	50.47	58.27	66.80	76.11	86.13	96.93	108.00
	Shear modulus (*G*)	30.28	34.96	40.08	45.66	51.68	58.16	64.80
200	Modulus\Porosity	0.356	0.355	0.350	0.343	0.329	0.314	0.309
	Bulk modulus (*B*)	52.26	60.06	68.59	77.90	87.93	98.73	109.79
	Shear modulus (*G*)	31.36	36.04	41.16	46.74	52.76	59.24	65.88
300	Modulus\Porosity	0.345	0.343	0.337	0.329	0.311	0.291	0.283
	Bulk modulus (*B*)	58.72	66.52	75.06	84.36	94.39	105.19	116.26
	Shear modulus (*G*)	35.23	39.91	45.03	50.62	56.63	63.11	69.75
400	Modulus\Porosity	0.333	0.332	0.326	0.317	0.297	0.273	0.263
	Bulk modulus (*B*)	69.03	76.83	85.36	94.67	104.69	115.49	126.56
	Shear modulus (*G*)	41.42	46.10	51.22	56.80	62.82	69.30	75.94
500	Modulus\Porosity	0.323	0.321	0.315	0.308	0.287	0.261	0.250
	Bulk modulus (*B*)	111.59	119.39	127.92	137.23	147.25	158.05	169.12
	Shear modulus (*G*)	66.95	71.63	76.75	82.34	88.35	94.83	101.47
600	Modulus\Porosity	0.312	0.310	0.305	0.297	0.275	0.245	0.232
	Bulk modulus (*B*)	268.71	276.51	285.04	294.35	304.37	315.17	326.24
	Shear modulus (*G*)	161.22	165.90	171.02	176.61	182.62	189.10	195.74
700	Modulus\Porosity	0.302	0.300	0.295	0.287	0.265	0.234	0.220
	Bulk modulus (*B*)	521.83	529.63	538.16	547.47	557.49	568.29	579.36
	Shear modulus (*G*)	313.10	317.78	322.90	328.48	334.50	340.98	347.62

5.4 Damping coefficient of goaf material

For estimating the effect of fragmented goaf on the seismic propagation, damping coefficient should be an important factor. In FLAC3D three kinds of damping are provided including Rayleigh damping, local damping and hysteretic damping. Rayleigh damping is dependent on the frequency and damping ratio. Local damping is only dependent on damping ratio, and hysteretic is an incorporation of strain-dependent damping ratio and secant modulus function. Because of the independent on frequency and high-speed convergence of local damping, local damping was selected in this simulation.

Local damping operates by adding or subtracting mass from a gridpoint or structural node at certain times during a cycle of oscillation; there is overall conservation of mass, because the added amount is equal to the subtracted amount. Mass is added when the velocity changes sign and subtracted when it passes a maximum or minimum point. Hence, increments of kinetic energy are removed twice per oscillation cycle.

The amount of removed energy, ΔW, is proportional to the maximum transient strain energy, W, and the ratio, $\Delta W/W$, is independent on frequency. Since $\Delta W/W$ is related to the critical damping ratio, ζ (Kolsky, 1963)

$$\alpha_L = \pi\zeta \tag{5-10}$$

where α_L is the local damping coefficient.

As is known that critical damping ratio is related to the quality factor shown as

$$\zeta = \frac{1}{2Q} = \frac{\beta V}{\pi f} \tag{5-11}$$

where Q [-] is quality factor, β [1/m] is the seismic attenuation; V [m/s] is the P-wave velocity; f [Hz] is the incident frequency.

In this way, therefore, the local damping coefficient α_L is obtained from

$$\alpha_L = \frac{\beta V}{2f} \tag{5-12}$$

For the unconsolidated sedimentary formation (Wang et al., 2009),

$$\frac{1}{Q_S} = \frac{3\gamma^2}{4}\left(1 - \frac{3K^*}{4\mu^*} + \left(\frac{3K^*}{4\mu^*}\right)^2 + \cdots\right)\frac{1}{Q_p} \tag{5-13}$$

where *Qp* [-] is the quality factor of shear wave; Q_S [-] is the quality factor of shear wave; γ [-] is the ratio of the P-wave velocity (V_P) to the S-wave velocity (V_S). K^* [MPa] and μ^* [MPa] are the bulk and shear modulus of the viscosity component.

Because, the S-wave displays much more attenuation than the P-wave in unconsolidated rock, $k^* < \frac{4}{3}\mu^*$ is always true, therefore

$$\frac{1}{Q_S} \approx \frac{3\gamma^2}{4}\frac{1}{Q_p}$$

Based on the relationship between quality factor (Q) and attenuation (β), therefore,

$$\frac{\beta_S}{\beta_P} = \frac{3}{4}\frac{V_{PC}}{V_{SC}} = \frac{3}{4}\sqrt{\frac{K_C + 4/3G_C}{G_C}} \tag{5-14}$$

where K_C [MPa] and G_C [MPa] are the bulk and shear modulus of the compressed media.

In Chapter 2, the seismic attenuation and velocity of the porous layer has been presented. Therefore, the damping coefficient of the goaf area for the cases of different depth and compaction time can be expressed as

$$\alpha_{Ls} = \frac{3}{4}\sqrt{\frac{K_C + 4/3G_C}{G_C}}\left[\beta_0 + \frac{1}{D}\sqrt{(1-2.07\varphi)V_{PI}}\left(-ln\left|\frac{\kappa/I}{\sqrt{\pi^2 f^2 + (\kappa/I)^2}}\right|\right)\right]\cdot(1-2.07\varphi)\frac{V_{PI}}{2f} \quad (5\text{-}15)$$

Therefore, α_{LS} can be derived from the model in terms of the porosity, frequency, particle size and loading. In this approach, a reasonable damping parameter was input to simulate the seismic attenuation propagating through the goaf area in the field-scale simulation. Frequency (f) was defined as 1.74Hz by the dominated frequency in FFT of incident wave (Figure 5-7). The diameter of fragment was set as 150mm based on the observation in the actual goaf (Figure 2-11).

The damping coefficients of the goaf at differnet depths and compaction time are listed below

Table 5-4. The damping coefficient, α_L through goaf of different depths and compaction time for numerical simulations

Depth\Time(year)	0.1	0.5	1	2	4	6	10
100	0.191	0.190	0.187	0.182	0.174	0.165	0.162
200	0.178	0.177	0.171	0.164	0.151	0.138	0.134
300	0.166	0.164	0.159	0.151	0.136	0.120	0.115
400	0.155	0.154	0.148	0.141	0.125	0.108	0.102
500	0.146	0.144	0.139	0.133	0.118	0.101	0.094
600	0.137	0.135	0.131	0.125	0.109	0.091	0.084
700	0.129	0.127	0.123	0.118	0.103	0.086	0.079

5.5 Test waves and dynamic parameters

The segments of Kobe waves (a_{max}=0.35g) of 0-10 s are extracted and performed in this part (Figure 5-7). The main frequency of the Kobe waves is distributed in the range of 0-8 Hz. The frequency at the maximum acceleration is 1.74 Hz.

As shown in the spectrum analysis of the incident waves (Figure 5-8), the energy is

dominated within 8Hz, which corresponds to 16m in wavelength in the goaf areas. Kuhlemeyer and Lysmer showed that for accurate calculation of wave propagation through the model, the spatial element size must be smaller than approximately 1/10 to 1/8 of the minimum wavelength.

Hence, the longitudinal mesh of the goaf area is defined as 1m. In the dynamic simulation, free-filed boundaries were adopted on the lateral sides of model, and viscous boundary was employed at the bottom of the model. The stress waves transformed from acceleration waves were applied into the bottom in the form of shear waves.

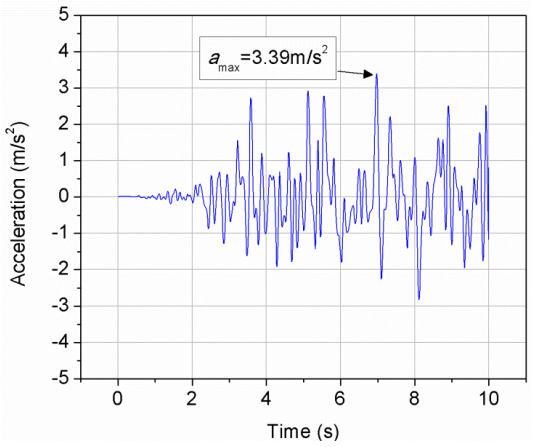

Figure 5-7. Incident Kobe acceleration waves.

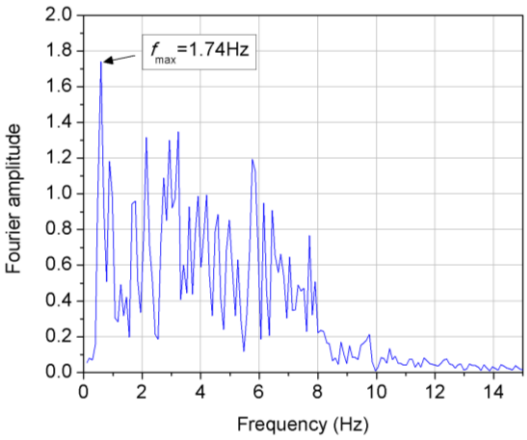

Figure 5-8. FFT of the incident wave.

5.6 Results and discussions

5.6.1 Time-history acceleration on the ground surface

In the seismic field, the acceleration is the most important factor to estimate the seismic response. We therefore herein observed the acceleration time-history curve of point #1 which right above the goaf center on the ground surface. Figure 5-8 shows the seismic time-history accelerations at point #1 for three different depths of the goaf (Figure 5-9, a-c) and the free-field (Figure 5-9, d).

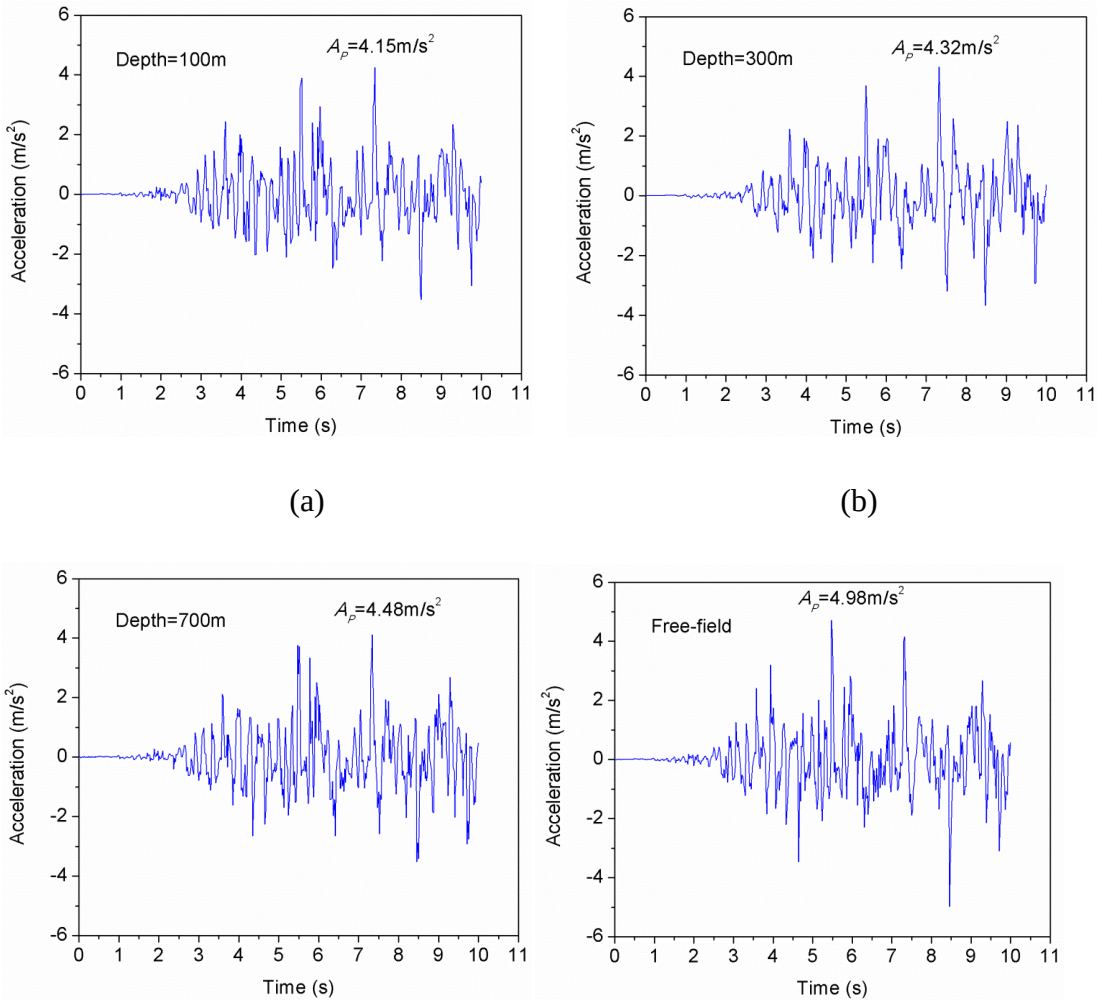

Figure 5-9. Acceleration of point #1 above goaf at different depths. (a) 100m, (b) 400m, (c) 700m and (d) free-field

The acceleration amplitude at point #1 was observed to be reduced comparing to that of free-field regardless of the goaf depth. Meanwhile, the amplitude was gradually increased with increasing depth.

It is clear that the presence of goaf reduces the acceleration in 16.7% on the ground surface above the goaf area. Moreover, the effect of goaf on the acceleration above goaf is getting smaller to 10% with the increase of depth.

5.6.2 Peak ground acceleration (PGA) above goaf for the cases of different depths and compaction time

Peak ground acceleration (PGA) is widely used as an effective tool to estimate the seismic damage. PGA is equal to the maximum ground acceleration that occurred during earthquake shaking at a location. To clarify the different PGA between the cases of existence and inexistence of goaf, we used the ratio of PGA above the goaf, a_p and that of the free-field case, a_f to estimate the effect of goaf on PGA values, and D_C refers to the horizontal distance of the points on the ground surface to the center of goaf.

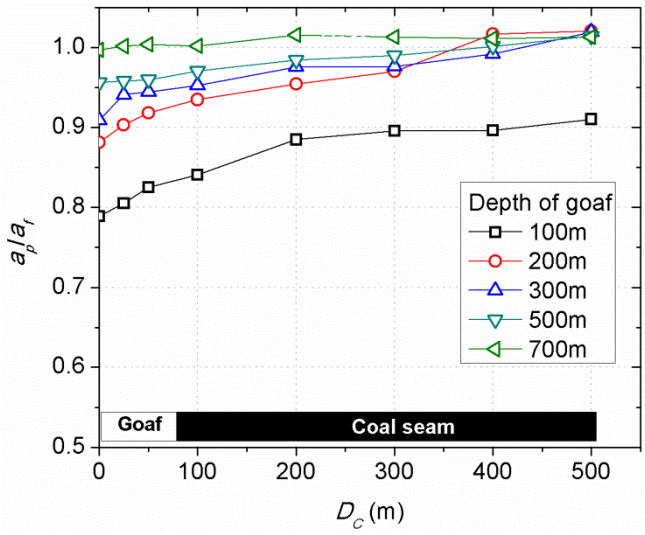

Figure 5-10. Ratio of PGA in the presence of goaf and that of free-field for the conditions of different depths of goaf.

Because the model is symmetric, therefore the PGA values of the monitoring points were selected at the right half of the model to study. It can be clearly seen in Figure 5-10 that the existence of goaf reduces the PGA values compared to that of free-field condition. Especially the location that above goaf, the PGA is around 20% reduction compared to the region above virgin undistributed strata. Meanwhile, as the increase of depth from 100 to 600 m, the reduction of PGA above goaf gradually decreases from 20 to 9%, and close to the free-field condition when depth of goaf is 700m. The reduction of PGA in the simulation exhibited a consistency to the phenomenon reported

in Tangshan earthquake (Anon, 1978) that the damage above goaf is not larger than other places, instead, the damage was relatively small.

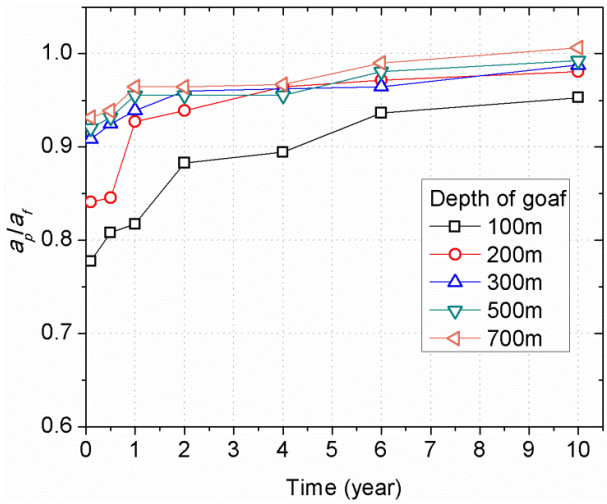

Figure 5-11. Effect of compaction time on PGA in the goaf-presence region.

To further understand the effect of compaction time on PGA in the goaf region. Figure 5-11 shows PGA at point #1 compared with the free-field PGA for the case of 300m-depth-goaf at different compaction time. It can be found the peak acceleration at point #1 is much smaller for the short-compaction-time goaf. It indicates that the wave amplitude is much attenuated in the uncompacted goaf. Meanwhile, the reduction especially becomes large above the shallow-goaf such as 100m depth. As the increase time of consolidation from 0.1 to 10 years, the reduction of PGA above goaf is decreased from 20 to 7% compared to that of the free-field one.

5.6.3 The variation of peak acceleration crossing the goafs of the cases of different depths and compaction time

In the last section, we simulated the PGA reduced above the goaf. To further understand the variation of acceleration before and after crossing the goaf area, the peak accelerations in the vertical direction are monitored by *L1-L11* line set in the model. The values of peak accelerations were then input Matlab to plot the contour of the peak accelerations of the whole model (Figure 5-12).

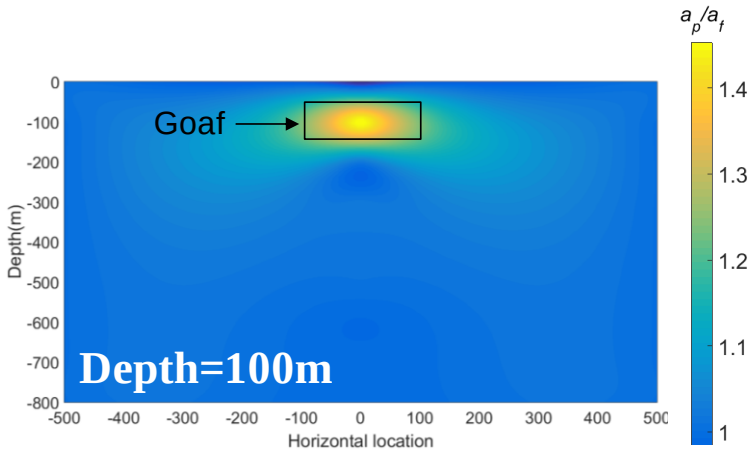

(a)

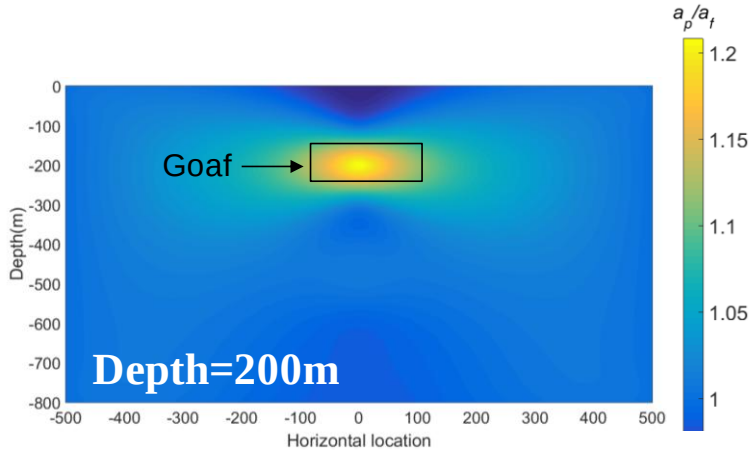

(b)

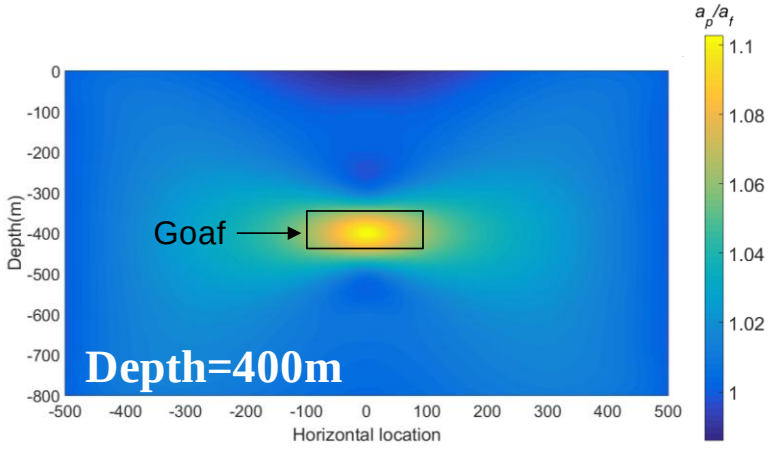

(c)

Figure 5-12. Variation of peak accelerations propagating through the different depths of goaf. (a) 100m (b) 200m and (c) 400m

The peak acceleration is considerable amplified inside the goaf area. The amplification is more than 25% compared to the undisturbed places. This is because the mechanical property of goaf material is much weaker and more vulnerable to the seismic force. The seismic energy is trapped in the goaf area leading to a reduction of energy transmitted through the goaf area. The PGA above goaf is therefore decreased around 10-20% compared with PGA above undisturbed strata.

Meanwhile, it can be seen that the energy trapped in goaf area becomes smaller from 35 to 25% as the increase of depth from 100 to 500 m. Those results explained the reason why the reduction effect of goaf on the PGA is gradually decreased with the increasing depth of goaf.

The reduction of PGA above goaf and amplification of acceleration in goaf area indicates that the existence of goaf has a role like buffer layer when earthquake happens. The seismic energy is trapped in the goaf area results in a reduction of energy transmitted to the ground surface through the goaf.

To examine the effect of compaction time on the acceleration amplification in goaf area, the peak acceleration with a 100m-depth-goaf with the compaction time of 0.1 year, 1 year, 2 years and 4 years were plotted in Figure 5-13.

It can be observed that the amplification of peak acceleration in goaf is decreased from 1.5 to 1.2 with the increasing compaction time from 0.1 to 2 years.

The reduction of PGA and amplification of acceleration in goaf area indicates that the existence of goaf plays a role of buffer layer when earthquake happens. The seismic energy is trapped in the goaf area results in a reduction of energy transmitted through the goaf to the ground surface. The amplification of peak acceleration in the goaf is decreased with the increasing depth and compaction time, which results in the corresponding variation of PGA above goaf.

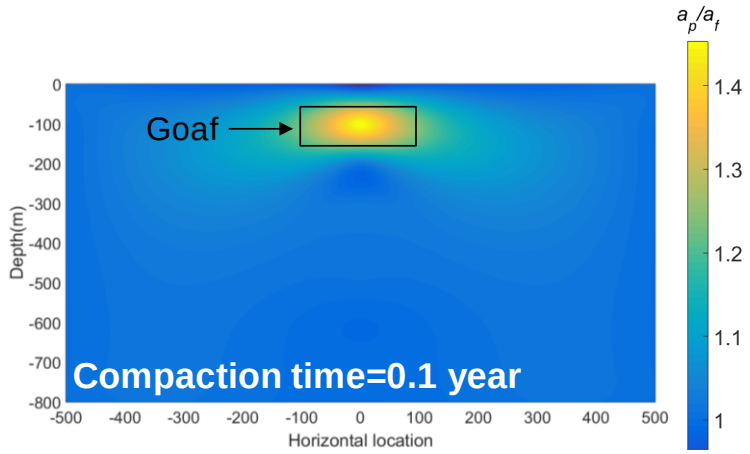

(a)

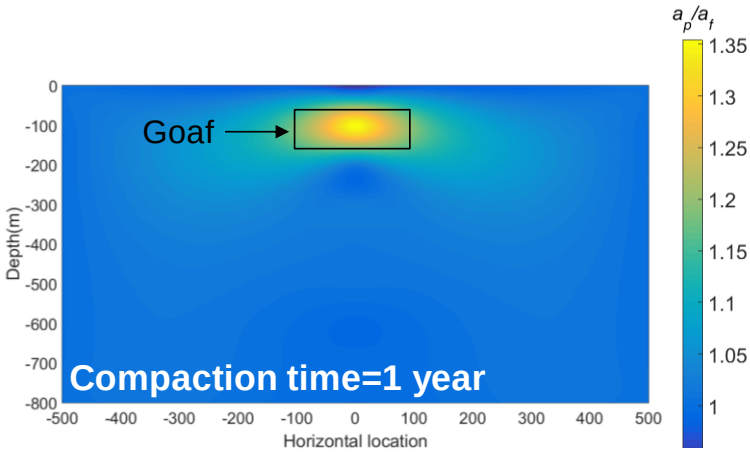

(b)

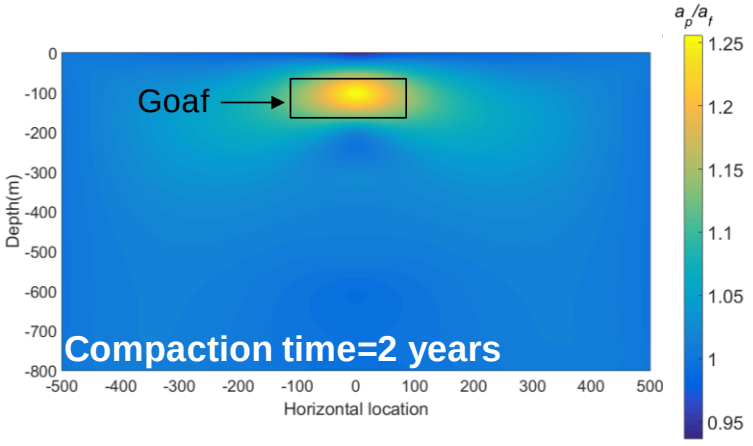

(c)

Figure 5-13. Variation of peak acceleration through the goaf under different compaction time. (a) 0.1 year, (b) 1 year, and (d) 2 years.

5.6.4 Seismic displacement on the ground surface above a goaf

In considering the seismic damage by earthquake, peak displacement on the ground surface (PGD) is another indicator to infer the range and degree of destruction. PGD refers to the maximum ground displacement that occurred during earthquake shaking at a location. PDG is used to estimate the displacement degree on the ground surface in terms of the existence of goaf. The ratio of PGD_g (PGD above goaf) and PGD_f (PGD above free-field) is used to evaluate the degree of seismic displacement.

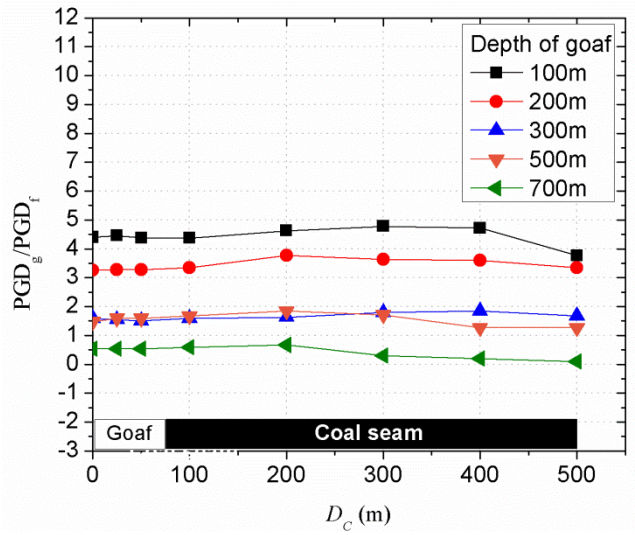

Figure 5-14. Ratio of PGD_g and PGD_f at different positions away from goaf on the ground surface.

Figure 5-14 shows the PGD above the goaf area and free-field. It can be seen that PGD_g is larger than PGD_f. The amplification is increased from 1 to 6 with the reduction of depth changing from 700 to 100. Additionally, the amplification is not only the region above goaf but also the region above the undisturbed coal seam. This indicates the goaf largely effects the displacements on the ground surface. Meanwhile, the PGD_g above the goaf is around 10% than that above the undisturbed coal seam. While, the decrease effect gradually declines with increasing depth of goaf.

Figure 5-15 shows the variation of PGD_g at P#1 with the increasing compaction time. It

can be seen that the PGD_g is decreased as the compaction time increases. The slope of decrease is getting larger with the reduction of depth of goaf. Which indicates the peak displacement increases faster with the increasing compaction time for the case of shallow goaf. Meanwhile, the amplification of PGD_g is slighter when compaction time close to 10 years. This revealed that the consolidation of goaf could reduce the seismic displacement on the around surface above goaf area.

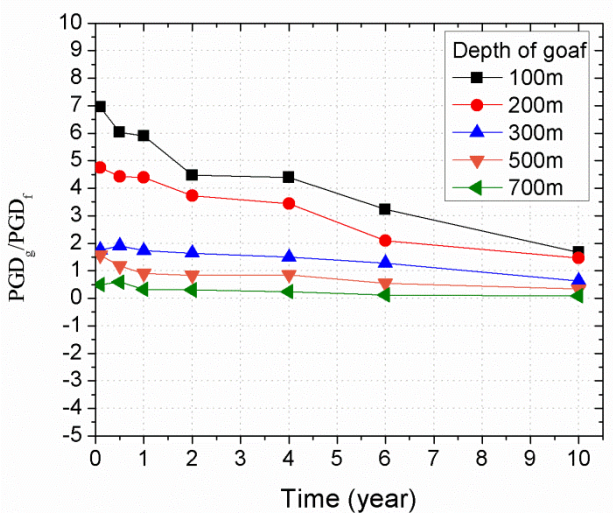

Figure 5-15. Effect of compaction time on PGD.

In order to study the reason of amplified displacement on the ground surface. We monitored the displacements including the surface and subsurface in the model for the cases of different depth and compaction time of goaf. The contour graph (Figure 5-16) shows that the displacement in the goaf is amplified around 5% compared to the undisturbed strata, which results in the release of energy in the goaf area and reduce the displacement above the goaf. However, the reduction of displacement above goaf is only 5% compared to that above the undisturbed strta. Whereas, as the increasing depth of goaf, the released effect on displacement in goaf can not affect the displacement on the ground surface above goaf (Figure 5-15-d). This shows a consistency to the displacement tendency on the ground surface (Figure 5-14). Consequently, the existence of goaf reduces around 5% of the displacement on the ground above goaf compared to that above the undisturbed strata.

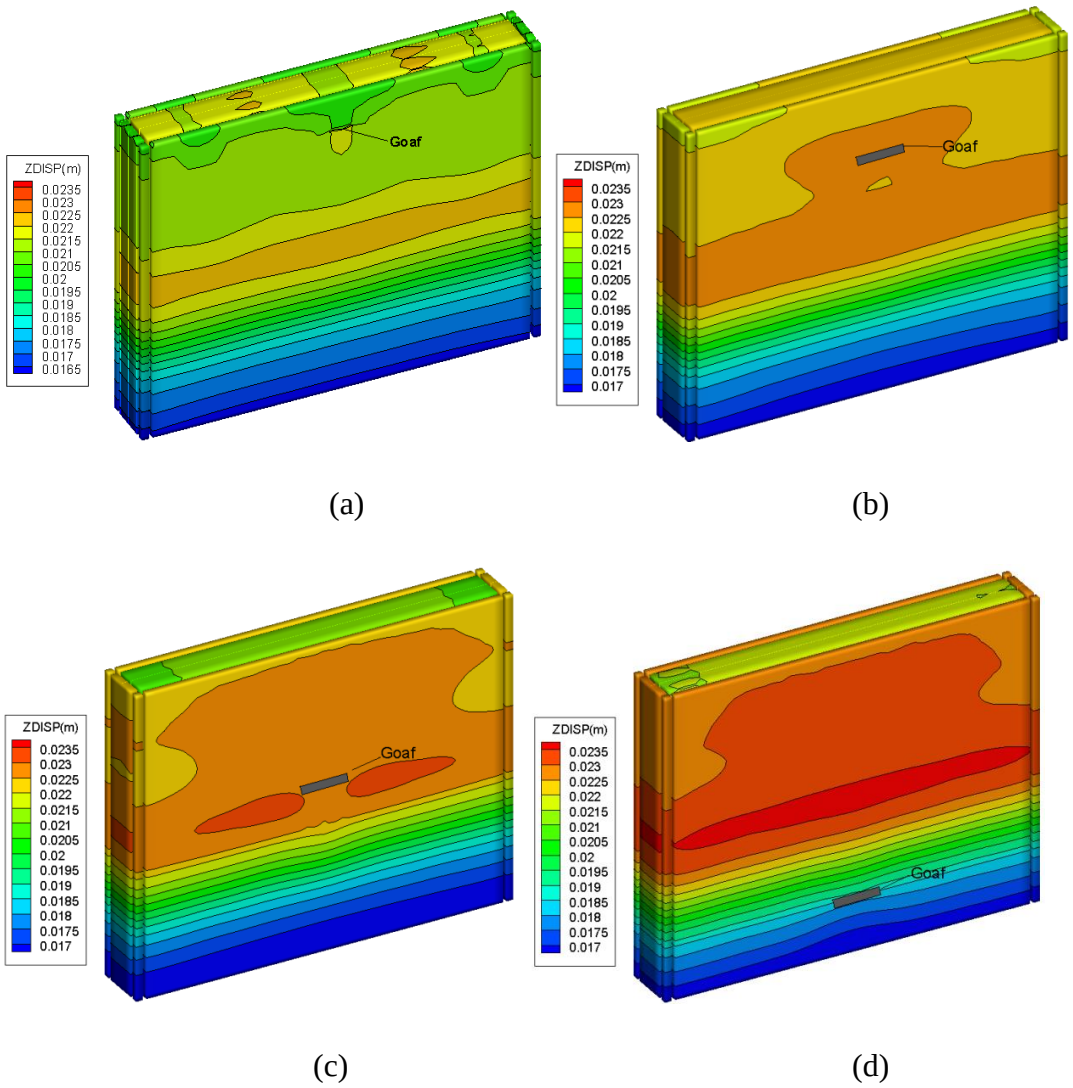

Figure 5-16. Displacements of subsurface and surface for the cases of different depths of goaf. (a) 100m, (b) 300m, (c) 500m and (d) 700m

Figure 5-17 shows the displacements at surface and subsurface for the cases of different compaction time of goaf at the depth of 300m. It can be observed that the displacement in goaf is decreased from 0.0225 to 0.0205 with the increasing compaction time from 0.1 year to 4 years. This indicates the release of displacement in the goaf area is gradually decreased as the increase of compaction time of goaf, which results in the less effect of goaf on the displacement on the ground surface above goaf.

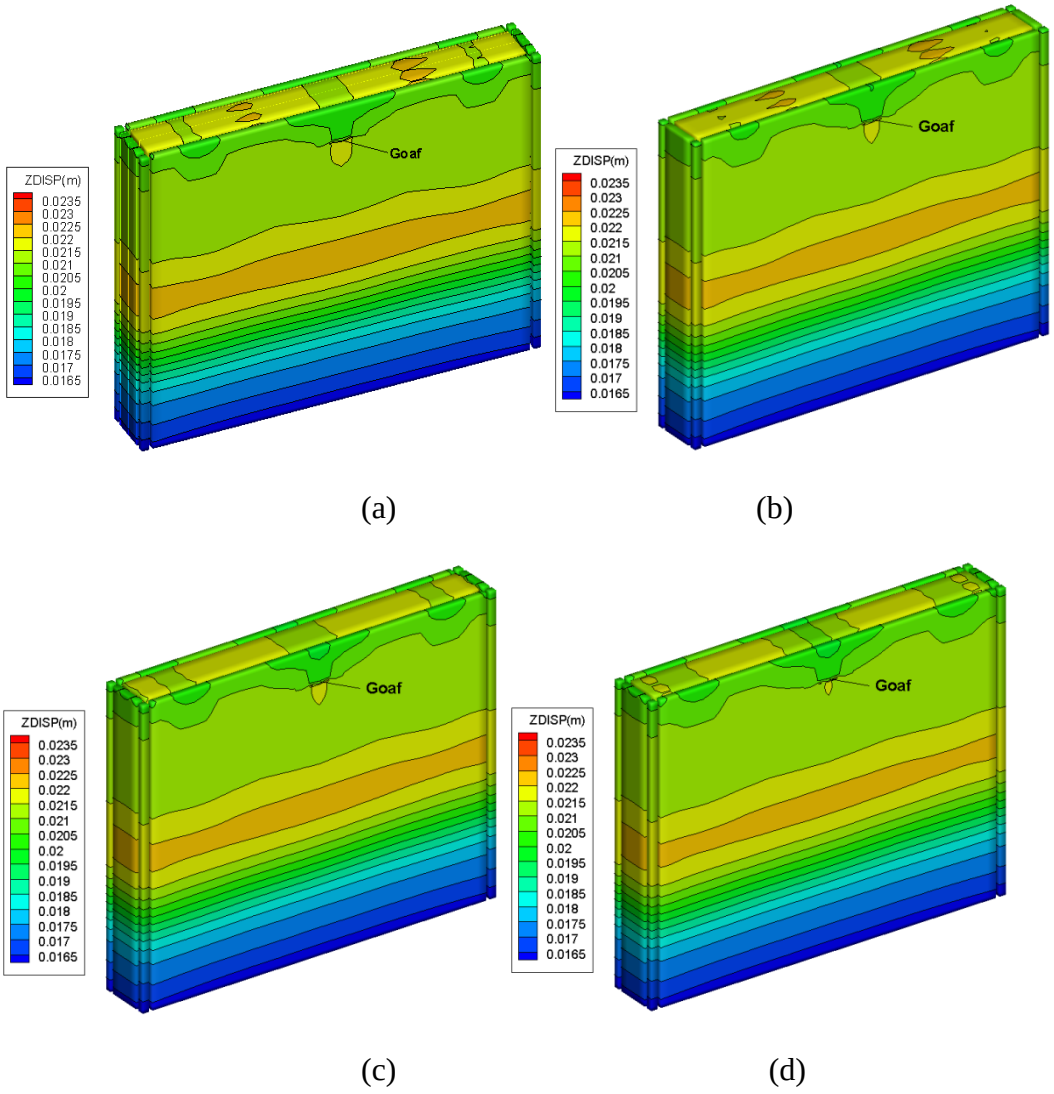

Figure 5-17. Displacement of surface and subsurface for the cases of goafs under different compaction time. (a) 0.1 year, (b) 1 year, (c) 2 years and (d) 4years

5.6.5 Response acceleration on the ground surface above goaf

A plot of the peak value of a response acceleration as a function of the natural vibration period of the system is called the response spectrum for this quantity (Bozorgnia and Bertero, 2004).

For a system of single degree of freedom (SODF),

$$\ddot{x}(t) + 2\xi\omega_0\dot{x}(t) + {\omega_0}^2 x(t) = -\ddot{x}_g(t); \quad \omega_0 = \sqrt{k/m}; \ \ \xi = \frac{c}{2m\omega_0}; \tag{5-14}$$

Using Duhamel's integral, the maximum of displacement can be express as (Agrawal and Shrikhande, 2006)

$$|x(t)|_{max} = \left| \int_0^t \ddot{x}_g(\tau) \frac{e^{-\xi\omega_0(t-\tau)}}{\omega_d} ins\omega_d(t-\tau)d\tau \right|_{max} \quad (5\text{-}15)$$

Then, the absolute acceleration response spectrum, S_a is expressed as

$$S_a(\xi, \omega_0) = |\ddot{x}_a(t)|_{max} = \left|\ddot{x}(t) + \ddot{x}_g(t)\right|_{max} \quad (5\text{-}16)$$

Therefore, the response acceleration is able to estimate the acceleration value incorporating the incident seismic and system itself at the specific period (or frequency).

The Figure 5-18 to Figure 5-20 depicted the absolute response accelerations of the points on the ground surface at the fixed damping ratio of 0.05.

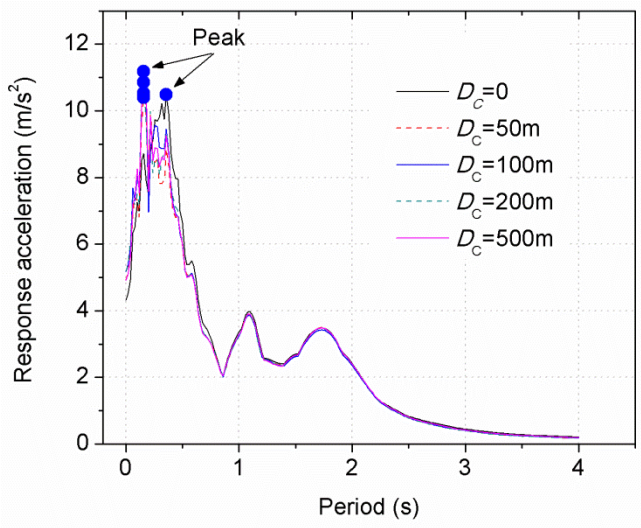

Figure 5-18. Response acceleration spectrum of points with different distances to the center of goaf on the ground surface.

Throughout the results of Figure 5-18, the response acceleration at the point closer to the goaf on the ground surface is smaller. The resonant period of the point above goaf is

0.2s larger than that of the point above the undisturbed strata. This indicates that the seismic response of the points above goaf on the ground surface is not amplified, instead, the seismic damage is smaller compared to the points above the undisturbed coal seam because of the larger resonant period.

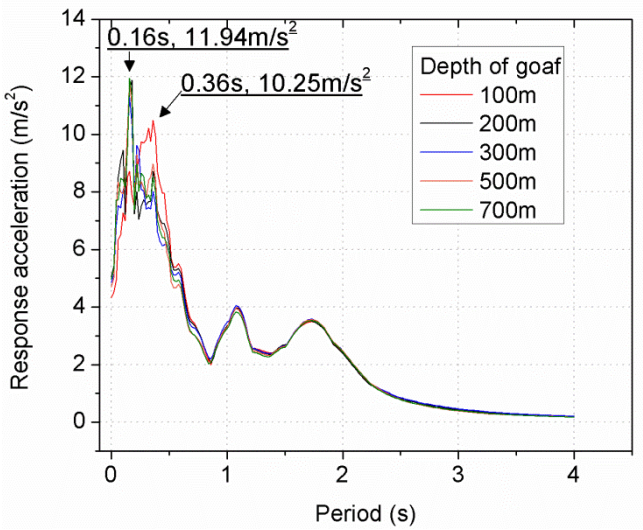

Figure 5-19. Response acceleration spectrum of point #1 above different depths of goaf.

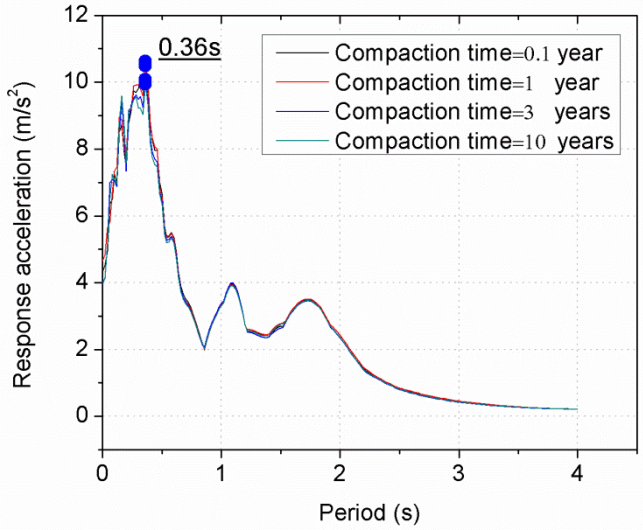

Figure 5-20. Response acceleration spectrum of point #1 above a 100m-depth-goaf for the cases of different compaction time.

It can be seen in Figure 5-19 that the response acceleration of point #1 increases with the increasing depth of goaf. Meanwhile, the resonant period at the maximal response

acceleration increases as the depth of goaf reduces. Which corresponds to the resonant frequency at the maximal response acceleration decreases for the shallow-depth of goaf. As is known that the danger is smaller as the resonant period is larger (Baker, 2008). Therefore, the presence of shallow-depth of goaf reduces the risk of the constructions on the underground above goaf. It can be found in Figure 5-20 that the resonant period is not strongly affected by the compaction time of goaf for the case of 100-depth-goaf. While, the response acceleration is lightly increased as the depth of goaf increases.

5.7 Conclusions

In this study, porous samples consists compressed rock and coal particles were measured by ultrasonic waves to evaluate the damping coefficient through a goaf area. The seismic response at the ground surface above the goaf areas were studied based on the estimated damping coefficient and reasonable elastic modulus of goaf area with numerical simulation analysis. Some main results are drawn as follows,

1. An empirical equation to estimate the damping coefficient through the goaf area has been presented for the simulations in terms of the porosity variation by laboratory measurement. Elastic modulus of the goaf area was evaluated by considering the compressive strength of the intact rock and porosity as well as the compaction time of the porous layers.

2. The simulation results on earthquake wave propagation showed that the peak acceleration above the goaf is smaller than that of the places above the undisturbed strata. Around 10 to 20% seismic energy was trapped in the goaf area, especially for the shallow and short-compaction-time goaf. The effect of goaf area on the surface acceleration is gradually decreased as the depth and compaction time of goaf increases.

3. The existence of goaf amplified the peak displacements on the ground surface compared to that of the free-field condition. The amplification is between 1 to 6 as

the depth changes from 100 to 700 m. Peak displacement above goaf is around 5% smaller than that above the undisturbed strata.

4. The resonance period on the ground surface above goaf is around 0.2s larger than that above the undisturbed strata.

Chapter 6: Final conclusions and outlook

6.1 Summary of present research

Seismic method is an effective tool to investigate the properties of goaf area including the porosity, size of fragments, pressure bearing, permeability and other valuable information. This research used compressed porous samples consists of 0.12-1 mm rock and coal particles, and ultrasonic wave with high frequency range from 37 to 250 kHz, covering the ratio of wavelength to fragments size of in-situ seismic investigation, to study the properties of goaf. A summaries of present research are as follow:

6.1.1 Laboratory measurements of seismic and permeability of simulated goaf cases

Rock and coal samples from USA (sandstone), Japan (limestone) and China (coal) were used in the experiment as the composition of the simulated goaf. Intact samples were crushed and sieved into smaller particles in the size of 0.12-1.0 mm to form the porous samples to simulate conditions of the actual goaf. The elastic modulus have been measured on these samples, the results showed a good agreement with the values in the actual goaf. Ultrasonic wave was used to measure the seismic velocity and attenuation of the samples. Different particle sizes, porosities and frequencies as well as the rock lithology were performed to find the effects of them on the seismic properties. It has been observed that the compressed samples with the porosity from 0.21 to 0.33 had a P-wave velocity from 600 to 1300 m/s, and the seismic attenuation is from 5 to 85 (1/m). The increasing particle size induce the increase of velocity but decrease of attenuation. The velocity dispersion and scattering attenuation are obvious for the ratio of wavelength over particle size was set to be smaller than 10. Permeability of the porous samples were also measured by steady-state method in the

laboratory. The permeability showed a range of 60 to 500 md varying with the increasing porosity.

6.1.2 Modeling of seismic attenuation through the simulated goaf

A new seismic attenuation model (the B-R model) based on the multi-fractured rock attenuation model has been established. The B-R model accounts for the greater attenuation through fragmented rock due to increased contact points between the particles, and decreased attenuation caused by network propagating through the porous media. The predicted seismic attenuation estimated by B-R model compared with the laboratory measurement results of ultrasonic wave attenuation using compressed porous rock and coal samples. A good consistency between them was found for various porosities, particle sizes and wavelength. The B-R model showed better agreement with measurement results when λ/D varied between 65 and 80, which covers most of the λ/D range expected at a coal mine goaf. 5. It is believed that B-R model is possible to estimate seismic attenuation through porous rock or a coal layer, such as a coal mine goaf. Besides, it is also capable of estimating the porosity or fragments size of the actual goaf based on the B-R model and the in-situ seismic investigations.

6.1.3 Relationship between permeability and seismic properties of goaf

The Kozney-Carman (*K-C*) equation with a percolation threshold porosity of 0.06 and variable porosity power of 4 showed a good consistency with the laboratory measurement. The variations of the seismic velocity (η) and attenuation (ξ) were employed to find the relationship between them to the parameters of permeability of the compressed porous samples. η showed a linear relationship with the square root of the tortuosity (τ) for τ = 5–10. ξ showed an approximately linear relationship with the porosity part of the *K-C* equation. An revised *K-C* equation is therefore proposed based on the seismic velocity, attenuation and particle size. The estimated

permeability based on the modified *K-C* equation showed a good agreement with the measured data. It is concluded that the permeability of the compressed porous samples could be predicted by seismic velocity and attenuation of the intact and porous samples.

6.1.4 Numerical simulation

The effect of goaf on the seismic response on the ground surface in the mining area was studied by numerical simulations. The damping coefficient of the goaf area in the simulation was given based on the B-R model we propose based on the laboratory experiment.

The presence of goaf has been observed to be like a buffer layer in the underground strata which absorbs the energy of seismic wave. The peak ground acceleration (PGA) above goaf is around 10-20% smaller compared with the PGA above undisturbed strata. The PGA above goaf is gradually increased with the increasing depth and compaction time of goaf. In the meantime, the peak ground displacement (PGD_g) with underlying goaf is 1-6 times amplified compared with that of free-field (PGD_f). The PGD above goaf is 5% smaller than that above the undisturbed strata. Furthermore, the existence of the underlying goaf could increase (decrease) the resonance period (frequency) of response acceleration on the ground surface. This indicates that the place above goaf exhibits less seismic response for the case of earthquake vibration.

6.2 Outlook

Since the fragments in goaf areas are from the collapsed roof blocks, the goaf is therefore filled with a mixture of different kinds of rock. The seismic properties and permeability of the mixture fragments are supposed to be conducted to study the effect of the rock proportion on the seismic and permeability.

Because of the risk of the in-situ investigation, the previous measurement inside the goaf area is quite limited. While, with the widely and densely goaf areas

distributed in the underground, the accurate in-situ measurement should be carried out by using advanced tools such as the robot or remote control method. If possible, the detailed condition of goaf can be grasped and enable the further study and evaluate the risk of goaf on the environment and mining field.

Finally, the pilot project of seismic monitor should be conducted in the mining area above goaf. Seismic acceleration on the ground surface in the mining area is therefore possible to be measured and propose an evaluation standard of the potential risk of the constructions on the ground surface above goaf area.

References

Adhikary, D., Guo, H., 2015. Modelling of longwall mining-induced strata permeability change. Rock Mechanics and Rock Engineering 48, 345-359, https://doi.org/10.1007/s00603-014-0551-7

Anon, 1978. Summary of damage in Tangshan earthquake. Earthquake Press, Beijing,

Athy, L.F., 1930. Density, porosity, and compaction of sedimentary rocks. AAPG Bulletin 14, 1-24, https://doi.org/10.1306/3d93289e-16b1-11d7-8645000102c1865d

Aydan, Ö., Genis, M., Sugiura, K., Sakamoto, A., 2012. Characteristics and amplifications of ground motions above abandoned mines, International Symposium on Earthquake Engineering, JAEE, 75-84

Aydan, Ö., Tano, H., Genis, M., 2007. Assessment of long-term stability of an abandoned room and pillar underground lignite mine. Turkish Journal of Rock Mechanics Bulletin, Turkish National Rock Mechanics Group, ISRM, 1-22,

Aydan Ö., Y.O., M. Daido, N. Tokashiki, 2003. Re-assessment of the seismic response and stability of stone masonry structures of Shuri Castle through shaking table tests, Fifth National Conference on Earthquake Engineering, Istanbul, Turkey, AE-041

Baker, J.W., 2008. An introduction to probabilistic seismic hazard analysis. Report for the US Nuclear Regulatory Commission, page Version 1,

Barton, N., 2007. Rock Quality, Seismic Velocity, Attenuation and Anisotropy, first ed. CRC, Boca Raton, https://doi.org/10.1121/1.1908239

Biot, M.A., 1956. Theory of propagation of elastic waves in a fluid‐saturated porous solid. I. Low‐frequency range. J. Acoust. Soc.Am. 28, 168-178, https://doi.org/10.1121/1.1908239

Boadu, F.K., Long, L.T., 1996. Effects of fractures on seismic‐wave velocity and attenuation. Geophys. J. Int. 127, 86-110, https://doi.org/10.1111/j.1365-246x.1996.tb01537.x

Bozorgnia, Y., Bertero, V.V., 2004. Earthquake engineering: from engineering seismology to performance-based engineering. CRC press,

Brunner, D., 1985. Ventilation models for longwall gob leakage simulation, Proceedings of 2nd US Mine Ventilation Symposium, September, 23-25

Cai, W., Dou, L., Cao, A., Gong, S., Li, Z., 2014. Application of seismic velocity tomography in underground coal mines: a case study of Yima mining area, Henan, China. Journal of Applied Geophysics 109, 140-149, https://doi.org/10.1016/j.jappgeo.2014.07.021

Cao, A., Dou, L., Cai, W., Gong, S., Liu, S., Jing, G., 2015. Case study of seismic hazard assessment in underground coal mining using passive tomography. Int. J. Rock Mech. Min. Sci. 78, 1-9, https://doi.org/10.1016/j.ijrmms.2015.05.001

Cerveny, V., 2005. Seismic ray theory. Cambridge university press, https://doi.org/10.1017/cbo9780511529399

Chen, T., Wang, X., Mukerji, T., 2015. In situ identification of high vertical stress areas in an underground coal mine panel using seismic refraction tomography. Int. J. Coal Geol. 149, 55-66, https://doi.org/10.1016/j.coal.2015.07.007

Cheng, Y., Wang, J., Xie, G., Wei, W., 2010. Three-dimensional analysis of coal barrier pillars in tailgate area adjacent to the fully mechanized top caving mining face. Int. J. Rock Mech. Min. Sci. 47, 1372-1383,

Clark, V.A., Tittmann, B.R., Spencer, T.W., 1980. Effect of volatiles on attenuation (Q−1) and velocity in sedimentary rocks. J. Geophys. Res. 85, 5190-5198,

Clover, P., 2008. Petrophysics MSc Course Note. Imperial College, London, 10-20,

Coussy, O., 1987. Acoustics of porous media. Editions Technip, https://doi.org/10.1121/1.402899

Crichlow, J.M., 1982. The effect of underground structure on seismic motions of the ground surface. Geophys. J. Int. 70, 563-575,

Cushman, J.H., Tartakovsky, D.M., 2016. The Handbook of Groundwater Engineering. CRC Press,

Dickinson, G., 1953. Geological aspects of abnormal reservoir pressures in Gulf Coast Louisiana. AAPG Bulletin 37, 410-432, https://doi.org/10.1306/5ceadc6b-16bb-11d7-8645000102c1865d

Dickinson, W.R., Suczek, C.A., 1979. Plate tectonics and sandstone compositions. Aapg Bulletin 63, 2164-2182, https://doi.org/10.1306/2f9188fb-16ce-11d7-8645000102c1865d

Dresen, L., Rüter, H., 1994. Seismic Coal Exploration: In-seam Seismics, first ed. Elsevier, New York, https://doi.org/10.1016/0148-9062(96)87542-5

Dvorkin, J., Mavko, G., Nur, A., 1995. Squirt flow in fully saturated rocks. Geophys. 60, 97-107, https://doi.org/10.1190/1.1822622

Dvorkin, J., Nur, A., 2002. Critical-porosity models. Memoirs-American Association of Petroleum Geologists, 33-42,

Ebrom, D.A., McDonald, J.A., 1994. Seismic Physical Modeling, first ed. Society of Exploration Geophysicists, Tulsa,

Eshelby, J.D., 1957. The determination of the elastic field of an ellipsoidal inclusion,

and related problems. Proc. R. Soc. Lond. A 241, 376-396,

Friedel, M., Scott, D., Williams, T., 1997. Temporal imaging of mine-induced stress change using seismic tomography. Engineering Geology 46, 131-141, https://doi.org/10.1016/s0013-7952(96)00107-x

Fujii, Y., Ishijima, Y., Ichihara, Y., Kiyama, T., Kumakura, S., Takada, M., Sugawara, T., Narita, T., Kodama, J.-i., Sawada, M., 2011. Mechanical properties of abandoned and closed roadways in the Kushiro Coal Mine, Japan. Int. J. Rock Mech. Min. Sci. 48, 585-596, https://doi.org/10.1016/j.ijrmms.2011.04.012

Fukuyama, M., Urata, K., Nishiyama, T., 2004. Geology and petrology of the Hirao Limestone and the Tagawa metamorphic rocks-with special reference to the contact metamorphism by Cretaceous granodiorite. Journal of Mineralogical and Petrological Sciences 99, 25-41,

Fumagalli, E., 1969. Tests on cohesionless materials for rockfill dams. Journal of Soil Mechanics & Foundations Div 92,

Ge, M., Wang, H., Hardy, H., Ramani, R., 2008. Void detection at an anthracite mine using an in-seam seismic method. Int. J. Coal Geol. 73, 201-212, https://doi.org/10.1016/j.coal.2007.05.004

Gibson, R.L., Ben‐Menahem, A., 1991. Elastic wave scattering by anisotropic obstacles: application to fractured volumes. J. Geophys. Res. 96, 19905-19924, https://doi.org/10.1029/91jb01668

Gochioco, L.M., 2000. High-resolution 3-D seismic survey over a coal mine reserve area in the US—A case study. Geophys. 65, 712-718, https://doi.org/10.1190/1.1444770

Group, I.C., 2012. FLAC3D 5.0 manual. Itasca Consulting Group Minneapolis

Guo, H., Yuan, L., Shen, B., Qu, Q., Xue, J., 2012. Mining-induced strata stress changes, fractures and gas flow dynamics in multi-seam longwall mining. Int. J. Rock Mech. Min. Sci. 54, 129-139,

Hanson, D.R., Vandergrift, T.L., DeMarco, M.J., Hanna, K., 2002. Advanced techniques in site characterization and mining hazard detection for the underground coal industry. Int. J. Coal Geol. 50, 275-301, https://doi.org/10.1016/s0166-5162(02)00121-0

Hardin, B.O., 1985. Crushing of soil particles. Journal of geotechnical engineering 111, 1177-1192,

Heid, J., McMahon, J., Nielsen, R., Yuster, S., 1950. Study of the permeability of rocks to homogeneous fluids, Drilling and production practice. American Petroleum Institute

Helgerud, M., Dvorkin, J., Nur, A., Sakai, A., Collett, T., 1999. Elastic‐wave velocity

in marine sediments with gas hydrates: Effective medium modeling. Geophysical Research Letters 26, 2021-2024,

Hsiung, S., Peng, S.S., 1985. Chain pillar design for US longwall panels. Min.Sci. & Technol. 2, 279-305,

Huang, J., Tian, C., Xing, L., Bian, Z., Miao, X., 2017. Green and Sustainable Mining: Underground Coal Mine Fully Mechanized Solid Dense Stowing-Mining Method. Sustainability 9, 1418,

Hudson, J.A., 1981. Wave speeds and attenuation of elastic waves in material containing cracks. Geophys. J. Int. 64, 133-150, https://doi.org/10.1111/j.1365-246x.1981.tb02662.x

Jiang, Y., Wang, H., Xue, S., Zhao, Y., Zhu, J., Pang, X., 2012. Assessment and mitigation of coal bump risk during extraction of an island longwall panel. Int. J. Coal Geol. 95, 20-33,

Johnson, K.L., 1987. Contact Mechanics, first ed. Cambridge university press, Cambridge, https://doi.org/10.1137/1029068

Jones, T., Nur, A., 1983. Velocity and attenuation in sandstone at elevated temperatures and pressures. Geophysical Research Letters 10, 140-143,

Kachanov, M., 1980. Continuum model of medium with cracks. Journal of the engineering mechanics division 106, 1039-1051,

Karacan, C., Esterhuizen, G., Schatzel, S., Diamond, W., 2007. Reservoir simulation-based modeling for characterizing longwall methane emissions and gob gas venthole production. Int. J. Coal Geol. 71, 225-245, https://doi.org/10.1016/j.coal.2006.08.003

Karacan, C.Ö., 2010. Prediction of porosity and permeability of caved zone in longwall gobs. Transport in porous media 82, 413-439, https://doi.org/10.1007/s11242-009-9437-7

Karacan, C.Ö., Ruiz, F.A., Cotè, M., Phipps, S., 2011. Coal mine methane: a review of capture and utilization practices with benefits to mining safety and to greenhouse gas reduction. Int. J. Coal Geol. 86, 121-156,

Kolsky, H., 1963. Stress waves in solids. Courier Corporation,

Kong, X., 1999. Advanced mechanics of fluids in porous media. University of Science and Technology of China Press, Hefei, China (in Chinese),

Kose, H., Cebi, Y., 1988. Investigation the stresses forming during production of thick coal seam, In: Proceedings of 6th Coal Congress of Turkey, Zonguldak, 371-383

Kukal, G., Simons, K., 1986. Log analysis techniques for quantifying the permeability

of submillidarcy sandstone reservoirs. SPE Formation Evaluation 1, 609-622, https://doi.org/10.2118/13880-pa

Lamur, A., Kendrick, J., Eggertsson, G., Wall, R., Ashworth, J., Lavallée, Y., 2017. The permeability of fractured rocks in pressurised volcanic and geothermal systems. Scientific Reports 7, 6173, https://doi.org/10.1038/s41598-017-05460-4

Li, W., Mu, Y., Zhang, J., Xu, Y., 2011. Optimization of surface detection technology and method of mine goaf. Coal Sci. Tech. 39, 102-106, https://doi.org/10.1109/icsdm.2011.5969112

Li, Z., Feng, G., Jiang, H., Hu, S., Cui, J., Song, C., Gao, Q., Qi, T., Guo, X., Li, C., 2018. The correlation between crushed coal porosity and permeability under various methane pressure gradients: a case study using Jincheng anthracite. Greenhouse Gases: Science and Technology, https://doi.org/10.1002/ghg.1757

Luan, H., Lin, H., Jiang, Y., Wang, Y., Liu, J., Wang, P., 2018. Risks Induced by Room Mining Goaf and Their Assessment: A Case Study in the Shenfu-Dongsheng Mining Area. Sustainability 10, 631,

Lubbe, R., Worthington, M., 2006. A field investigation of fracture compliance. Geophys. Prospect. 54, 319-331, https://doi.org/10.1111/j.1365-2478.2006.00530.x

Luijendijk, E., Gleeson, T., 2015. How well can we predict permeability in sedimentary basins? Deriving and evaluating porosity–permeability equations for noncemented sand and clay mixtures. Geofluids 15, 67-83, https://doi.org/10.1002/9781119166573.ch10

Lunarzewski, L., 2010. Coal mine goaf gas predictor (CMGGP).

Luxbacher, K., Westman, E., Swanson, P., Karfakis, M., 2008. Three-dimensional time-lapse velocity tomography of an underground longwall panel. Int. J. Rock Mech. Min. Sci. 45, 478-485, https://doi.org/10.1016/j.ijrmms.2007.07.015

Müller, T.M., Gurevich, B., Lebedev, M., 2010. Seismic wave attenuation and dispersion resulting from wave-induced flow in porous rocks—A review. Geophys. 75, A147-A164, https://doi.org/10.1190/1.3463417

Ma, D., Miao, X.-x., Wu, Y., Bai, H.-b., Wang, J.-g., Rezania, M., Huang, Y.-h., Qian, H.-w., 2016. Seepage properties of crushed coal particles. Journal of Petroleum Science and Engineering 146, 297-307, https://doi.org/10.1007/s11242-015-0473-1

Mavko, G., Nur, A., 1997. The effect of a percolation threshold in the Kozeny-Carman relation. Geophys. 62, 1480-1482, https://doi.org/10.1190/1.1444251

Murphy, W.F., 1982. Effects of microstructure and pore fluids on the acoustic properties of granular sedimentary materials. Ph. D. dissertation, Stanford University,

Nasseri-Moghaddam, A., Cascante, G., Phillips, C., Hutchinson, D., 2007. Effects of

underground cavities on Rayleigh waves—Field and numerical experiments. Soil Dyn. Earthquake Eng. 27, 300-313,

Nie, L., Zhang, M., Jian, H., 2013. Analysis of surface subsidence mechanism and regularity under the influence of seism and fault. Natural hazards 66, 773-780,

Oda, M., 1985. Permeability tensor for discontinuous rock masses. Geotechnique 35, 483-495,

Pappas, D.M., Mark, C., 1993. Behavior of simulated longwall gob material. US Department of the Interior. Bureau of Mines, 39

Peng, S., Loucks, B., 2016. Permeability measurements in mudrocks using gas-expansion methods on plug and crushed-rock samples. Marine and Petroleum Geology 73, 299-310, https://doi.org/10.1016/j.marpetgeo.2016.02.025

Peng, S.S., 2017. Advances in Coal Mine Ground Control. Woodhead Publishing,

Pepper, J.F., De Witt, W., Demarest, D.F., 1954. Geology of the Bedford Shale and Berea Sandstone in the Appalachian basin. Science 119, 512-513,

Poursartip, B., Fathi, A., Kallivokas, L.F., 2017. Seismic wave amplification by topographic features: A parametric study. Soil Dyn. Earthquake Eng. 92, 503-527, https://doi.org/10.1016/j.soildyn.2016.10.031

Prasad, M., 2003. Velocity-permeability relations within hydraulic units. Geophys. 68, 108-117,

Pride, S.R., 2005. Relationships between seismic and hydrological properties, Hydrogeophysics. Springer, 253-290,

Pyrak-Nolte, L., Morris, J., 2000. Single fractures under normal stress: The relation between fracture specific stiffness and fluid flow. Int. J. Rock Mech. Min. Sci. 37, 245-262,

Pyrak-Nolte, L.J., Myer, L., Cook, N., 1987. Seismic visibility of fractures.

Pyrak‐Nolte, L.J., Myer, L.R., Cook, N.G., 1990. Anisotropy in seismic velocities and amplitudes from multiple parallel fractures. J. Geophys. Res. 95, 11345-11358,

Quan, Y., Harris, J.M., 1997. Seismic attenuation tomography using the frequency shift method. Geophys. 62, 895-905, Seismic attenuation tomography using the frequency shift method

Raymer, L., Hunt, E., Gardner, J.S., 1980. An improved sonic transit time-to-porosity transform, In: Society of Petrophysicists and Well-Log Analysts, Houston, 1-13

Ren, T., Edwards, J., Jozefowicz, R., 1997. CFD modeling of methane flow around longwall coal faces, Proceedings of the 6th International Mine Ventilation Congress. Pittsburgh, 17-22

Sams, M., Neep, J., Worthington, M., King, M., 1997. The measurement of velocity dispersion and frequency-dependent intrinsic attenuation in sedimentary rocks. Geophys. 62, 1456-1464,

Sayers, C., Kachanov, M., 1991. A simple technique for finding effective elastic constants of cracked solids for arbitrary crack orientation statistics. International Journal of Solids and Structures 27, 671-680,

Schoenberg, M., Sayers, C.M., 1995. Seismic anisotropy of fractured rock. Geophys. 60, 204-211,

Schwartz, L.M., Kimminau, S., 1987. Analysis of electrical conduction in the grain consolidation model. Geophys. 52, 1402-1411, https://doi.org/10.1190/1.1442252

Shephard, L., Bryant, W.R., 1983. Geotechnical properties of lower trench inner-slope sediments. Tectonophysics 99, 279-312, https://doi.org/10.1016/0040-1951(83)90109-9

Shi, Y., Wang, C.Y., 1988. Generation of high pore pressures in accretionary prisms: Inferences from the Barbados subduction complex. J. Geophys. Res. 93, 8893-8910, https://doi.org/10.1029/jb093ib08p08893

Si, G., Durucan, S., Jamnikar, S., Lazar, J., Abraham, K., Korre, A., Shi, J.-Q., Zavšek, S., Mutke, G., Lurka, A., 2015. Seismic monitoring and analysis of excessive gas emissions in heterogeneous coal seams. Int. J. Coal Geol. 149, 41-54, https://doi.org/10.1016/j.coal.2015.06.016

Smart, B., Haley, S., 1987. Further development of the roof strata tilt concept for pack design and the estimation of stress development in a caved waste. Min.Sci. & Technol. 5, 121-130,

Smerzini, C., Aviles, J., Paolucci, R., Sánchez‐Sesma, F., 2009. Effect of underground cavities on surface earthquake ground motion under SH wave propagation. Earthquake Engineering & Structural Dynamics 38, 1441-1460,

Su, D., 1991. Finite element modeling of subsidence induced by underground coal mining: The influence of material nonlinearity and shearing along existing planes of weakness, In: 10th International Conference on Ground Control in Mining

Szlazak, J., Szlazak, N., Obracaj, D., Borowski, M., 2009. Method of Determination of Methane Concentration in Goaf, Proceedings of the Ninth International Mine ventilation Congress, India, 533-544

Tajduś, K., 2009. New method for determining the elastic parameters of rock mass layers in the region of underground mining influence. Int. J. Rock Mech. Min. Sci. 46, 1296-1305,

Tselentis, G.-A., Paraskevopoulos, P., 2002. Application of a high-resolution seismic

investigation in a Greek coal mine. Geophys. 67, 50-59, https://doi.org/10.1190/1.1451326

Vardoulakis, I., Beskos, D., Leung, K., Dasgupta, B., Sterling, R., 1987. Computation of vibration levels in underground space, International Journal of Rock Mechanics and Mining Sciences & Geomechanics Abstracts. Elsevier, 291-298

Wang, L., 2011. Foundations of stress waves. Elsevier,

Wang, L., Pan, D., Zhang, X., 2008. Three Techniques for Detecting Underground Mined-out Areas. Geo. Geoche. Explo. 32, 291-294, https://doi.org/10.1021/acs.energyfuels.7b00409

Wang, Y., Lu, J., Shi, Y., Yang, C., 2009. PS-wave Q estimation based on the P-wave Q values. Journal of geophysics and engineering 6, 386,

Wang, Y., Zhang, X., Sugai, Y., Sasaki, K., 2017. Determination of critical self-ignition temperature of low-rank coal using a 1 m wire-mesh basket and extrapolation to industrial coal piles. Energy Fuels 31, 6700-6710, https://doi.org/10.1021/acs.energyfuels.7b00409

Wardlaw, N., Li, Y., Forbes, D., 1987. Pore-throat size correlation from capillary pressure curves. Transport in porous media 2, 597-614, https://doi.org/10.1007/bf00192157

Wardle, L., Enever, J., 1983. Application of the displacement discontinuity method to the planning of coal mine layouts, 5th ISRM Congress. International Society for Rock Mechanics

Whittles, D., Lowndes, I., Kingman, S., Yates, C., Jobling, S., 2006. Influence of geotechnical factors on gas flow experienced in a UK longwall coal mine panel. Int. J. Rock Mech. Min. Sci. 43, 369-387, https://doi.org/10.1016/j.ijrmms.2005.07.006

Xie, H., 1993. Fractals in rock mechanics, first ed. Crc Press, Boca Raton,

Xie, H., 1996. Introduction to fractal rock mechanics. Beijing: Science Press

Xie, H., Chen, Z., Wang, J., 1999. Three-dimensional numerical analysis of deformation and failure during top coal caving. Int. J. Rock Mech. Min. Sci. 36, 651-658,

Xu, P., Mao, X., Zhang, M., Zhou, Y., Yu, B., 2014. Safety analysis of building foundations over old goaf under additional stress from building load and seismic actions. International Journal of Mining Science and Technology 24, 713-718,

Yavuz, H., 2004. An estimation method for cover pressure re-establishment distance and pressure distribution in the goaf of longwall coal mines. Int. J. Rock Mech. Min. Sci. 41, 193-205, https://doi.org/10.1016/s1365-1609(03)00082-0

Zhou, X.H., 2006. Characterization of combustion and explosion in the underground mine and study of control technology. Liaoning Technical University